INELASTIC MODEL FOR CYCLIC BIAXIAL LOADING OF REINFORCED CONCRETE

by

D. Darwin
D.A.W. Pecknold

A Report on a Research Project Sponsored by
THE NATIONAL SCIENCE FOUNDATION
Research Grant GI 29934

UNIVERSITY OF ILLINOIS
URBANA, ILLINOIS
July 1974

ACKNOWLEDGEMENTS

This report is based on a thesis submitted by David Darwin in partial fulfillment of the requirements for the Ph.D. degree. The support of Mr. Darwin's graduate study by a National Science Foundation Graduate Fellowship is gratefully acknowledged.

The numerical calculations were performed on the IBM 360/75 system of the Cumputing Services Office of the University of Illinois.

This study was funded in part under National Science Foundation Research Grant No. GI 29934.

TABLE OF CONTENTS

LIST OF TABLES

LIST OF FIGURES

Chapter 1

INTRODUCTION

1.1 General

Reinforced concrete is a major medium of construction throughout the world. While in service, reinforced concrete structures are subjected to many cycles of load. In the case of structures subjected to seismic loading, the cycles may be of large magnitude. The material within these structures is in a triaxial state of stress. In contrast, the procedures used in the design of reinforced concrete members are based primarily on short-term monotonic load tests, and the material properties used in design are obtained from uniaxial strength tests (4).

Experimental investigations (1,16,20,22,26,34,35), not yet incorporated into design procedures, have shown that the behavior of concrete and steel varies considerably from that demonstrated in simple strength tests when the materials are subjected to cycles of load, and in the case of plain concrete, to combinations of biaxial stress.

These findings, combined with the ever increasing complexity of reinforced concrete structures, make a strong case for continued research. The need for safe, economical structures can be satisfied to the fullest only when the behavior of the structures is adequately understood. One tool in research is the analytical model which provides a prediction of the behavior of reinforced concrete under varying load conditions. This report presents an inelastic model for the cyclic, biaxial loading of reinforced concrete.

1.2 Previous Work

In recent years the finite element technique has become a powerful analytical tool. Several different approaches have been taken to modeling reinforced concrete. A good review of this area is presented by Scordelis (33).

One approach, exemplified by the work of Jofriet and McNeice (15) and Bell (5) on reinforced concrete slabs, uses semi-empirical moment-rotation curves to define the behavior of the elements under load. A second general approach seeks to duplicate the behavior of reinforced concrete structures by modeling the behavior of the constituent materials.

Within the realm of this second approach, investigators have used different methods to model the material behavior of the concrete and the steel. Areas in which the individual models differ include distribution of the steel, bond between the steel and the concrete, stress-strain behavior of the steel, representation of cracks in the concrete, behavior after cracking, and behavior of the concrete in compression.

Ngo and Scordelis (27) first demonstrated the applicability of the finite element method to reinforced concrete beams. They modeled the steel and the concrete as linear elastic materials connected by linear elastic "bond" links. Cracking was modeled by the separation of nodal points and a redefinition of structural topology. Nilson (28) expanded this work by introducing nonlinear material behavior. The difficulty involved in providing for economical redefinition of structural topology has made this approach generally unpopular.

Rashid (29) introduced a different approach in which cracked concrete is treated as an orthotropic material. This approach has been used by many other investigators (8,9,10,11,13,21,31,37,40,42). Franklin (11) used this approach together with nonlinear material properties and discrete element representations for the steel, concrete and bond links, to model the behavior of frames and panels. Other investigators have found it useful to represent the steel as a distributed or "smeared", uniaxially-stressed material rather than as a number of discrete elements.

Many studies have dealt with beams, frames, walls and panels. Cervenka and Gerstle (8,9,10) modeled the steel as an elasto-plastic material. They idealized the concrete as an elasto-plastic material in compression and as an elastic brittle material in tension. Once a crack was opened, the newly defined orthotropic material could take stresses parallel to the crack only. Stiffness perpendicular to the crack and shear stiffness parallel to the crack were set to zero. A similar approach was presented by Valliappan and Doolan (40). Suidan and Schnobrich (37) and Yuzugullu and Schnobrich (42) used the same general approach for three-dimensional and two-dimensional representations, respectively, but found that they obtained better results after cracking if they kept a small value for shear stiffness parallel to the open cracks.

Scanlon (31) presented a layered element to model the behavior of reinforced concrete slabs under long-term load, including the effects of creep and shrinkage. He introduced the concept of "tension-stiffening" in which open cracks have a decreasing (rather than zero) tensile strength after cracking. The concrete and steel were modeled as linear materials. Lin (21) expanded this work by adding elasto-plastic material behavior. Both investigators

found that tension stiffening was very important in duplicating experimental behavior.

Mikkola and Schnobrich (25) presented an elasto-plastic material model for reinforced concrete shells. Hand, Pecknold, and Schnobrich (13) developed a layered element for plates and shells. Concrete behavior was modeled using a bilinear stress-strain curve up to "yielding". This change provided a noticeable improvement over the linear representation for the elastic range. They also allowed the concrete to retain a small shear stiffness after cracking. They found, as pointed out by Schnobrich et al (32), that this had much the same effect as the tension-stiffening of Scanlon (31) and Lin (21). The magnitude of the shear stiffness was not as important as the fact that some shear stiffness was retained.

The work discussed above obtained good results for monotonic loading. The single investigation that attempted to match behavior under cyclic loading (8,9,10) fell short. While the experimental specimens showed a continuing loss of stiffness and strength with each cycle of load, the analytical model showed little of this degrading behavior. This inability to model cyclic behavior appears to be due primarily to the way in which the material properties were modeled.

The work of Blakely and Park (6) and Aktan, Pecknold and Sozen (2,3) provide two examples of structural models in which reasonable matches for cyclic loading were obtained using uniaxial representations for the constituent materials. Blakely and Park modeled prestressed concrete beams with a series of horizontal elements. The steel and the concrete had nonlinear stress-strain curves. Concrete behavior included a downward portion of the stress-strain curve and hysteresis upon cycling. Aktan et al modeled the behavior of

reinforced concrete columns subjected to planar movement by using "finite filaments" of concrete and steel to represent the column cross section. The concrete followed a parabolic stress-strain curve up to maximum strength and thereafter behaved plastically if confined. Both studies differentiated between confined and unconfined concrete and both ignored the effects of shear. These models provide satisfactory results for a limited class of problems.

Several nonlinear material models have been presented in recent years. Liu, Nilson and Slate (23,24) and Kupfer and Gerstle (19) have proposed constitutive models for monotonic, biaxial loading of plain concrete. Sinha, Gerstle and Tulin (35) and Karsan and Jirsa (17) have proposed models for cyclic, uniaxial loading. Aktan, Karlsson, and Sozen (1) have devised two possible models for the cyclic behavior of reinforcing steel.

1.3 Object and Scope

It is the purpose of this investigation to develop an inelastic material model to be used in conjunction with the finite element technique to simulate the behavior of reinforced concrete structures under cyclic, biaxial loading. The model is designed to be used not only for planar structures, such as shear walls, shear panels, and beams, but for any reinforced concrete structure which may be considered to be in a state of plane stress. Examples of structures in this latter category are slabs, shells, and reactor containment vessels. The material model, a sequential step toward a three dimensional model for reinforced concrete, may be used for monotonic, cyclic, and dynamic (seismic) structural loads.

The investigation first considers the development of a consistent

material model that matches the existing experimental evidence for the behavior of plain concrete under monotonic, biaxial loading (19,20,22,23,24,26) and under cyclic, uniaxial loading (16,17,35). The reinforcing steel is idealized as a bilinear, uniaxially stressed material and compared with tests of reinforcing bars under cyclic loading (1,34).

The individual material models are combined with the finite element technique to demonstrate their use and applicability. Finite element calculations are compared with experimental results for a beam (7), two shear panels (8,10), and a shear wall-frame system (38) subjected to monotonic loading. Comparisons for a third shear panel (8,10) subjected to cyclic loading are also presented.

The resulting model should prove to be a highly useful research tool for use in the study of reinforced concrete structures.

Chapter 2

MATERIAL MODEL

2.1 General

Prior to developing a material model for reinforced concrete, it is appropriate to ask: Is there a need for a special model? Why not treat the concrete and the steel as linear, elastic materials as suggested in Fig. 2.1?

Reinforced concrete may be modeled as a combination of linear, elastic materials for limited load ranges and specific types of loading. Cervenka (8) and Yuzugullu and Schnobrich (42) modeled the concrete and reinforcing steel in shear walls, shear panels, and flexural members as elasto-plastic materials. For much of the load range that they investigated, the steel remained elastic and the concrete behaved as an elastic-brittle material. Both sets of investigations obtained reasonable results for monotonic loading. However, neither of these studies were able to match experimental data over the entire range of loading that they investigated.

It is not the goal of this investigation to synthesize a model for limited use, but rather to develop a material model for reinforced concrete to be used for general loading situations in which the material stresses may be approximated by a state of plane stress.

It is essential that a constitutive model exhibit the important characteristics of the actual material. It is known that concrete behaves in a highly nonlinear manner in uniaxial compression, but may be idealized as a linear, elastic, brittle material in uniaxial tension, as shown in

Fig. 2.2. Under biaxial states of stress, concrete exhibits not only different stress-strain behavior, but varying strength characteristics (19,20,23, 26). Figures 2.3 and 2.4 demonstrate the effect of biaxial stresses on the stress-strain behavior and on the strength of plain concrete. The experimental work that has been done on the behavior of concrete under cyclic loading (17,35), while limited to uniaxial compression, has yielded important information. As shown in Fig. 2.5, hysteresis curves are formed with each cycle of load. The area enclosed by each curve represents energy dissipated during each cycle. The studies in this area have also shown that the envelope curve, obtained from a controlled strain compression test, closely approximates the maximum values of stress that may be obtained with each cycle of load.

Reinforcing steel behaves as a linear elastic material until it reaches its yield strength. Thereafter the steel behaves plastically, then strain hardens, and finally fails as shown in the virgin stress-strain curve illustrated in Fig. 2.6. Under cycles of loading, investigators (1,34) have found that the steel behaves quite differently, as shown in Fig. 2.7. The steel not only exhibits strain-hardening with cycles of load, but exhibits the Bauschinger effect upon load reversal.

The material model developed during this investigation has the key characteristics described above. In many areas, however, no experimental evidence exists. For example, no work has been completed on the behavior of concrete under biaxial, cyclic loading. In these cases the characteristics of the material model were selected in order to provide simplicity and to provide consistency, both internally and with experimentally established behavior.

2.2 Concrete

2.2.1 Orthotropic Constitutive Equations

Since the material model is designed to be used in conjunction with the finite element technique, the constitutive equations must be written in a form applicable to that technique. The material is treated as an incrementally linear, elastic material. That is, during each load increment the material is assumed to behave elastically. Between increments, the material stiffness and stress are corrected to reflect the latest changes in deflection and strain, using an adaptation of the Initial Stress Method (43).

Plain concrete has been idealized as an isotropic material by Kupfer and Gerstle (19), and as an orthotropic material by Liu, Nilson, and Slate (24). The stress-strain curves for plain concrete, as shown in Fig. 2.8, strongly suggest stress-induced orthotropic material behavior, which is the constitutive model used in this investigation.

Neglecting shear deformation for the moment, the equations relating change in strain to change in stress, for an incrementally linear orthotropic material may be written as follows:

$$d\varepsilon_1 = \frac{d\sigma_1}{E_1} - \nu_2 \frac{d\sigma_2}{E_2}$$

$$d\varepsilon_2 = -\nu_1 \frac{d\sigma_1}{E_1} + \frac{d\sigma_2}{E_2} \qquad (2.1)$$

where E_1, E_2, ν_1, ν_2 are stress-dependent material properties, and the material axes, 1 and 2, coincide with the current principal stress axes.

Solving these equations for change in stress in terms of change in strain and rewriting the solution in matrix form gives:

$$\begin{bmatrix} d\sigma_1 \\ d\sigma_2 \end{bmatrix} = \frac{1}{1 - \nu_1\nu_2} \begin{bmatrix} E_1 & \nu_2 E_1 \\ \nu_1 E_2 & E_2 \end{bmatrix} \begin{bmatrix} d\varepsilon_1 \\ d\varepsilon_2 \end{bmatrix} \tag{2.2}$$

From energy considerations, it may be shown that

$$\nu_1 E_2 = \nu_2 E_1 \tag{2.3}$$

In order to utilize these equations, the values of E_1, E_2, ν_1, and ν_2 must be known for each increment of load. To simplify their use and to insure that neither direction is favored, these relations may be modified by letting

$$\nu^2 = \nu_1\nu_2 \tag{2.4}$$

where ν is an "equivalent" Poisson's ratio dependent on the state of stress and strain in the material. Using Eqs. 2.3 and 2.4, Eq. 2.2 may be rewritten in a symmetrical form.

$$\begin{bmatrix} d\sigma_1 \\ d\sigma_2 \end{bmatrix} = \frac{1}{1 - \nu^2} \begin{bmatrix} E_1 & \nu\sqrt{E_1E_2} \\ \nu\sqrt{E_1E_2} & E_2 \end{bmatrix} \begin{bmatrix} d\varepsilon_1 \\ d\varepsilon_2 \end{bmatrix} \tag{2.5}$$

Equation 2.5 may now be expanded to include the shear term as shown below.

$$\begin{bmatrix} d\sigma_1 \\ d\sigma_2 \\ d\tau_{12} \end{bmatrix} = \frac{1}{1 - \nu^2} \begin{bmatrix} E_1 & \nu\sqrt{E_1E_2} & 0 \\ & E_2 & 0 \\ \text{sym} & & (1 - \nu^2)G \end{bmatrix} \begin{bmatrix} d\varepsilon_1 \\ d\varepsilon_2 \\ d\gamma_{12} \end{bmatrix} \tag{2.6}$$

or more simply:

$$d\sigma = D\, d\varepsilon$$

It should be noted that no experimental work has been done as yet in order to determine the value of shear modulus of plain concrete under a general state of biaxial stress. In addition, as in the case of Poisson's ratio, it is desirable that no particular direction be favored with respect to the shear stiffness of the material model. A satisfactory resolution of this situation is obtained by observing the effect of an axis rotation of angle θ on the constitutive matrix, D, as shown in Fig. 2.9. The constitutive matrix, D', in the new coordinates, where $d\sigma' = D' d\varepsilon'$, is given by

$$D' = T^T D\, T \tag{2.7}$$

where T is the matrix that transforms strains between axes.

$$d\varepsilon = T\, d\varepsilon'$$

$$T = \begin{bmatrix} \cos^2\theta & \sin^2\theta & \sin\theta\cos\theta \\ \sin^2\theta & \cos^2\theta & -\sin\theta\cos\theta \\ -2\sin\theta\cos\theta & 2\sin\theta\cos\theta & \cos^2\theta - \sin^2\theta \end{bmatrix}$$

At an arbitrary angle θ, the value of the shear modulus becomes:

$$G' = \sin^2\theta\cos^2\theta\,(E_1 + E_2 - 2\nu\sqrt{E_1E_2}) + (\cos^2\theta - \sin^2\theta)^2 G \tag{2.8}$$

G' becomes independent of the value of θ if,

$$G = G' = \frac{1}{4}(E_1 + E_2 - 2\nu\sqrt{E_1E_2}) \quad (2.9)$$

Substituting Eq. 2.9 into Eq. 2.7 gives the constitutive equations at an angle θ with the material coordinates:

$$\begin{bmatrix} d\sigma_1' \\ d\sigma_2' \\ d\tau_{12}' \end{bmatrix} = \frac{1}{1-\nu^2} \begin{bmatrix} E_1\cos^2\theta+E_2\sin^2\theta & \nu\sqrt{E_1E_2} & \frac{1}{2}(E_1-E_2)\sin\theta\cos\theta \\ & E_1\sin^2\theta+E_2\cos^2\theta & \frac{1}{2}(E_1-E_2)\sin\theta\cos\theta \\ \text{sym} & & \frac{1}{4}(E_1+E_2-2\nu\sqrt{E_1E_2}) \end{bmatrix} \begin{bmatrix} d\varepsilon_1' \\ d\varepsilon_2' \\ d\gamma_{12}' \end{bmatrix} \quad (2.10)$$

or in the material coordinates:

$$\begin{bmatrix} d\sigma_1 \\ d\sigma_2 \\ d\tau_{12} \end{bmatrix} = \frac{1}{1-\nu^2} \begin{bmatrix} E_1 & \nu\sqrt{E_1E_2} & 0 \\ & E_2 & 0 \\ \text{sym} & & \frac{1}{4}(E_1+E_2-2\nu\sqrt{E_1E_2}) \end{bmatrix} \begin{bmatrix} d\varepsilon_1 \\ d\varepsilon_2 \\ d\gamma_{12} \end{bmatrix} \quad (2.11)$$

It should be pointed out that in addition to the shear modulus, the off-diagonal terms containing Poisson's ratio, ν, are also independent of orientation. It is also interesting to note that the constitutive matrix is defined by only three quantities, E_1, E_2, and ν.

As used in this investigation, the material coordinates are oriented on the principal stress axes for each material point investigated. For an individual load increment, the values of the material properties E_1, E_2, and ν are determined as a function of the state of stress and strain at each point through a procedure to be described below. The constitutive matrix is then rotated to the global axes where it is used to calculate the element stiffness. The orientation of the material axes and of the material properties are corrected with each iteration of the solution procedure.

2.2.2 Equivalent Uniaxial Strain

The concept of "equivalent uniaxial strain" was developed in order to keep track of the degradation of stiffness and strength of plain concrete and to allow actual biaxial stress-strain curves to be duplicated from "uniaxial" curves. Figure 2.10 is a typical stress-strain curve for concrete undergoing several cycles of load reversal in uniaxial compression. It may be seen that many values of strain correspond to a single value of stress. It can also be seen that subsequent stiffness and strength of the concrete is highly dependent upon the value of strain as well as the value of stress. For a material in uniaxial compression it is relatively simple to develop a model that takes into account the overall state of the material, as was done by Kent and Park (18) and Blakely and Park (6). In the uniaxial case, the strain quantity of importance is the total strain in the direction of load. For a biaxial state of stress, however, the strain in one direction is a function, not only of stress in that direction, but also of the stress in the orthogonal direction, due to the Poisson effect. This point is illustrated

in incremental form by Eq. 2.1. The concept of equivalent uniaxial strain provides a method to separate the Poisson effect from the cumulative strain.

Equivalent uniaxial strain is most easily introduced using a linear elastic material. Figure 2.11 shows two stress-strain curves for a linear material. One curve represents the plot of stress versus strain for uniaxial compression. The other curve represents stress versus strain in the major compressive direction for biaxial compression, where $\sigma_1 = \alpha\sigma_2$. This line is steeper than the first, due to the Poisson effect. At any value of stress, the true strain for biaxial compression is given by the biaxial loading line. The equivalent uniaxial strain for any stress is the strain corresponding to the stress on the uniaxial loading curve. For a linear elastic material, the equivalent uniaxial strain in the ith direction, ε_{iu}, is given by

$$\varepsilon_{iu} = \frac{\sigma_i}{E_i} \tag{2.12}$$

ε_{iu} may be thought of as the strain that would exist in the ith direction for zero stress in the jth direction.

The concept of equivalent uniaxial strain is easily extended to a nonlinear material, where

$$\varepsilon_{iu} = \int d\varepsilon_{iu} = \int \frac{d\sigma_i}{E_i} \tag{2.13a}$$

with $d\sigma_i$, $d\varepsilon_i$ = differential change is stress and equivalent uniaxial strain in the ith direction, respectively

and E_i = tangent modulus of elasticity in the ith direction

For an incremental analysis the equivalent uniaxial strain in the ith direction is:

$$\varepsilon_{iu} = \sum_{\substack{\text{all} \\ \text{load} \\ \text{increments}}} \frac{\Delta\sigma_i}{E_i} \tag{2.13b}$$

This concept proves to be extremely useful in modeling a material such as concrete. In this investigation, the equivalent uniaxial strains, ε_{1u} and ε_{2u} are associated with the principal stress axes. An example of how the equivalent uniaxial strain is calculated is illustrated in Fig. 2.12a. Mohr's circles are shown representing the state of stress at the beginning and the end of a load increment. In this example, since a shear stress was applied in addition to the normal stresses, the principal and material axes rotate by an angle θ. The change in equivalent uniaxial strain, $\Delta\varepsilon_{iu}$, is given by

$$\Delta\varepsilon_{iu} = \frac{\sigma_{i\ new} - \sigma_{i\ old}}{E_i} \tag{2.14}$$

where $\sigma_{i\ old}$ corresponds to the original i axis, $\sigma_{i\ new}$ corresponds to the new i axis and E_i represents the tangent modulus in the ith direction at the start of the load increment. The value for $\Delta\varepsilon_{iu}$ obtained in Eq. 2.14 is added to the previous value of ε_{iu} to give the new totals for equivalent uniaxial strain on the newly oriented material axes. It is important to note that if the material axes are not allowed to rotate, and are held to one orientation, this has the effect of ignoring the inelastic effects due to pure shear in those fixed axes. By allowing the material axes to rotate, the tangent stiffnesses, E_1 and E_2, always represent the moduli corresponding to the principal, and therefore extreme, values of stress.

It is possible, even through small load increments, for the material axes to rotate more than 90 degrees. This is undesirable since the stress and uniaxial strain history developed at one orientation should continue to control the behavior of the material in essentially the same orientation. For this reason, rotation of the material axes is limited to 90 degree regions that are centered on axes established by the first load increment on the structure. If the principal stress axes rotate more than 45 degrees from their originally established orientations, the material axes are reoriented to coincide with the principal stress axis within their respective regions. This is illustrated in Fig. 2.12b.

2.2.3 Monotonic Loading Curves - Description

The concept of equivalent uniaxial strain may now be used to define equivalent uniaxial stress-strain curves for plain concrete. The object is to define a family of stress-strain curves that may be used with the incrementally linear, orthotropic constitutive relations developed above to match the actual stress-strain behavior of plain concrete under biaxial, monotonic loading.

The curves selected for compressive loading are based on an equation suggested by Saenz (30) and illustrated in Fig. 2.13.

$$\sigma_i = \frac{\varepsilon_{iu} E_o}{1 + [\frac{E_o}{E_s} - 2] \frac{\varepsilon_{iu}}{\varepsilon_{ic}} + (\frac{\varepsilon_{iu}}{\varepsilon_{ic}})^2} \qquad (2.15)$$

where E_o is the tangent modulus of elasticity at zero stress, E_s is the secant modulus at the point of maximum compressive stress, σ_{ic}, and ε_{ic} is the

equivalent uniaxial strain at the maximum compressive stress. This curve is particularly useful because the initial slope, and the values of peak stress and corresponding strain may be entered as independent variables.

Determination of E_o

For this study the value E_o corresponds to the initial tangent modulus determined in a uniaxial compression test. If that data is not available, E_o may be estimated using the ACI formulation (4).

Determination of σ_{ic}

The value of maximum compressive stress, σ_{ic}, for different combinations of biaxial loading has been the object of at least three detailed experimental studies. Kupfer, Hilsdorf and Rusch (20), Liu, Nilson and Slate (23), and Nelissen (26) have conducted biaxial loading tests of concrete using brush-type loading heads. The maximum strength criteria that they obtained was quite consistent between the separate investigations and is illustrated in Fig. 2.4. It may be seen, for example, that for even a small amount of secondary compressive stress, the strength of concrete in compression is increased a relatively large amount. Kupfer and Gerstle (19) have suggested the analytical maximum strength envelope shown in Fig. 2.14a. This criteria has been adapted and is used with some minor modifications, shown in Fig. 2.14b, in this investigation.

For biaxial compression, Kupfer and Gerstle found that the strength envelope was closely approximated by the equation

$$\left(\frac{\sigma_1}{f_c'} + \frac{\sigma_2}{f_c'}\right)^2 - \frac{\sigma_2}{f_c'} - 3.65\,\frac{\sigma_1}{f_c'} = 0 \qquad (2.16)$$

where $\sigma_1 \geq \sigma_2$.*

If α, the ratio of σ_1 to σ_2, is used, then Eq. 2.16 may be rewritten to give the maximum compressive strength of the concrete, σ_{2c}, as a function of the uniaxial compressive strength, f_c' and α.

$$\sigma_{2c} = \frac{1 + 3.65\alpha}{(1 + \alpha)^2}\, f_c' \qquad (2.17)$$

The peak stress that may be obtained in the minor compressive direction is:

$$\sigma_{1c} = \alpha\sigma_{2c} \qquad (2.18a)$$

or

$$\sigma_{1c} = \alpha\,\frac{1 + 3.65\alpha}{(1 + \alpha)^2}\, f_c' \qquad (2.18b)$$

The values of σ_{1c} and σ_{2c} are used in this study to define the shape of the equivalent uniaxial stress-strain curves for a given value of α. The shapes of the curves change continuously as the ratio of σ_1 to σ_2 changes.

For tension-compression, Kupfer and Gerstle suggest a straight line reduction in tensile strength with increased compressive stress.

$$\sigma_{1t} = \left(1 - 0.8\,\frac{\sigma_2}{f_c'}\right) f_t' \qquad (2.19)$$

While this equation gave good results for material simulation, it was found that the simpler criteria of a constant tensile strength also worked quite

* This algebraic sign convention will be used throughout this report.

satisfactorily in the problems investigated in Chapter 4. Equation 2.17 is modified slightly for negative ratios of σ_1 to σ_2. For tension-compression, the compressive stress-strain curves are modeled with the following value for σ_{2c}:

$$\sigma_{2c} = \frac{1 + 3.28\alpha}{(1 + \alpha)^2} f_c' \qquad (2.20)$$

For tension-tension, Kupfer and Gerstle recommended a constant tensile strength, equal to uniaxial tensile strength of the material. This is in close agreement with the findings of other investigators (20,26). While the value suggested for uniaxial tensile strength as a function of compressive strength gives good results for the material tests, it seemed low for structural members, where the modulus of rupture seemed to give a better prediction of structural behavior than either the splitting tensile strength or the true tensile strength. This fact may be explained in part by the work of Sturman, Shah, and Winter (36). They found that plain concrete was able to undergo greater strains, and presumably greater stresses, when subjected to a strain gradient than was possible under uniaxial load.

Determination of ε_{ic}

The final step in defining the shape of the equivalent uniaxial curves requires a method to determine ε_{ic}, the equivalent uniaxial strain at which the peak compressive stress is attained. For values of strength greater than f_c' in absolute magnitude, a relatively large increase in ductility, or strain at maximum stress, has been noted in two investigations

(20,26). This increase in real strain over the uniaxial case occurred in spite of the Poisson effect.

To include this behavior in the model, a simple method is used. For biaxial compression, a constant value of Poisson's ratio, ν, of 0.2 is assumed. This corresponds to the value determined by Kupfer, Hilsdorf and Rusch (20). They found that Poisson's ratio remained essentially constant up to approximately 80 percent of the ultimate load, at which point it began to increase.

The experimental stress-strain curve for equal biaxial compression ($\alpha = 1$) is used to determine the effect of biaxial compression on increased ductility. The real strain at maximum compressive stress is converted to an equivalent uniaxial strain, ε_{ic}, by dividing by $(1 - \nu)$. This "removes" the Poisson effect from the strain. Since the value of ε_{ic} is known for the actual uniaxial curve, the values of ε_{ic} are established for two values of peak stress. If the values of ε_{ic} are assumed to vary linearly with peak compressive strength, the following relationship is determined.

$$\varepsilon_{ic} = \varepsilon_{cu} \left[\frac{\sigma_{ic}}{f'_c} \cdot R - (R - 1)\right] \tag{2.21}$$

where ε_{cu} = strain at peak stress for the real uniaxial curve, and

$$R = \frac{\dfrac{\varepsilon_{ic}\ (\alpha = 1)}{\varepsilon_{cu}} - 1}{\dfrac{\sigma_{ic}\ (\alpha = 1)}{f'_c} - 1} \tag{2.22}$$

The available data (20,22,23,26) indicate that values of R equal to approximately 3, give good results.

Equation 2.21 does not give good results for values of σ_{ic} that are of smaller absolute magnitude than f_c'. During the development of the equivalent uniaxial curves it was found that as the magnitude of σ_{ic} drops below f_c' (i.e., lower compressive strength) that the value of ε_{ic} changes very little at first. It drops significantly only with relatively large reductions in σ_{ic}. The variation of ε_{ic} with σ_{ic} for this range of peak compressive strength is expressed by the following equation:

$$\varepsilon_{ic} = \varepsilon_{cu} \left[-1.6 \left(\frac{\sigma_{ic}}{f_c'}\right)^3 + 2.25 \left(\frac{\sigma_{ic}}{f_c'}\right)^2 + 0.35 \left(\frac{\sigma_{ic}}{f_c'}\right)\right] \quad (2.23)$$

While not extremely attractive, this equation produced satisfactory results. The values of ε_{ic} are constrained to insure that the ratio E_o/E_s in Eq. 2.15 is always greater than or equal to 2. This prevents the shape of the stress-strain curve from becoming concave upward.

Representative curves from the family of equivalent uniaxial stress strain curves are shown in Fig. 2.15 for different values of σ_{ic}.

A value for the "effective" Poisson's ratio, ν, of 0.2 proved quite satisfactory for monotonic loading in tension-tension and compression-compression. This value also proved to be adequate for uniaxial compression and tension-compression at low values of stress. However, in the latter two cases for values of stress above about 80 percent of f_c', 0.2 proved to be too small. It is interesting to note that this is the level of stress at which Kupfer, Hilsdorf and Rusch found that the Poisson's ratio of concrete starts

to increase. The apparent variation of the effective Poisson's ratio may be approximated satisfactorily as follows:

$$\nu = 0.2 \qquad \text{for tension-tension and compression-compression} \tag{2.24a}$$

$$\nu = 0.2 + 0.6 \left(\frac{\sigma_2}{f_c'}\right)^4 + 0.4 \left(\frac{\sigma_1}{\sigma_{1t}}\right)^4$$

$$\nu \leq 0.99$$

$$\text{for uniaxial compression and tension-compression} \tag{2.24b}$$

It should be noted that in Eq. 2.24b the value of ν remains close to 0.2 until relatively high values of stress are attained. ν is limited to a maximum value of 0.99 for purposes of the numerical solution. It also should be pointed out that there is no philosophical difficulty involved with allowing Poisson's ratio to exceed a value of 0.5 (the value for an incompressible material). A greater value means that the volume of the material is increasing, which is in fact the case for plain concrete.

Concrete is modeled in tension as a linear, elastic brittle material.

2.2.4 Monotonic Loading Curves - Comparison

The equivalent uniaxial stress-strain curves described above are combined with the incremental, linear orthotropic constitutive equations described previously to simulate the behavior of plain concrete under monotonically increasing biaxial stress. The parameters that control the behavior

of the model are the maximum uniaxial compressive stress, f'_c, the strain at maximum uniaxial compressive stress, ε_{cu}, the uniaxial tensile strength, f'_t, and the initial tangent modulus E_o.

The formulation presented here is compared with the experimental data of Kupfer, Hilsdorf and Rusch (20) and Nelissen (26) and is also compared with the analytical models advocated by Liu, Nilson and Slate (23,24) and Kupfer and Gerstle (19).

The experimental investigations utilized brush-type loading heads to minimize lateral confinement of the specimens due to friction. Kupfer, Hilsdorf and Rusch, and Nelissen investigated biaxial tension, biaxial compression and tension compression. Representative examples of biaxial stress-strain curves are shown in Figs. 2.16 through 2.26. These curves are compared with the results of this investigation as well as the analytical models of Liu, Nilson and Slate, and Kupfer and Gerstle.

Liu, et al. modeled concrete as an orthotropic material under biaxial loading conditions. Their model is derived in terms of total stresses and strains, as a variation of Saenz's equation. Stress is given as a function of initial uniaxial stiffness, uniaxial strength, total strain at maximum stress, Poisson's ratio, total strain and the ratio between principal stresses. Their formulation is applicable to biaxial compression only, and does not take into account load reversal or rotation of principal stress axes. The nature of the model causes the stress to become indefinite (infinite slope) in the minor compressive direction for a ratio of σ_1 to σ_2 of 0.2 as seen in Fig. 2.18. As an integral portion of their model, Liu et al. established a constant value for total strain at maximum stress in the major

compressive direction of .0025, while allowing the total strain at maximum stress in the minor principal direction to vary. They also set the maximum compressive strength of concrete to a constant value, 1.2 f'_c, for values of α between 0.2 and 1.0. Poisson's ratio in the primary compressive direction is always 0.2. The value in the minor compressive direction varied in accordance with Eq. 2.3. Liu, et al (24) modified their equations for use in an incremental finite element procedure, but they do not illustrate its use.

Kupfer and Gerstle (19) have proposed an isotropic material model for concrete under biaxial loading. They presented a series of closed form expressions for the secant shear modulus and the secant bulk modulus. The expressions were derived by curve fitting the data obtained by testing three representative sets of concrete specimens under various combinations of monotonic biaxial stress. The behavior of the model is controlled by the octahedral shear stress. Kupfer and Gerstle adapted their closed form equations for use in both a secant constitutive matrix and a tangent constitutive matrix. Their model does not account for unloading, and while they obtain good results for most levels of biaxial compression, they obtain a poor match with experimental data at high values of stress, and by their own admission, do not obtain good results for uniaxial compression or tension-compression.

The models of Kupfer and Gerstle, and Liu, et al, and the proposed model are compared with the experimental stress-strain curves of Kupfer, Hilsdorf and Rusch (20) and Nelissen (26) for various combinations of biaxial compression in Figs. 2.16 through 2.23. These diagrams illustrate both the strong points and the weak points of the models. All three models match the monotonic loading curves in the major compressive direction with reasonable accuracy.

However, the models of Liu, et al, and Kupfer and Gerstle fall short in modeling the behavior in the minor compressive direction. At high stresses, Kupfer and Gerstle's model exhibits an unrealistic stiffening in the σ_1 direction, as shown in Figs. 2.16, 2.20, and 2.22. On the other hand, Figs. 2.20 and 2.22 show that Liu's model is unreasonably soft in the σ_1 direction at high stresses. Figure 2.18 illustrates the previously mentioned limitation in Liu's model that imposes a zero strain in the minor compressive direction for α equal to 0.2.

The proposed model gives good results in the cases illustrated, in both principal directions and shows none of the idiosyncrasies exhibited by the other two models. It is interesting to note that none of the models gives a close approximation of Nelissen's curves for $\alpha = 0.2$, as shown in Figs. 2.18 and 2.19. This is due to the fact that this experimental curve deviates considerably from the balance of Nelissen's results. These particular curves are included to illustrate, among other things, the type of variation in behavior that is typical of concrete. The work presented in this report does not attempt to model the statistical variation in the material properties.

In matching Nelissen's curves, a value of f_c' equal to 90 percent of the prism strength and a value of ε_{cu} equal to .0022 are used. These values represent the average percentage strength for all of Nelissen's uniaxial tests and the value for strain at maximum uniaxial compressive strength recommended by Liu (22), respectively. These average values proved to give far better results than the actual values for this particular strength concrete, because Nelissen's published uniaxial curve had a value of f_c' equal to only 79 percent of the prism strength.

The variables used to define all three models are listed in Table 2.1. A value of R (see Eq. 2.22) equal to 3.15 is used in all cases.

The models proposed by Liu, et al, and Kupfer and Gerstle compare favorably with the experimental data of Kupfer, Hilsdorf and Rusch for uniaxial compression, as shown in Fig. 2.24. Kupfer and Gerstle's curve for tension-compression is presented in Fig. 2.25. The proposed model is compared with the same curves, plus several others in Fig. 2.26. These diagrams illustrate that while Kupfer and Gerstle's model diverges from the experimental curve for tension-compression, the proposed model obtains closer agreement as α, the ratio of σ_1 to σ_2, becomes more negative.

2.2.5 Cyclic Loading Curves

The proposed model is not restricted to monotonic loading as are those of Kupfer and Gerstle, and Liu, et al, but may be extended to include the behavior of plain concrete under cyclic loading. The objectives of modeling cyclic behavior include approximating the stress-strain behavior under cycles of load, approximating the number of cycles to a maximum load that cause "failure" of the concrete, and matching the energy loss due to the hysteresis effect.

Since no experimental data are available on the behavior of plain concrete under biaxial cyclic loading, the model is based on the experimental work of Sinha, Gerstle and Tulin (35), and Karsan and Jirsa (17) in which they investigated the behavior of concrete under cycles of uniaxial, compressive load. The model is then extended to biaxial loading.

The overall stress-strain behavior of concrete under cyclic loading is illustrated by the two experimental curves (17) shown in Fig. 2.27. This behavior is approximated by the proposed model shown in Fig. 2.28. Straight

lines were selected to approximate the downward portion of the stress-strain curve and hysteresis loops. This provided for maximum simplicity and at the same time gave a reasonable approximation of experimental behavior.

The initial portion of the envelope curve of the model is a monotonic equivalent uniaxial loading curve. The downward portion drops linearly from the point of maximum stress (a function of α) until a maximum compressive strain is reached and the concrete crushes. The stress and strain at the lower end of the line are independent of α. A reasonable match with experimental data is obtained with a crushing strain of four times ε_{cu}, and a stress, just prior to crushing, of 20 percent f'_c. This straight line behavior is somewhat similar to that used by Blakely and Park (6). The proposed envelope curve is compared with experimental envelope curves (39) in Fig. 2.29.

Typical hysteresis curves from experimental data and for the proposed model are shown in Fig. 2.30. The shape of the model curve is based on the findings of Karsan and Jirsa. They discovered a close relationship between ε_{en}, strain on the envelope curve just prior to unloading, and the residual strain remaining after all load was released, ε_p, which they called the "plastic strain". They found that these values could be related by the following equation:

$$\frac{\varepsilon_p}{\varepsilon_{cu}} = 0.145 \left(\frac{\varepsilon_{en}}{\varepsilon_{cu}}\right)^2 + 0.13 \left(\frac{\varepsilon_{en}}{\varepsilon_{cu}}\right) \qquad (2.25)$$

Equation 2.25 is used in this investigation to determine the plastic strain, ε_p, as a function of ε_{en}, the "envelope strain".

Karsan and Jirsa also found that there were a band of points on the stress-strain plane, as shown in Fig. 2.31, which controlled the degradation

of the concrete under continued cycles of load. The band is bounded from below by the "stability limit" and above by the "common point limit". They found that if load was cycled below the stability limit, the stress-strain curve formed a closed hysteresis loop. If the load was cycled above the stability limit, additional permanent strain would accumulate if the peak stress was maintained between cycles. The common point limit represents the maximum stress at which a reloading curve may intersect the original unloading curve.

For this investigation, the band was reduced to a single curve representing both the common point limit and the stability limit. The method of locating the "locus of common points" with respect to the envelope curve is described below.

As shown in Fig. 2.30, the reloading curve is represented by a straight line from the "plastic strain" point $(0,\varepsilon_p)$, through the common point. The unloading curve is approximated by three straight lines: the first with slope E_0; the second parallel to the reloading line; and the third with zero slope. Load reversals initially follow the line with slope E_0 between the parallel unloading and reloading lines.

For the case in which a second unloading takes place after the concrete has been reloaded past the common point but has not yet reached the envelope curve, a new unloading curve is defined based on the projected point of unloading on the envelope curve, as shown in Fig. 2.32. Each new projected unloading or "envelope" point defines a new common point and a new plastic strain. Continued cycles above the common point eventually result in intersection with the envelope curve.

The location of the common points with respect to the envelope curve may be adjusted to control the number of cycles to failure. As the locus of common points is lowered, fewer cycles of load are required to intersect the envelope curve for a given maximum stress.

Karsan and Jirsa found that as the maximum stress for each cycle was increased above the stability limit, the number of cycles to failure decreased. They also found that as the minimum compressive stress for each cycle was adjusted closer to the maximum compressive stress, the number of cycles to failure increased. A summary of their experimental results appears in Table 2.2. Several possibilities for location of the common points were investigated for the proposed model. The results are also summarized in Table 2.2. A good match with Karsan and Jirsa's data for cycles of load with zero minimum stress is obtained by setting σ_{cp}, the stress at the common point, equal to 5/6 σ_{en} for values of ε_{en} up to the peak compressive stress. For the downward portion of the stress-strain curve, the drop from σ_{en} to σ_{cp} is 1/6 f'_c of 1/6 σ_{en} (in the case of biaxial loading), which ever is of greater absolute magnitude, but in no case greater in absolute magnitude than 1/3 σ_{en}. A typical locus of common points is shown in 2.33. In addition to the case in which the maximum compressive stress lies below the common points, if the model is cycled solely between the envelope curve and the common points, no additional strain is accumulated.

The energy dissipated for each cycle is controlled by the location of the turning point $(\sigma_{tp},\varepsilon_{tp})$ as shown in Fig. 2.30. The lower the turning point, the greater the energy dissipated per cycle. A reasonably simple scheme that gives a satisfactory energy match for all but low values of ε_{en} is shown

in Fig. 2.33. σ_{tp} is taken as 1/2 σ_{en} for the upward portion of the envelope curve and for the downward portion in cases where σ_{en} is greater than f_c'. For the balance of the downward portion, σ_{tp} is taken as 1/2 f_c' with the additional requirement that the drop from the common point to the turning point must be at least as large in magnitude as the drop from the envelope to the common point. Individual curves for the model are compared with several experimental curves scaled from Reference (17) in Figs. 2.34 through 2.37. The model curves are based on the strain at which the experimental curve began unloading. The model curves were constructed in the following manner: If the experimental curve began to unload from the envelope curve, then the model was unloaded from the model envelope curve at the same strain; if the experimental curve unloaded from a point inside the experimental envelope curve, the model was unloaded from the same value of stress and strain. A summary of the energy match data is presented in Table 2.3. It may be seen that the model dissipates less energy than the experimental specimen at cycles of low strain, but improves as the strain increases. It was felt that any additional improvement in the energy match would come only at the expense of considerably increasing the complexity of the model.

The reason for selecting parallel unloading and reloading lines is of some importance. The initial model included converging unloading and reloading lines. However, it was soon evident that if a constant load was placed in one direction while the load was cycled in compression in the other direction, the strain increased in the direction of the constant load, "creating" energy and resulting in a type of "jacking" effect. This jacking effect was due to the changing Poisson's ratio ($E_1\nu_2 = E_2\nu_1$) as one load was cycled

around the hysteresis loop. By making the unloading and reloading lines parallel, the resulting strain was zero at the completion of each cyle of load. This device did not take into account the lowest portion of the unload-reload curve shown in Fig. 2.38. In order to prevent the jacking effect from occurring in this area, Poisson's ratio is temporarily set to zero in the area bounded by the zero stress line, the reloading line, and the line defined by:

$$\sigma = -\sqrt{E_o E_B}\,(\varepsilon_{iu} + \frac{\sigma_{tp}}{E_B} - \varepsilon_{tp}) \qquad (2.26)$$

This insures that the accumulated strain in the noncycled direction is zero for all of the closed hysteresis loops illustrated.

Referring to Fig. 2.28 additional characteristics of the model may be noted. The model may take tensile stress up to the values defined by Fig. 2.14 along lines which are extensions of the reloading curves.

For low values of ε_{en} the unloading and reloading take place on a single line with slope E_o. This occurs when $|\varepsilon_{en}| \leq \frac{1}{4}|\varepsilon_{cu}|$ or when the line from $(\sigma_{en},\varepsilon_{en})$ to $(0,\varepsilon_p)$ is steeper than E_o. Figures 2.39 and 2.40 provide a comparison of the model with the experimental results of two load histories run by Karsan and Jirsa.

For simplicity, a constant value for the equivalent Poisson's ratio, ν, of 0.2 is used when cycling for values of $|\varepsilon_{en}| \leq |\varepsilon_{cu}|$. For $|\varepsilon_{en}| > |\varepsilon_{cu}|$, ν is set to zero and not changed thereafter. This is done because experimental investigations of concrete under biaxial loading (20,22,23,24,26) have noted that for biaxial compression, the final failure is manifested by splitting parallel to the plane in which the loads are applied. It is reasoned that at high strains, the effect of change in strain in one principal direction

upon strain in the other principal direction is greatly diminished. A Poisson's ratio of zero serves to model this reduced interaction.

2.2.6 Cracking

The phenomena of cracking is extremely important in the load-deflection behavior of reinforced concrete structures. It is therefore not surprising that the formation of cracks plays an important part in the behavior of analytical models of these same structures.

For the proposed model, cracking first occurs when the tensile strength of the concrete is exceeded, as discussed in Section 2.2.3. When the principal stress in the concrete exceeds the tensile strength, a "crack" forms perpendicular to the principal stress direction, as illustrated in Fig. 2.41a. Cracking is modeled by reducing the value of E to zero along the original principal stress direction. Rather than representing a single crack, this procedure has the effect of orienting many finely spaced cracks perpendicular to the principal stress direction as shown in Fig. 2.41b; for simplicity, this type of behavior will be referred to as single crack formation. When a single crack occurs, the constitutive equations take the following form in material coordinates:

$$\begin{bmatrix} d\sigma_1 \\ d\sigma_2 \\ d\tau_{12} \end{bmatrix} = \begin{bmatrix} 0 & 0 & 0 \\ 0 & E_2 & 0 \\ 0 & 0 & E_2/4 \end{bmatrix} \begin{bmatrix} d\varepsilon_1 \\ d\varepsilon_2 \\ d\gamma_{12} \end{bmatrix} \qquad (2.27)$$

where the 1 direction is perpendicular to the crack.

This equation is obtained from Eq. 2.11 with $E_1 = 0$. Although the crack is open, shear may be transferred along the crack representing the friction and interlock that occur in concrete. Not only does some shear transfer seem realistic (in this case elastic transfer), but other investigators (13, 41) have found that even a small amount of shear stiffness gave significantly better results than providing for no shear transfer.

In addition to the single crack discussed above, the model includes five other crack configurations. The six possible configurations, shown in Fig. 2.42, are identical to those used by Yuzugullu and Schnobrich (41). The possibilities are: no cracks; one crack; first crack closed; first crack closed and second crack open; both cracks closed; and both cracks open. A second crack may form while the first crack is either open or closed, and forms like the first, when the tensile strength of the concrete is exceeded. If the first crack is open, the second crack will form perpendicularly to the first. If the first crack is closed, then the orientation of the second crack depends on the orientation of the principal tensile stress. Independent of their orientation, if both cracks are open, the constitutive matrix takes the following form:

$$D_{concrete} = [0] \tag{2.28}$$

It is necessary, when modeling concrete under cyclic loading, to have a criterion that may be used to establish the point at which a crack closes. The concept of "crack width" is defined for this purpose. By the nature of the finite element procedure that is used in this study, and the method used to represent a crack, crack width is defined in terms of strain at a point rather than as the separation of two pieces of material.

Just after a crack is first formed, the crack width, C_{wi}, is defined by the following equation:

$$C_{wi} = \frac{\sigma_{cri}}{E_i} \tag{2.29}$$

where σ_{cri} is the stress that caused the crack and E_i is the tangent stiffness that was assumed prior to crack formation. Since the stress across a crack is zero, σ_{cri} must be reapplied to the structure as a residual stress. It is worthy to note that once the tensile strength of the concrete has been exceeded, the presence of steel has no effect on the crack width defined in Eq. 2.29. That is, the crack opens to its full width whether or not steel is present in the concrete. This behavior has the effect of momentarily reducing the bond strength between the steel and the concrete to zero and then restoring perfect bond between the two materials. This is the only portion of the model in which any type of bond slip is approximated.

Once a crack has formed, the change in equivalent uniaxial strain, $\Delta\varepsilon_{ju}$, parallel to the crack is given by:

$$\Delta\varepsilon_{ju} = \Delta\varepsilon_j \tag{2.30}$$

where $\Delta\varepsilon_j$ is the change in real strain parallel to the crack.

The change in the equivalent uniaxial strain perpendicular to the crack, $\Delta\varepsilon_{iu}$, and therefore the change in crack width, is given by:

$$\Delta\varepsilon_{iu} = \Delta\varepsilon_i + \nu\Delta\varepsilon_j \tag{2.31}$$

A constant value of $\nu = 0.2$ is used in Eq. 2.31.

At a given point in time, the crack width may be determined by combining Eqs. 2.29 and 2.31.

$$C_{wi} = \frac{\sigma_{cri}}{E_i} + \sum_{\substack{\text{Load increments} \\ \text{following crack} \\ \text{formation}}} (\Delta\varepsilon_i + \nu\Delta\varepsilon_j) \qquad (2.32)$$

When the crack width becomes less than or equal to zero, the crack is said to have closed. Equation 2.32 shows that compressive strain increments, parallel as well as perpendicular to the crack, tend to close the crack. Tensile strain increments increase the crack width.

When two cracks are open at the same time, the Poisson's effect is removed from Eq. 2.31, giving:

$$\Delta\varepsilon_{iu} = \Delta\varepsilon_i \qquad (i = 1, 2) \qquad (2.33)$$

where the incremental strains, $\Delta\varepsilon_i$, are taken perpendicular to each crack.

When a crack closes, the equivalent uniaxial strain at closing corresponds to the point at which the stress-strain curve crossed the zero stress line when the material first went into tension, as illustrated in Fig. 2.43.

While a crack is open, the material coordinates remain fixed. Once the crack closes, the material coordinates are again free to rotate; however, the material has no tensile strength perpendicular to the closed crack. Stresses across the closed cracks are checked at each iteration of the solution, and if a tensile stress is found, the crack is again opened, with a crack width, C_{wi}, as defined in Eqs. 2.29 through 2.33.

2.3 Steel

The virgin stress-strain curve for steel shown in Fig. 2.6 is a familiar sight to most engineers. The behavior of steel under cycles of load is less well known. For cyclic loading of reinforcing steel, Singh, Gerstle, and Tulin (34) showed that the elasto-plastic behavior was typical only for the virgin loading curve. Subjected to cycles of load, reinforcing steel exhibits substantial strain hardening, as well as a marked Baushinger effect. Aktan, Karlsson, and Sozen (1) studied the cyclic behavior of reinforcing steel subjected to large strain reversals. An example of their tests is shown in Fig. 2.7. They concluded that the stress-strain behavior was dependent on the previous loading history and the virgin properties of the steel, and that linear, elasto-plastic models gave conservative values for the energy adsorption characteristics of the steel. They investigated two analytical models for the steel: a Ramberg-Osgood representation, and a linear representation. The Ramberg-Osgood model gave a close match with the actual tests, but required, among other things, a prior knowledge of the extremes of stress to be encountered on each cycle. The linear representation gave satisfactory, though less accurate, results in most cases.

For this study, a simplified bi-linear model for the stress-strain behavior of steel is used. The model is such that the steel may be either elasto-plastic or strain hardening with a Baushinger effect. The model is compared with two tests by Aktan, et al (1) in Figs. 2.44 and 2.45. The strain hardening stiffness is usually taken in the range of 0.5 to 1.0 percent of initial elastic stiffness depending upon the material. A simple device to determine the strain hardening stiffness is to use the slope of the

line between the yield point and the point at which the ultimate strength is attained on the virgin stress-strain curve. If these data are not available, a value of 0.5 percent is used.

It may be seen from Figs. 2.44 and 2.45 that the model for steel gives generally conservative results for both strength and energy absorption.

As used in the composite material model, the steel is treated as a uniaxial material that is "smeared" throughout the concrete. This is similar to the approach used by Cervenka (8) and Yuzugullu and Schnobrich (42). The composite material constitutive matrix is obtained by adding the constitutive matrix for the steel to that of the concrete. In material coordinates, the constitutive matrix for the steel is given by:

$$D_{steel} = p_{steel} \begin{bmatrix} E_{steel} & 0 & 0 \\ 0 & 0 & 0 \\ 0 & 0 & 0 \end{bmatrix} \qquad (2.34)$$

where E_{steel} is the tangent stiffness of the steel and p_{steel} is the reinforcing ratio. D_{steel} is rotated to global coordinates using Eq. 2.7.

No attempt is made to model the bond between the steel and the concrete, except as noted in Section 2.2.6. The strain in the concrete and the strain in the steel are assumed to be the same at each material point.

Chapter 3

FINITE ELEMENT PROCEDURE

3.1 Isoparametric Element

The finite element used in this study was developed by Wilson, et al (41) and is shown in Fig. 3.1. The element is a four noded, quadrilateral isoparametric element with two degrees of freedom at each node, plus four extra degrees of freedom associated with nonconforming deformation modes. The degrees of freedom corresponding to the nonconforming modes illustrated in Fig. 3.1 may be thought of as internal degrees of freedom. Wilson, et al found that while the eight degree of freedom element gave satisfactory results for states of uniform tension and shear, it was too stiff in pure flexure. By adding the incompatible modes, they were able to obtain good agreement with the elastic solutions for various types of flexural loading with only a small number of elements.

The element stiffness matrix is calculated using the standard Gaussian numerical integration technique. The nonlinear material behavior of the composite material is followed at several points within each element allowing the variation in the state of the material across the element to be taken into account each time the element stiffness matrix is recalculated. Numerical integration is quite time consuming which becomes a major consideration if many load steps or iterations are required in the solution of a problem.

Figure 3.2 shows the location of the Gaussian integration points for a three by three grid of points. It is evident that while material property variation is accounted for in the elements, the integration points are

not located at the edges of the elements. The strains calculated at the integration points are, therefore, not the extreme values within the element. This may delay the nonlinear material response of the element.

Element properties are presented in greater detail in Appendix B.

3.2 Analysis Procedure

3.2.1 General

The basic input for the analysis procedure consists of a description of the topology and material properties of the structure. The loads are expressed as imposed displacements or nodal forces.

The material properties for the concrete are specified for each element. The percentage, orientation and material properties of the reinforcing steel are specified for the integration points within each element and may be varied from point to point. A detailed description of the input used in the analysis is presented at the end of Appendix A.

In this investigation, the number of Gaussian integration points within each element varied from nine to fifteen, with a three by three grid usually being sufficient.

The first step in the analysis consists of forming the structure stiffness matrix from the individual element stiffness matrices. The first stiffness matrix is based on the virgin material properties of the concrete and the steel.

The structure is then analyzed under several increments of load which may be either nodal loads or imposed nodal displacements. For each load increment, the solution is carried through several iterations until

specific convergence criteria are met (see Section 3.3). The structure is assumed to behave linearly within an iteration. Following each iteration the structure stiffness matrix is reconstructed using the tangent stiffness properties of the material and forces within the structure are corrected to reflect the nonlinear behavior of the material model. The force correction procedure is an adaptation of the Initial Stress Method of Zienkiewicz (43) and is illustrated schematically in Fig. 3.3. In the case of the imposed nodal displacements, the computer program which was developed has the capability of varying the boundary conditions during the load sequence. That is, the nodal points, at which a displacement (or zero displacement) is imposed, can be changed with each new load step. This provides extra flexibility for matching varied experimental loading schemes.

Following the solution of the nodal equilibrium equations, the nodal displacements are used to obtain the strains within each element, as described in Appendix B. The material strains at each integration point are used to determine the apparent changes in stress for the concrete and the steel. The apparent changes in stress for the materials are corrected to reflect their nonlinear behavior. The difference between the apparent stresses and the corrected stresses are the residual stresses which are used to calculate residual nodal loads. With each iteration, the state of each material point is updated, stresses are corrected, and a new tangent stress-strain matrix is calculated. The element and structure stiffness matrices are reconstructed and the residual loads are applied until the solution for that load step converges.

As the solution proceeds, the following information is available:

the load-deflection data, material stresses, cracking patterns, and other evidence of material nonlinearity such as strain-hardening in the steel and crushing in the concrete. The results of typical problems of this type are presented in Chapter 4.

3.2.2 Iterative Solution of Equilibrium Equations

The iterative procedure outlined above is described in more detail in this section. Assume that at some stage during the loading history, element stresses, σ, and nodal loads, P, satisfying the convergence criteria have been found. A new load increment, ΔP, is applied and the nodal equilibrium equations become

$$\sum_k L_k^T \int_{V_k} B^T (\sigma_k + \Delta\sigma_k)\, dV = P + \Delta P \qquad (3.1)$$

where the subscript "k" identifies the element and L_k is the localizing matrix relating u_k, the nodal displacement vector of element k, to U, the structure displacement vector. For convenience, the element labels and summations are omitted below.

The incremental equilibrium equation is

$$\int_V B^T \Delta\sigma dV = \Delta P + R \qquad (3.2)$$

where

$$R \equiv P - \int_V B^T \sigma dV$$

and represents the lack of satisfaction of equilibrium when iterations were terminated for the previous load increment. Since the actual stress changes

reflect nonlinear material behavior, the equilibrium equation is rewritten

$$\int_V B^T \delta\sigma dV = \Delta P + R + \int_V B^T (\delta\sigma - \Delta\sigma)\, dV \qquad (3.3)$$

where $\delta\sigma$ is a stress change found by using incorrect or approximate material properties. To emphasize the fact that nodal displacements as well as nodal loads may be imposed, the load vector is partitioned and Eq. 3.3 is rewritten as

$$\int_V B^T \delta\sigma dV = \begin{bmatrix} \Delta P_I \\ \hline \Delta P_B \end{bmatrix} + \begin{bmatrix} R_I \\ \hline R_B \end{bmatrix} + \int_V B^T (\delta\sigma - \Delta\sigma)\, dV \qquad (3.4)$$

where the subscript "I" denotes nodes at which loads are specified ("interior" nodes) and the subscript "B" denotes nodes at which displacements are specified ("boundary" nodes). It should be noted that ΔP_B is not known a priori.

The iteration procedure is carried out by setting

$$\begin{aligned} \Delta\sigma &= \Delta\sigma^{(1)} + \Delta\sigma^{(2)} + \ldots + \Delta\sigma^{(n)} \\ \delta\sigma &= \delta\sigma^{(1)} + \delta\sigma^{(2)} + \ldots + \delta\sigma^{(n)} \end{aligned} \qquad (3.5)$$

in Eq. 3.4, and then solving the sequence of linear problems,

$$\int_V B^T \delta\sigma^{(1)} dV = \begin{bmatrix} \Delta P_I + R_I \\ \hline \delta P_B^{(0)} \end{bmatrix}$$

$$\int_V B^T \delta\sigma^{(2)} dV = \begin{bmatrix} \delta R_I^{(1)} \\ \hline \delta P_B^{(1)} \end{bmatrix} \qquad (3.6)$$

$$\vdots \qquad\qquad \vdots$$

$$\int_V B^T \delta\sigma^{(i)} dV = \begin{bmatrix} \delta R_I^{(i-1)} \\ \hline \delta P_B^{(i-1)} \end{bmatrix}$$

where

$$\delta R^{(i-1)} \equiv \begin{bmatrix} \delta R_I^{(i-1)} \\ \hline \delta R_B^{(i-1)} \end{bmatrix} \equiv \sum_k L_k^T \int_{V_k} B^T (\delta\sigma_k^{(i-1)} - \Delta\sigma_k^{(i-1)}) dV$$

are residual loads, and $\delta P_B^{(i-1)}$ are boundary nodal forces necessary for equilibrium. Note that any convenient choice of material properties (as long as numerical stability is insured) may be made for determining $\delta\sigma^{(i)}$ and that once the state of strain corresponding to $\delta\sigma^{(i)}$ is known the actual stress change, $\Delta\sigma^{(i)}$, may be found, making possible the calculation of the residual load for the next iteration. The actual stress change, $\Delta\sigma^{(i)}$, is determined from the uniaxial stress-strain curves presented in Chapter 2. In this study, the current tangential stiffness, $D^{(i-1)}$ (see Chapter 2), is used in the determination of $\delta\sigma^{(i)}$. Thus

$$\delta\sigma^{(i)} = D^{(i-1)} B \delta u^{(i)} \qquad (3.7)$$

where $\delta u^{(i)}$ is the change in element nodal displacements for the current iteration. The sequence of linear problems (Eq. 3.6) becomes

$$\begin{aligned} K^{(0)}\delta U^{(1)} &= \delta P^{(0)} \\ &\vdots \quad\quad \vdots \\ K^{(i-1)}\delta U^{(i)} &= \delta P^{(i-1)} \end{aligned} \tag{3.8}$$

where $K^{(i-1)}$ is the structure tangent stiffness matrix assembled from the element tangent constitutive matrices, $D^{(i-1)}$. Since boundary conditions have not yet been imposed $K^{(i-1)}$ is singular. When iterations are terminated the residual load, $\delta R^{(n)}$, becomes R in Eq. 3.2 for the next load increment.

3.2.3 Solution of Equilibrium Equations

A typical iteration involves the solution of a set of linear equations, Eqs. 3.8, which may be rewritten in partitioned form as

$$\left[\begin{array}{c|c} K_{II}^{(i-1)} & K_{IB}^{(i-1)} \\ \hline K_{BI}^{(i-1)} & K_{BB}^{(i-1)} \end{array}\right] \left[\begin{array}{c} \delta U_I^{(i)} \\ \hline \delta U_B^{(i)} \end{array}\right] = \left[\begin{array}{c} \delta P_I^{(i-1)} \\ \hline \delta P_B^{(i-1)} \end{array}\right] \tag{3.9}$$

In Eq. 3.9 $\delta P_I^{(i-1)}$ is known, being either the specified nodal load increment (plus residual from the last increment) on the first iteration or a residual load on subsequent iterations; $\delta U_B^{(i)}$ is known, being either the specified boundary displacement on the first iteration, or zero on subsequent iterations. The conjugate quantities, $\delta U_I^{(i)}$ and $\delta P_B^{(i-1)}$, are unknown.

Equations 3.9 are altered to incorporate the known quantities

$$\begin{bmatrix} K_{II}^{(i-1)} & 0 \\ 0 & I \end{bmatrix} \begin{bmatrix} \delta U_I^{(i)} \\ \delta U_B^{(i)} \end{bmatrix} = \begin{bmatrix} \delta \bar{P}_I^{(i-1)} - K_{IB}^{(i-1)} \delta \bar{U}_B^{(i)} \\ \delta \bar{U}_B^{(i)} \end{bmatrix} \tag{3.10}$$

where the overbars indicate prescribed values. The matrix on the left hand side of Eq. 3.10 is now nonsingular, and the solution proceeds in the normal way. In Eq. 3.10,

$$\delta \bar{P}_I^{(0)} = \Delta P_I + R_I$$

$$\delta \bar{U}_B^{(1)} = \Delta \bar{U}_B \qquad \text{for the first iteration, } i = 1$$

and

$$\delta \bar{P}_I^{(i-1)} = \delta R_I^{(i-1)}$$

$$\delta \bar{U}_B^{(i)} = 0 \qquad \text{for subsequent iterations, } i > 1 \tag{3.11}$$

In the equation solver, rearrangement of the equation is not carried out as the matrix bandwidth would be increased. Rows and columns of the singular stiffness matrix corresponding to prescribed displacements are set to zero with the exception of the diagonal entry which is set equal to one, as suggested by Eq. 3.10. Appropriate changes are then made to the load vector (see Eq. 3.10). The above procedure has the advantage of preserving the symmetry and narrow bandwidth of the stiffness matrix.

The boundary nodal loads, $\delta P_B^{(i-1)}$, are computed at each iteration from Eq. 3.9, corrected with the boundary residual loads $\delta R_B^{(i-1)}$, and summed to compute ΔP_B, the nodal load increment at the boundary nodes.

$$\Delta P_B = \sum_{i=1}^{n} [\delta P_B^{(i-1)} - \delta R_B^{(i)}] - R_B + \delta R_B^{(n)} \qquad (3.12)$$

3.2.4 Updating D Matrix

As mentioned above (Section 3.2.2), it is possible to use D matrices other than the current tangent constitutive matrix for the computation of $\delta\sigma^{(i)}$ (Eq. 3.6). However, questions of efficiency and accuracy arise. Updating the D matrix (and K matrix) continuously is admittedly expensive; yet, this procedure should require the fewest iterations. In general, consideration should be given to the frequency with which the D matrix is updated versus the number of additional iterations required.

Other factors may play a role in determining how often the material properties must be updated. In a strongly path dependent problem, it is undesirable to get too far away from the actual history. In addition, there are certain cases in which the solution will not converge if the material stiffness is not updated. For example, if loading is taking place on a flat slope and the material subsequently unloads at a much steeper slope, it is possible for the solution to diverge.

Since the material properties modeled in this study are highly path dependent and the model does include large changes in stiffness as loads are cycled, the D matrix is updated with each iteration.

3.3 Convergence Criteria

Two criteria are used to establish convergence for an increment of load: one based on displacement and the other upon the magnitude of the residual loads.

The displacement criteria are the same for both nodal loads and imposed nodal displacements. In each case, the square root of the sum of the squares (root sum squares or RSS) of the change in nodal displacements for the last iteration, $\delta U^{(i)}$, is compared to the RSS of the total nodal displacements, U, and to the RSS of the change in the displacements occurring since the last load increment, ΔU. If the RSS for the latest changes is smaller than one-hundredth of the RSS of the total displacements or one-twentieth of the RSS of the total change in displacements, the solution is considered to have converged. These criteria are expressed symbolically as follows:

$$\frac{\text{RSS}\ (\delta U^{(n)})}{\text{RSS}\ (U)} \leq \frac{1}{100} \qquad \text{or} \qquad \frac{\text{RSS}\ (\delta U^{(n)})}{\text{RSS}\ (\Delta U)} \leq \frac{1}{20} \tag{3.13}$$

where $\text{RSS}\ (a) = (\sum_i a_i^2)^{1/2}$

Other values for the displacement criteria were investigated. Tighter requirements (one-thousandth and one-thousandth) required a significantly larger number of iterations with little apparent improvement in results. Looser requirements (one-fiftieth and one-tenth) resulted in a noticeable change in results and were therefore not used.

Once the displacement criteria are met, the solution is then checked for force convergence. The residual load at each node is checked. When nodal loads are applied to the structure, the residual load at each node is compared to one-fiftieth of the largest RSS of incrementally applied nodal loads encountered up to that point in the solution. When nodal displacements are applied, the residual loads are compared with either one-fiftieth of the

largest total calculated load at a node at which a displacement is imposed or seventy percent of the previous load criteria used. The force criteria are summarized below:

Nodal Loads:

$$\frac{|R_i|}{\max[RSS(\Delta P)]} \leq \frac{1}{50} \qquad i = 1, \text{ structure degrees of freedom} \qquad (3.14)$$

where R_i = residual load for structure degree of freedom i

ΔP = nodal loads applied in a single increment

Imposed Nodal Displacements:

$$\frac{|R_i|}{P'} \leq \frac{1}{50} \qquad i = 1, \text{ structure degrees of freedom} \qquad (3.15)$$

where P' = maximum of either $|P_{max}|$ or $0.7P''$

$|P_{max}|$ = maximum absolute total nodal load

P'' = P' for previous load increment

The results obtained using these criteria have been generally good. For the examples presented in Chapter 4, it was found that the deflection criteria were satisfactory for about thirty percent of the load increments, while the load criteria governed for the other seventy percent. When the load criteria were not used, the structure appeared to be stiffer. This fact was especially noticeable once cracking had begun. Generally, the loading sequences required force convergence, while for unloading sequences, displacement

convergence occurred quickly and also satisfied the force criteria. This is highly reasonable since the material being modeled exhibits more nonlinearity upon loading than upon unloading.

3.4 Special Techniques

Two techniques were used in order to deal with problems inherent in modeling some of the inelastic behavior of concrete.

The first technique deals with the downward sloping portion of the stress-strain curve. As shown in Fig. 2.28, the tangent modulus of elasticity for this portion of the monotonic loading curve is negative. However, using a negative value of E in the constitutive matrix may lead to erroneous results, such as a decrease in compressive strain with an increase in compressive load. In order to alleviate this problem, the tangent modulus on the downward portion of the stress-strain curve is set to zero for the purpose of the numerical solution, as shown in Fig. 3.5, and the stress is corrected to the proper value at the end of each iteration.

The second technique concerns the closing of tensile cracks. Once a crack is open, the incremental stiffness perpendicular to the crack is zero. For a structure, this results in a significant decrease in stiffness for movement in the direction that caused the crack to open. No difficulty arises while the crack remains open; the problem occurs as the crack begins to close, as in the case of cyclic loading. Just prior to closing, the elements containing the cracks appear to be soft. When the crack is closed, the low stiffness used for that increment may give a result which indicates that the concrete has undergone a large compressive strain perpendicular to the crack.

This result, which sometimes includes crushing of the concrete, is erroneous, since the actual stiffness is not used in the solution. To prevent displacement from being concentrated in the vicinity of an open crack just prior to its closing, an artificial stiffness is assigned perpendicular to the crack when the crack width, C_w, as defined in Chapter 2, is less than $|\varepsilon_{cu}|$. Within this range, the stiffness used is:

$$E = \frac{E_o}{2} \times \left(\frac{C_w + \varepsilon_{cu}}{\varepsilon_{cu}}\right)^2 \tag{3.16}$$

Note: $\varepsilon_{cu} < 0$

$C_w \geq 0$

It may be seen that when C_w equals $|\varepsilon_{cu}|$, E equals zero. E increases quadratically to a maximum value of one-half E_o for zero crack width. If the crack has not closed by the end of an iteration step, the accumulated stress is reduced to zero, with an equal residual stress being passed on to the structure. When a crack first opens, a stiffness of zero is used for the next iteration step. Thereafter, the varying value of E in Eq. 3.16 allows the residual stress generated to become smaller and smaller with each increment as the crack opens. As it closes, although the residual stresses in the vicinity of the crack may continue to increase, the steadily increasing value of E prevents an unreasonable concentration of displacement at the crack. This technique provides a method of approximating gradual crack closing even though the loads are applied in finite increments.

If two open cracks exist at a material point, a slightly different technique is used. Initially a value for the artificial stiffness is calculated

for each crack as described above. Since the cracks need not be perpendicular the values of E are averaged to obtain a representative stiffness. The material at the point is then treated as isotropic with $\nu = 0$. The residual stresses developed for the double crack are handled in the same manner as they are for the single crack and the technique has the same desirable results.

Chapter 4

NUMERICAL EXAMPLES

4.1 General

In order to demonstrate the usefulness and applicability of the proposed constitutive model, several numerical examples are presented in which the model is compared with experimental test results as well as analytical models proposed by other investigators (8,9,10,37,42). The examples include both monotonic and cyclic loading.

For monotonic loading, the model is compared with a singly reinforced concrete beam tested by Burns and Siess (7), two shear panels tested by Cervenka and Gerstle (8,9,10), and a shear wall-frame system tested by Umemura, Aoyama, and Liao (38).

The usefulness of the model for structures under cycles of load is demonstrated with a shear panel (8,9,10) subjected to large load reversals.

Data covering the material properties of the example test structures are presented in Table 4.1. The values presented by the original investigators were generally used. Estimates were made in cases where specific items of data were not available.

4.2 Monotonic Loading

The examples presented in this section consider the behavior of two types of reinforced concrete member and one reinforced concrete system under monotonically increasing load or deflection. They are presented in order of increasing complexity. One example also compares the analytical

behavior of the same structure with several loading schemes, including both nodal loads and imposed nodal displacements.

4.2.1 Singly Reinforced Beam--Burns and Siess

The ability of the proposed model to simulate the behavior of a simple type of structure is demonstrated with the singly reinforced beam shown in Fig. 4.1. Beam J-4 (7) was simply-supported at center depth and loaded with a concentrated load at center span.

The analytical model, shown in Fig. 4.2, takes advantage of symmetry and considers one half of the beam. For the model, the right hand support is two inches below the center-line to accomodate the finite element representation. Fourteen elements are used, each with a 3 by 4 grid of integration points. The single row of tensile steel is modeled by placing longitudinal steel in the lower half of the bottom row of elements; the stirrups are modeled as a uniform distribution of the steel through all elements.

The model is loaded with a series of imposed nodal displacements at mid-span. The results of the analysis are compared with the experimental load-deflection curve in Fig. 4.3. Figure 4.3 also contains the analytical results of Suidan and Schnobrich (37) in which they treated the concrete and the steel as elasto-plastic materials and utilized a grid of 18, three-dimensional, isoparametric elements.

The proposed model compares favorably with the experimental load deflection curve, and is somewhat better than the other model shown. The jagged portion of the curve on the "yield" plateau of the structure is due, in part, to the method of loading (imposed displacements) and in part, to the

fact that at several points on the plateau the solution did not meet the force convergence requirements presented in Chapter 3. That is, the next displacement was imposed at the conclusion of the maximum number of iterations for a load step without the previous solution having converged. One such point is the peak at a deflection of 1.2 inches.

As the model was loaded, the tension steel began to strain harden at a deflection of 1.2 inches and the concrete began to crush at a displacement of 1.3 inches. This last value compares to a deflection of 0.92 inches for the test. This discrepency may be due to the fact that integration points are not located on the extreme fibers of the beam.

Figure 4.4 shows the crack pattern of the analytical model and the location of those integration points at which the stress in the concrete and the steel are high. In addition to the concrete that has crushed, the concrete at two other material points is on the downward portion of the stress-strain curve, demonstrating the "softer" nature of the model as compared to an elasto-plastic representation.

The overall behavior of the model in this simple case is encouraging and does much to establish its applicability to more complex problems.

4.2.2 Shear Panels--Cervenka and Gerstle

The next examples deal with two reinforced concrete shear panels tested by Cervenka and Gerstle (8,9,10). The shear panels, shown in Fig. 4.5, were cast and loaded in groups of two to simplify the testing procedure. The panels were either two or three inches thick and were bounded by thickened ribs on two opposite sides. Panel reinforcement was varied from test to test.

Shear Panel--Lightly Reinforced

The first shear panel to be considered is specimen W-1, shown in Fig. 4.6a. W-1 was two inches thick and uniformly reinforced with 9 gage wire. The analytical model consisting of 24 elements, each with a 3 by 3 grid of integration points, is presented in Fig. 4.6b. In the load deflection curve (Fig. 4.7), the analytical model is compared to the average deflection of the two panels that made up the test specimen. The deflections of the two panels did not agree very closely. Also presented are the results of the analysis made by Cervenka and Gerstle in which they used elasto-plastic constitutive relations for the concrete and the steel and a finite element grid made up of 240 constant strain triangles, compared to a total of 216 integration points for the proposed model. The mode of failure of the test specimen, as well as that of both analytical models, consisted of the formation of nearly vertical cracks in the shear panel adjacent to the center rib.

Shear Panel--Varying Reinforcement

A more interesting test specimen, shear panel W-2 (Fig. 4.8a) was thicker and more heavily reinforced than was W-1. The reinforcement was also varied, so that a larger percentage of longitudinal steel was placed in the bottom six inches of the panel than was placed in the top twenty-four inches. The finite element grid was varied slightly to accomodate this non-uniform reinforcement. As indicated in Fig. 4.8b, this test was used not only to judge the accuracy of the constitutive model, but also to compare the results obtained using several loading schemes for the finite element model.

Figure 4.9 presents the results of the different analyses. The analytical solution obtained by Cervenka and Gerstle is not shown, but they obtained an extremely close match with the experimental curve. The experimental load deflection curve is compared to three analytical solutions: Solution A, in which the load was applied at two points on the outer rib to simulate the actual test; Solution B, in which a displacement was imposed at the outside corner of the rib; and Solution C, in which a concentrated load was applied at the outside corner of the rib. While differing, all three analytical solutions give a reasonable match with the test data including the structure "yield" load (all three are within ten percent).

The Solutions B and C, in which the load was concentrated at the outer edge of the rib give, as expected, lower "yield" strengths than Solution A, which modeled a load placed at the center of the outer rib. There is, however, some question as to why the difference exists between Solutions B and C (imposed displacement versus concentrated load at the same point). A possible explanation is that the load was effectively applied in increments of different size for Solutions B and C, which resulted in slightly different material behavior and cracking patterns. A more important reason has to do with the loading methods themselves.

A simple example, illustrated in Fig. 4.10, will point out this expected difference. Suppose that line OA represents the load-deflection curve for an uncracked structure, and line OBC represents the load-deflection curve for the same structure after it has cracked. If load increments are used, the analytical load deflection curve follows lines OA and AC making the structure appear to be elasto-plastic. The load deflection curve looks quite

uneven, however, if displacement increments are used, in which case, the true load deflection curve, OA, AB, BC, is obtained. While this example is over-simplified when compared to the highly path dependent problems presented in this report, it is gratifying to note that load deflection curves for solutions A and B remain quite close, up to the structure "yield" load. The two yield loads predicted are only eight percent apart.

The ability of the proposed model to duplicate experimental crack patterns is demonstrated in Figs. 4.11 and 4.12. Figure 4.11 compares the crack patterns for Solution A with those for the test at two load levels, 14 kips and 24 kips. The comparison is reasonable for 14 kips and quite good for 24 kips. The analytical model also indicates that portion of the concrete in which the compressive stress exceeds 0.8 f_c' in magnitude.

Figure 4.12 compares the crack patterns for Solutions A, B, and C with that of the test for a point on the structure "yield" plateau. The analytical solutions agree quite well with the experimental crack pattern, with Solution A showing somewhat more cracking than is evident in the experimental pattern or in Solutions B or C. Although the predicted loads differ considerably for Solutions B and C at this point, the crack patterns are very close. All three analytical solutions indicate the presence of cracks in the center rib. Whether or not these cracks were present in specimen W-2 cannot be ascertained from the available references (8,10). The experimental crack pattern also indicates that local crushing or splitting off of concrete in the compressive zone of the specimen has occurred. This type of behavior is also indicated by the analytical solutions, as shown, with Solutions A and B including portions of concrete that are on the downward portion of the stress-strain curve.

It may be concluded that all three analytical solutions gave a reasonable duplication of the experimental behavior of this test specimen.

4.2.3 Shear Wall-Frame System--Umemura, Aoyama, and Liao

The shear wall-frame system tested by Umemura, Aoyama and Liao (38) is shown in Fig. 4.13. Test specimen A-1 consisted of two structural systems cast together and tested like a simply-supported beam. The analytical model for a single shear wall-frame system consists of 20 elements with 12 integration points each, and is shown in Fig. 4.14. In the actual test, specimen A-1 was loaded to approximately 100 metric tons, unloaded and then reloaded to failure. The unloading cycle was not considered in the analytical solution. The load deflection curves for the test and the analytical model are shown in Figs. 4.15 through 4.17. Figures 4.15 and 4.16 compare the vertical displacement of the proposed model with that of the frame. Figure 4.16 also contains the results of an analysis by Yuzugullu and Schnobrich (42) in which they utilized elasto-plastic constitutive relations for the concrete and the steel and a finite element grid of 64 quadrilateral elements, each consisting of four constant strain triangles, plus special link elements to connect the shear wall to the frame. The proposed model predicted a lower "yield" strength than was actually obtained, but gave a reasonable match with the overall force deflection behavior. Yuzugullu and Schnobrich obtained a good match for the "yield" strength, but thereafter their model proved to be too stiff. Figure 4.17 compares the horizontal displacements of the lower outside corners of the model and specimen A-1. Again a good match is obtained with the overall behavior.

The experimental crack pattern for the maximum load of 197 tons is shown in Fig. 4.18 and may be compared with the analytical crack patterns for 100 tons and 200 tons in Fig. 4.19. The large diagonal cracks occurred in specimen A-1 at a load of 127 tons. The cracking pattern for the model at 100 tons (its "yield" load) compares well with Fig. 4.18. However, at higher loads the cracking pattern for the model differs from that of the specimen, showing continued growth of cracks in the upper right hand corner of the shear wall.

The fact that the crack patterns differ, while at the same time the overall load-deflection behavior is similar, may be explained by a facet of specimen A-1 that was not modeled analytically. As indicated in Fig. 4.13, the reinforcing steel in the columns and the beams was concentrated away from the member centerlines. This non-uniform distribution of steel was not included in the finite element model. Had the steel in the model been shifted toward the extreme fibers of these members, the columns would have been stiffer under lateral load. While this would not have affected the overall system appreciably, it would have affected the local interaction of the individual structural members and suppressed the cracks in the upper right portion of the wall to some degree.

Another facet of specimen A-1 that was not modeled correctly at first was the location of the center load points. Figure 4.13 shows that the center load points are displaced 17.5 cm from the specimen centerline. Initially the two loads were modeled as a single concentrated load at the center of the specimen. The resulting analysis indicated that extensive cracking should have occurred in the left-hand side of the upper column and in the upper

portion of the foundation. When the model loading was changed to simulate the test more accurately, as shown in Fig. 4.14, these cracks were suppressed. The load-deflection behavior, however, did not change an appreciable amount.

4.3 Cyclic Loading

4.3.1 Shear Panel--Cervenka and Gerstle

The reinforced concrete structure considered in this section is shear panel W-4 from the tests performed by Cervenka and Gerstle (8,10). This shear panel is similar to those discussed in Section 4.2.2; the panel thickness was three inches and reinforced as shown in Fig. 4.20a. The test specimen was cycled four times at low stresses and then cycled to failure at a load calculated by Cervenka to be 88 percent of the monotonic load limit. For this test, a cycle consisted of first loading and then unloading in a single direction. The results of the "plastic" cycling are shown in Fig. 4.21 along with the results of the analysis by Cervenka and Gerstle. Their analysis, which utilized elasto-plastic material properties, allowed only single cracking at a point, and used a grid of 70 constant strain triangle finite elements, fell far short of their goal of modeling the load-deflection behavior of this panel.

The proposed model for panel W-4 is shown in Fig. 4.20b, and consists of 24 elements with 9 integration points each. The analytical model was loaded with imposed nodal displacements as shown. The boundary conditions at the center rib were varied for each cycle to duplicate those in the actual test. The analytical load-deflection curve is compared to the actual curve for the first two and a half cycles (Fig. 4.22). The agreement with the test

curve is good and essentially duplicates the behavior of the shear panel. The fact that the finite element model appears to be slightly softer than the test specimen, for positive cycles at least, may be due to the fact that the nodal displacement was imposed at the edge rather than at the center of the outside rib.

The analytical crack pattern after two and one-half cycles is compared with that of test specimen W-4 after ten cycles in Fig. 4.23.

The proposed model succeeded where that of Cervenka and Gerstle failed, probably because of several reasons. First, although their model contained 70 finite elements as compared to 24 for the proposed model, the nine integration points per element for the proposed model gave a finer grid that allowed the state of the material to be followed at more points within the panel. Preliminary work in this study indicated that this was of some importance. Cervenka (8) considered this problem when he lowered the "monotonic load limit," calculated with the 70 element grid, from 28 kips to 26 kips, based on other analytical work that he had done. He did not account for the coarse grid when he selected the limits for cycling the analytical model.

A second reason for their lack of success, pointed out by Cervenka (8), was the fact that their model allowed for only one open crack within each element. In this investigation it was found that a significant portion of the cracks remained open, even when the cycle was reversed. This matches the experimental evidence.

Cervenka offered two other possible reasons for his inability to model this test. His model did not consider bond slip or crack deterioration. The proposed model does not include bond slip, but it does include "crack

deterioration" if a crack is closed and the concrete is reloaded above the common point (Sections 2.2.5 and 2.2.6).

One point which Cervenka did not consider, which may be the most important reason why the proposed model succeeded, while that of Cervenka and Gerstle failed, is that the "elasto-plastic" model remains elastic in compression until the yield surface is reached, whereas the proposed model becomes strongly nonlinear in compression for stresses above about 0.7 f_c'. As shown in Fig. 4.23c, on all three cycles, portions of the concrete near the center rib had stresses exceeding 0.8 f_c'. On the negative cycle, and the second positive cycle, portions of the concrete were actually on the downward portion of the stress-strain curve. Since these material points represented the only uncracked concrete adjacent to the center rib, the nonlinear behavior of the proposed model in compression must be considered to be a major factor in the close match obtained.

Initial work in this investigation, not included in this report, indicates that displacement control gives a more accurate duplication of experimental tests for cyclic loading than does load control. It is likely that Cervenka and Gerstle's model would have given a significantly better match with the initial cycle of "plastic" loading if displacement control had been used. It is not expected, however, that the subsequent cyclic behavior of their model would have been improved, due to other limitations discussed above (e.g., only one open crack per element).

Chapter 5

SUMMARY AND CONCLUSIONS

5.1 Summary

An inelastic constitutive model for cyclic, biaxial loading of reinforced concrete is presented in which the material properties of the concrete and the reinforcing steel are modeled. The individual models are combined to form a "composite" material used in conjunction with the finite element technique to analyze the behavior of reinforced concrete structures.

The constitutive model for plain concrete is developed to match experimental data on monotonic biaxial and cyclic uniaxial loading. The model is extended to cover cyclic biaxial loading and multi-directional cracking. The resulting model is compared with existing material tests on concrete.

The reinforcing steel is modeled as a bilinear uniaxial material that exhibits both strain-hardening and the Bauschinger effect. When combined with the model for concrete, the steel is "smeared" rather than being treated as discrete reinforcing bars.

With the exception of the initial calculation of "crack width", bond slip is not considered. The stresses in the concrete and steel at a material point are considered separately, with the strains assumed to be the same in both. Time and temperature effects are not considered.

The constitutive models are combined with the finite element technique to model reinforced concrete structures that may be considered to be in a state of plane stress. A four noded quadrilateral isoparametric

element with four extra nonconforming degrees of freedom is used. An incremental method of nonlinear analysis is presented in which either loads or displacements may be prescribed. Convergence criteria are discussed and special techniques for handling the closing of cracks and the downward portion of the concrete stress-strain curve are described.

Numerical examples are presented in which the proposed model is compared with experimental tests of several reinforced concrete members and one reinforced concrete structural system under monotonically increasing load. The model is also used to duplicate the experimental behavior of a reinforced shear panel under cyclic load.

5.2 Conclusions

The proposed constitutive model for reinforced concrete gave satisfactory results for both material simulation and structural analysis.

The model gives a good match with experimental results for monotonic biaxial loading of plain concrete. The model also compares well with material tests of concrete under cycles of uniaxial compressive load. The model gives conservative values for energy loss for cycles of low compressive strain, but good results for values of compressive strain above about eighty percent of the strain at f'_c. The constitutive model also compares well with the total number of cycles to a fixed stress that are necessary to cause failure.

The constitutive model for reinforcing steel gives generally conservative values for strength and energy loss for cyclic loading.

The numerical examples of reinforced concrete members demonstrate that the constitutive model, when combined with the finite element technique,

is quite useful for analyzing structures of this type. These examples indicate that a good match with structural behavior is obtained by combining the individual constitutive properties of the concrete and steel to form a "composite" material. The "smearing" technique provides satisfactory results when the steel is distributed within the analytical model in a manner similar to that in the prototype structure. Good matches with test data are obtained for the numerical examples presented without any need to model bond slip between the steel and the concrete.

The concept of equivalent uniaxial strain gives reasonable results for both monotonic and cyclic loading.

While a concrete tensile strength that varied with compressive stress gave the best results for material simulation, a constant tensile strength was satisfactory for structural modeling. Values of tensile strength equal to the modulus of rupture and the splitting tensile strength were used successfully for structural problems.

The results of the shear wall-frame system analysis indicate that modeling of boundary conditions and steel distribution may be very important in determining the analytical crack pattern, if not the overall behavior of the structure being analyzed.

As demonstrated by the shear panel subjected to cyclic load, the nonlinear nature of the analytical stress-strain curve in compression seems to be an important aspect in modeling structural behavior.

5.3 Recommendations for Further Study

The techniques presented in this report are designed to be used

with a broader category of structures than the examples presented. The constitutive model should find application in the study of folded plates, slabs, shells, and reactor containment vessels. The model should also prove to be a useful tool for investigating the behavior of reinforced concrete structures under seismic loading. The built-in hysteresis behavior is designed to provide the energy loss that is usually accounted for by adding damping terms to the dynamic analysis.

Further work is also indicated in the area of constitutive models. The model presented in this report is limited to structures in which the concrete is in a state of plane stress. The proposed model should be extended or new models should be developed that consider triaxial states of stress in concrete, including the effect of confinement provided by shear reinforcement, an area not considered in this investigation.

Concurrent with the need to extend existing analytical models, and in many ways necessary for that extension, is the need to expand the available information on the behavior of concrete and steel. Two areas of immediate interest are the investigation of the behavior of concrete for loading paths in which both the principal directions and the ratio of principal stresses change, and the study of concrete when it is subjected to cycles of biaxial load. These areas appear to be the next logical steps toward a better understanding of the behavior of reinforced concrete through a better understanding of the behavior of its constituent materials.

REFERENCES

1. Aktan, A. E., Karlsson, B. I. and Sozen, M. A., "Stress-Strain Relationships of Reinforcing Bars Subjected to Large Strain Reversals," SRS No. 397, Civil Engineering Studies, University of Illinois, Urbana-Champaign, Illinois, June 1973.

2. Aktan, A. E. and Pecknold, D.A.W., "Response of a Reinforced Concrete Section to Two-Dimensional Curvature Histories," Journal ACI, Proc. V. 71, No. 5, May 1974, pp. 246-250.

3. Aktan, A. E., Pecknold, D.A.W. and Sozen, M. A., "Effects of Two-Dimensional Earthquake Motion on a Reinforced Concrete Column," SRS No. 399, Civil Engineering Studies, University of Illinois, Urbana-Champaign, Illinois, May 1973.

4. American Concrete Institute, "Building Code Requirements for Reinforced Concrete (ACI 318-71)," Nov. 1971.

5. Bell, J. C., "A Complete Analysis of Reinforced Concrete Slabs and Shells," Ph.D. Thesis, University of Canterbury, Christchurch, New Zealand, 1970.

6. Blakely, R.W.G. and Park, R., "Prestressed Concrete Sections with Cyclic Flexure," Journal Struct. Div., ASCE, Vol. 99, No. ST8, Aug. 1973, pp. 1717-1742.

7. Burns, N. H. and Siess, C. P., "Load-Deformation Characteristics of Beam-Column Connections in Reinforced Concrete," SRS No. 234, Civil Engineering Studies, University of Illinois, Urbana-Champaign, Illinois, Jan. 1962.

8. Cervenka, V., "Inelastic Finite Element Analysis of Reinforced Concrete Panels Under In-Plane Loads," Ph.D. Thesis, University of Colorado, Boulder, Colorado, 1970.

9. Cervenka, V. and Gerstle, K. H., "Inelastic Analysis of Reinforced Concrete Panels, Part I: Theory," IABSE Publications, Vol. 31-II, 1971, pp. 31-45.

10. Cervenka, V. and Gerstle, K. H., "Inelastic Analysis of Reinforced Concrete Panels, Part II: Experimental Verification and Application," IABSE Publications, Vol. 32-II, 1972, pp. 25-39.

11. Franklin, H. A., "Nonlinear Analysis of Reinforced Concrete Frames and Panels," Ph.D. Thesis, University of California, Berkeley, California, 1970.

12. Gupta, A. K., Mohraz, B. and Schnobrich, W. C., "Elasto-Plastic Analysis of Three Dimensional Structures Using the Isoparametric Element," SRS No. 381, Civil Engineering Studies, University of Illinois, Urbana-Champaign, Illinois, Aug. 1971.

13. Hand, F. R., Pecknold, D. A. and Schnobrich, W. C., "Nonlinear Layered Analysis of RC Plates and Shells," Journal Struct. Div., ASCE, Vol. 99, No. ST7, July 1973, pp. 1491-1505.

14. Irons, B. M. and Razzaque, A., "Experience with the Patch Test for Convergence of Finite Elements," The Mathematical Foundations of the Finite Element Method with Applications to Partial Differential Equations, ed. Aziz, A. K., Academic Press, New York and London, 1972.

15. Jofriet, J. C. and McNeice, G. M., "Finite Element Analysis of Reinforced Concrete Slabs," Journal Struct. Div., ASCE, Vol. 97, No. ST3, Mar. 1971, pp. 785-806.

16. Karsan, I. D., "Behavior of Plain Concrete Under Variable Load Histories," Ph.D. Thesis, Rice University, Houston, Texas, May 1968.

17. Karsan, I. D. and Jirsa, J. O., "Behavior of Concrete Under Compressive Loadings," Journal Struct. Div., ASCE, Vol. 95, No. ST12, Dec. 1969, pp. 2543-2563.

18. Kent, D. C. and Park, R., "Flexural Members with Confined Concrete," Journal Struct. Div., ASCE, Vol. 97, No. ST7, July 1971, pp. 1969-1990.

19. Kupfer, H. B. and Gerstle, K. H., "Behavior of Concrete Under Biaxial Stresses," Journal Engr. Mech. Div., ASCE, Vol. 99, No. EM4, Aug. 1973. pp. 852-866.

20. Kupfer, H., Hilsdorf, H. K. and Rusch, H., "Behavior of Concrete Under Biaxial Stresses," Journal ACI, Proc. V. 66, No. 8, Aug. 1969, pp. 656-666.

21. Lin, C. S., "Nonlinear Analysis of Reinforced Concrete Slabs and Shells," Ph.D. Thesis, University of California, Berkeley, California, 1972.

22. Liu, T.C.Y., "Stress-Strain Response and Fracture of Concrete in Biaxial Compression," Ph.D. Thesis and Research Report No. 339, Dept. of Struct. Engr., Cornell University, Ithaca, N.Y., Feb. 1971.

23. Liu, T.C.Y., Nilson, A. H. and Slate, F. O., "Stress-Strain Response and Fracture of Concrete in Uniaxial and Biaxial Compression," Journal ACI, Proc. V. 69, No. 5, May 1972, pp. 291-295.

24. Liu, T.C.Y., Nilson, A. H. and Slate, F. O., "Biaxial Stress-Strain Relations for Concrete," Journal Struct. Div., ASCE, Vol. 98, No. ST5, May 1972, pp. 1025-1034.

25. Mikkola, M. J. and Schnobrich, W. C., "Material Characteristics for Reinforced Concrete Shells Stressed Beyond the Elastic Range," SRS No. 367, Civil Engineering Studies, University of Illinois, Urbana-Champaign, Illinois, Aug. 1970.

Table 2.1

Variables Used to Define Material Models

Model	Proposed	Kupfer & Gerstle (19)	Lin, Nilson & Slate (23)
Experimental			
Kupfer, Hilsdorf, and Rusch (20) β_p = -328 kp/cm^2 (4650 psi)	f_c' = -4650 psi ε_{cu} = -0.00216 in./in. f_t' = 430 psi E_o = 4.78 x 10^6 psi	f_{cu} = -4650 psi (modeled after curves for concrete with f_{cu} = -324 kp/cm^2 (f_{cu} = -4600 psi)	σ_o = -4650 psi E = 4.78 x 10^6 psi
Nelissen (26) (1%/100' in σ_1 - direction; K350)	f_c' = -315 kp/cm^2 ε_{cu} = -.0022 cm/cm f_t' = 16 kp/cm^2 E_o = 3.45 x 10^5 kp/cm^2	f_{cu} = -315 kp/cm^2 (modeled after curves for concrete with f_{cu} = -324 kp/cm^2)	σ_o = -315 kp/cm^2 E = 3.45 x 10^5 kp/cm^2

Table 2.2

Number of Cycles of Compressive Load Between Fixed Values of Stress Required to Intercept the Envelope Curve

Maximum Stress as a Percentage of Specimen Strength*	Minimum Stress as a Percentage of Specimen Strength	Cycles to "Failure"				
		Karsan & Jirsa (16,17)	Proposed Model**			
			$\sigma_{cp}=\frac{9}{10}\sigma_{en}$	$\sigma_{cp}=\frac{17}{20}\sigma_{en}$	$\sigma_{cp}=\frac{5}{6}\sigma_{en}$ ***	$\sigma_{cp}=\frac{4}{5}\sigma_{en}$
95	0	5	23	13	12	9
93	0	17	NF	19	16	13
91	0	21	NF	27	22	17
Maximum Percentage of Specimen Strength at Which No Additional Strain is Accumulated Between Cycles		~74	90	85	83	80

* Specimen strength was approximately .85 f'_c ($f'_c \simeq$ 3660 to 3950 psi)

** Additional information presented in Section 2.2.5

*** Used in model

NF = No failure after 31 cycles

Table 2.3

Energy Dissipated for a Single Cycle of Uniaxial Compressive Load as a Function of the Envelope Strain

Envelope Strain as a Fraction of Strain at Maximum Stress $\varepsilon_{en}/\varepsilon_{cu}$	Karsan and Jirsa (17)			Proposed Model	
	Specimen	Cycle	Energy* (Experimental)	Energy* (Analytical)	Analytical / Experimental
.54	AC3-10	3	2.72	1.24	0.46
.59	AC4-10	2	2.46	1.65	0.67
.64	AC4-12	2	3.05	2.04	0.67
.81	AC3-10	4	4.44	3.40	0.77
.86	AC2-09	2	4.37	3.90	0.89
1.10	AC3-10	5	5.14	5.48	1.07
1.45	AC2-09	4	5.92	6.01	1.02
1.62	AC3-10	7	4.66	5.80	1.24
2.69	AC2-09	6	7.16	7.00	0.98

Specimen	f'_c
AC2-09	- 3370 psi
AC3-10	- 5010 psi
AC4-10	- 3950 psi
AC4-12	- 3760 psi

*Relative units

Table 4.1

Material Properties for Structural Tests

Investigators	Specimen Designation	Concrete					Steel			Type Nominal Area
		E_o	f'_c	ε_{cu}	f'_t		f_y	E_{steel}	$\frac{E_{sh}}{E_{steel}}$	
Burns & Siess (7)	J-4	3.8×10^6* psi	-4820 psi	-.0022*	546 psi		44,900 psi	27×10^6* psi	.005*	#8(.79 in.^{2}) #3(.11 in.^{2})
Cervenka & Gerstle (8,9,10)	W-1	2.9×10^6 psi	-3580 psi	-.0025	470[1] psi	PANEL & X-RIB	33,000 psi	27×10^6 psi	.00541	9Ga(.0173 in.^{2})
						Y-RIB	51,200 psi	27.3×10^6 psi	.0092	#3 Bars (.11 in.^{2})
	W-2	2.9×10^6 psi	-3649 psi (-3650)**	-.0025	529[1] psi (530)		51,200 psi	27.3×10^6 psi	.0092	#3 Bars[2] (.11 in.^{2})
	W-4	2.9×10^6 psi	-3544 psi (-3540)	-.0025	512[1] psi (510)		51,200 psi	27.3×10^6 psi	.0092	#3 Bars[2] (.11 in.^{2})
Umemura, Aoyama, Liao (38)	A-1	2.98×10^5 kp/cm^2[3]	-237 kp/cm^2	-.00159 (-.0016)	40* kp/cm^2		3,420 kp/cm^2	1.9×10^6* kp/cm^2	.005*	6ϕ (.238 cm^2)
							4,770	1.9×10^6*	.005*	D16(2.01 cm^2)

* **Assumed

Numbers in parenthesis show values used in analysis, if different from those shown.

[1] Splitting tensile strength

[2] 9Ga bars also in rib--assigned same properties as #3 bars for analysis

[3] Secant modulus at .25 f'_c

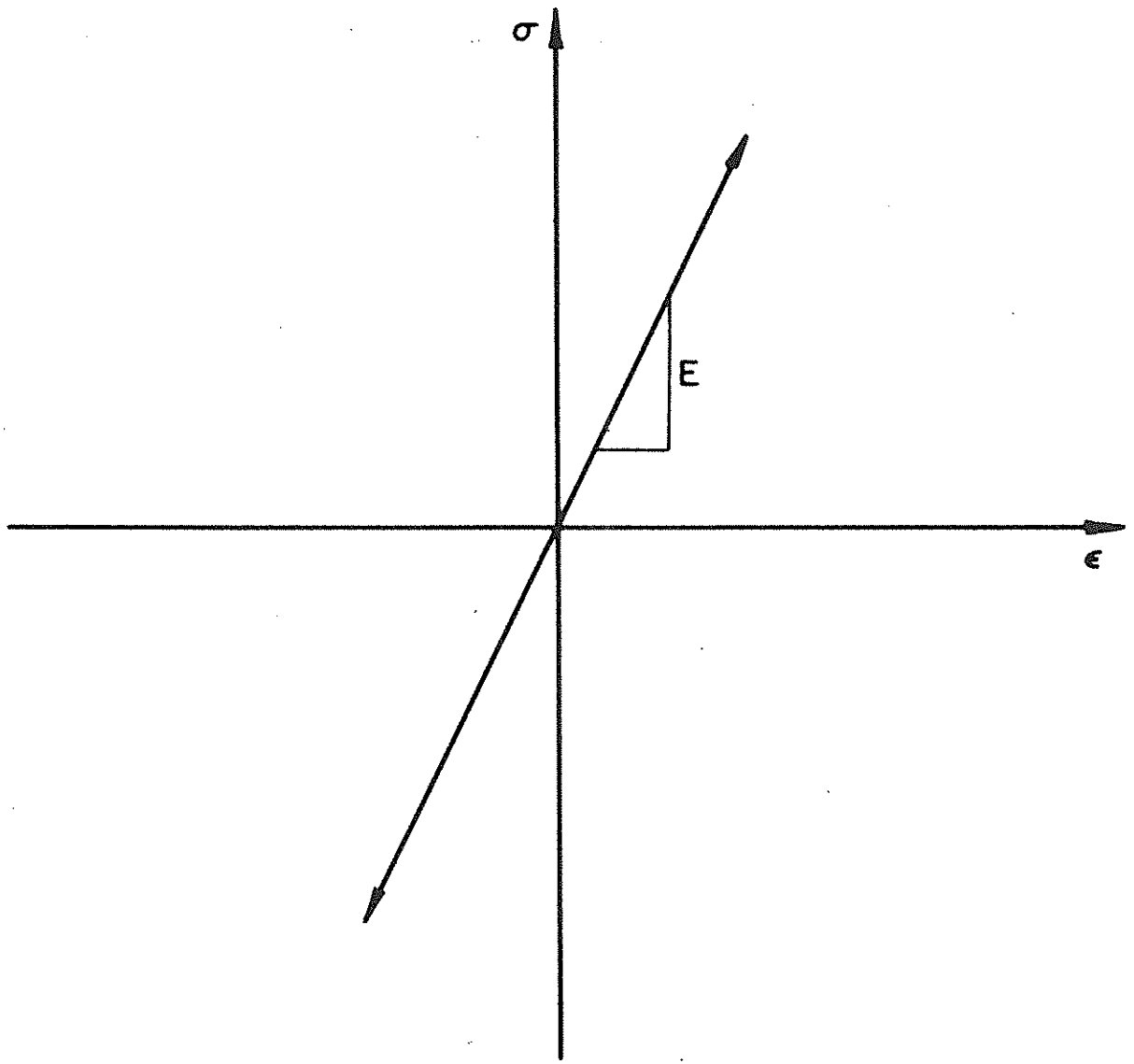

Figure 2.1 Linear Elastic Representation for Concrete and Steel

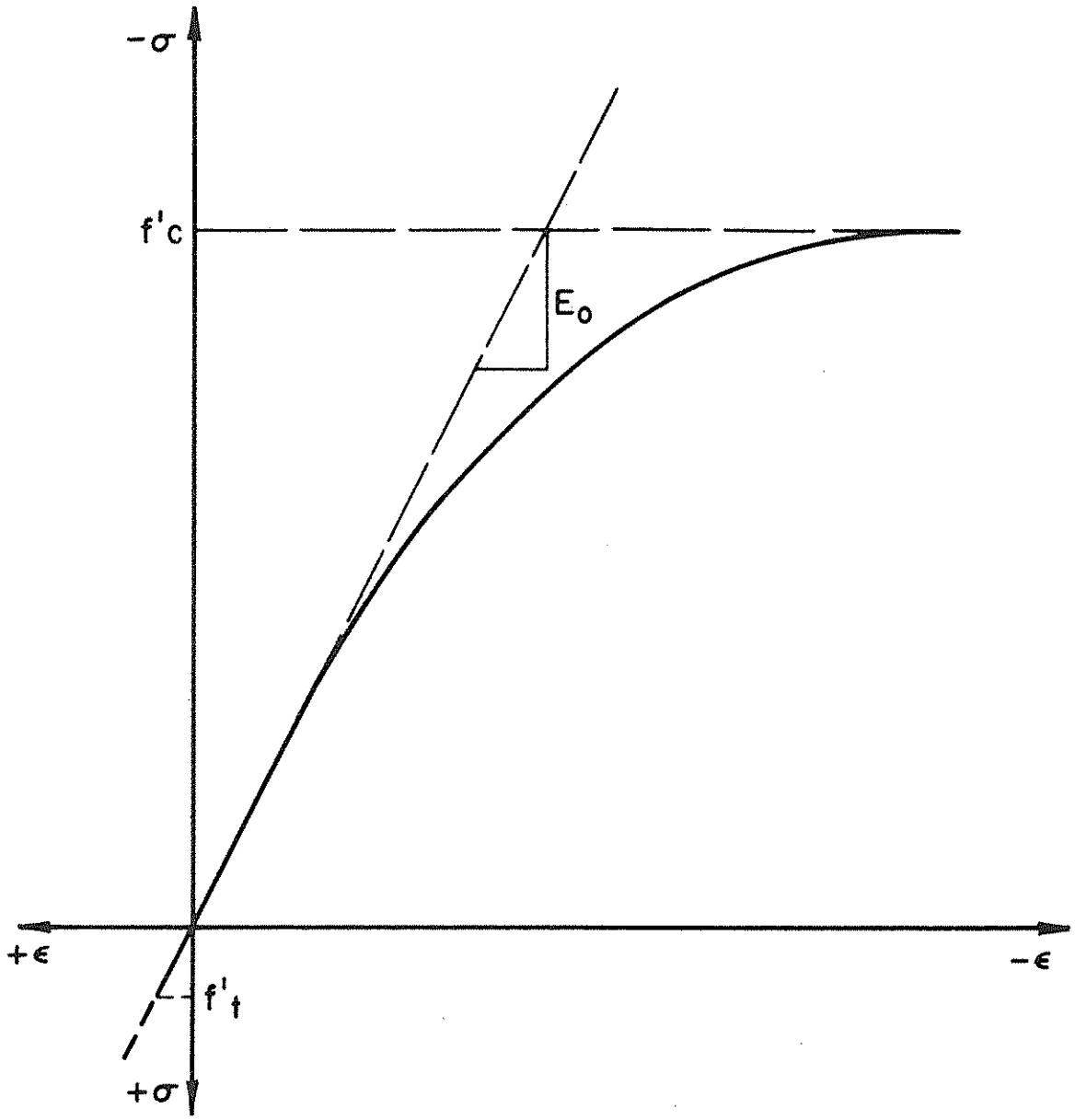

Figure 2.2 Typical Stress-Strain Curve for Plain Concrete Under Uniaxial Compression or Tension

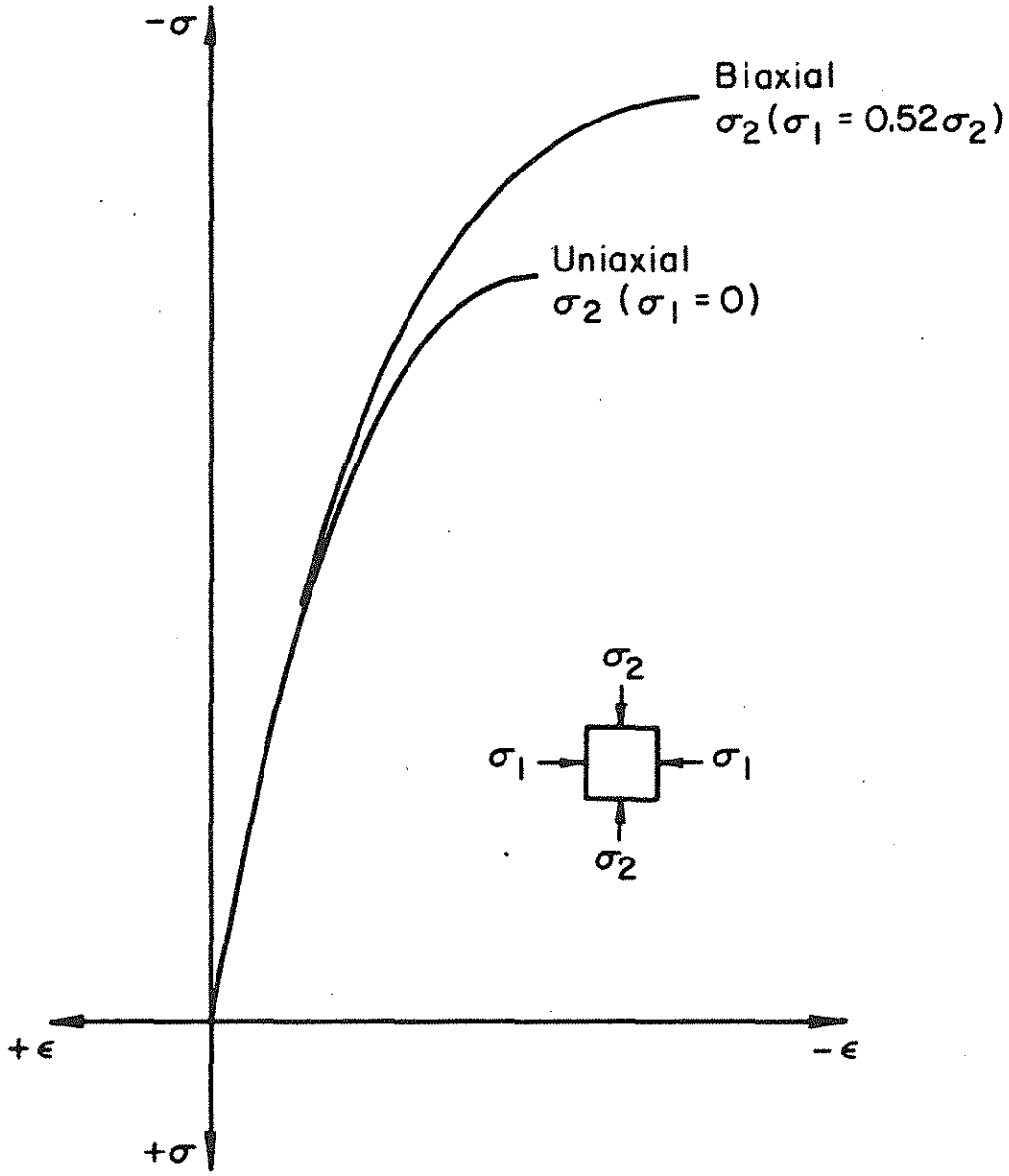

Figure 2.3 Effect of Biaxial Stress State on Behavior of Plain Concrete

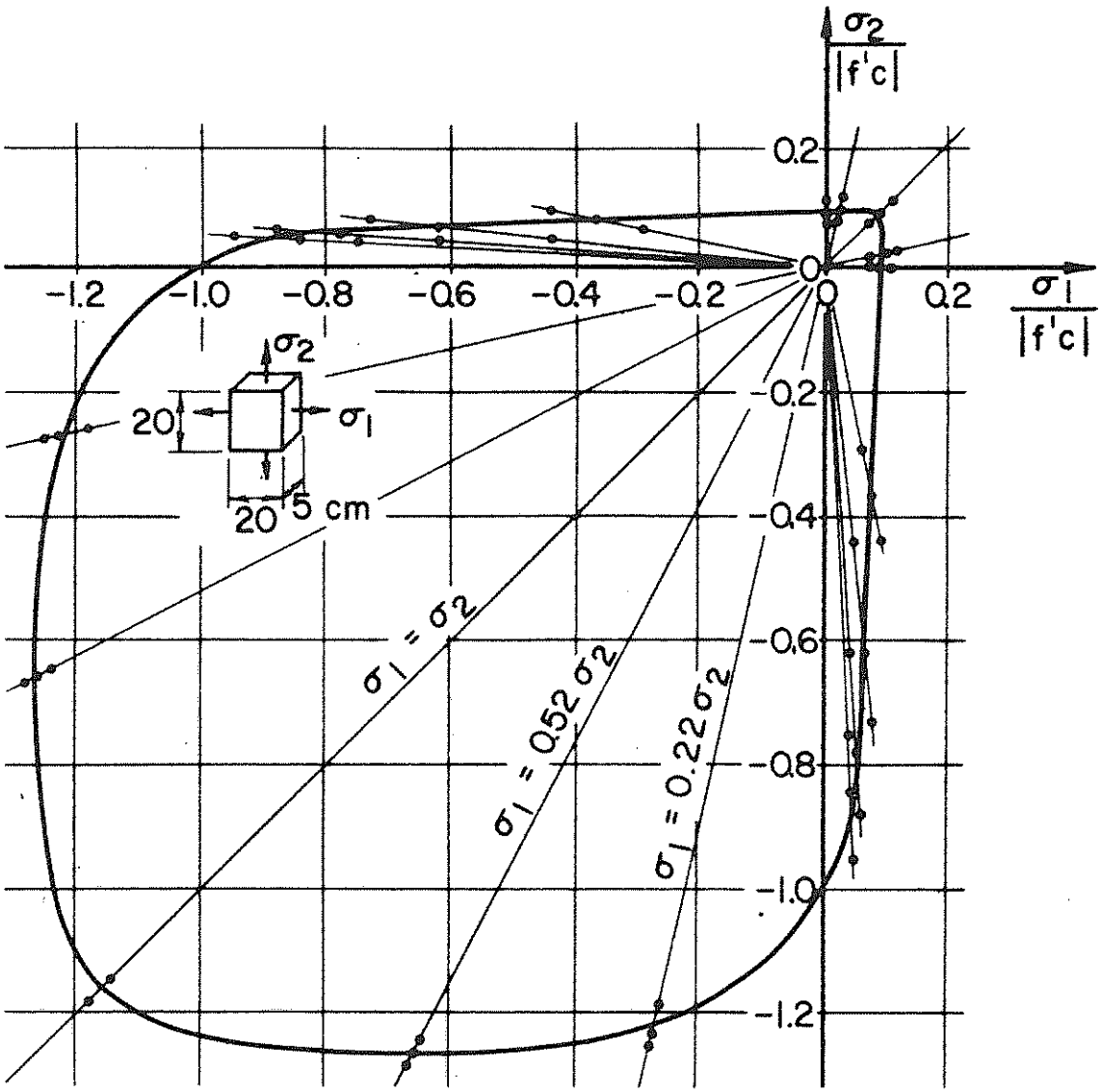

Figure 2.4 Biaxial Strength of Concrete (20)

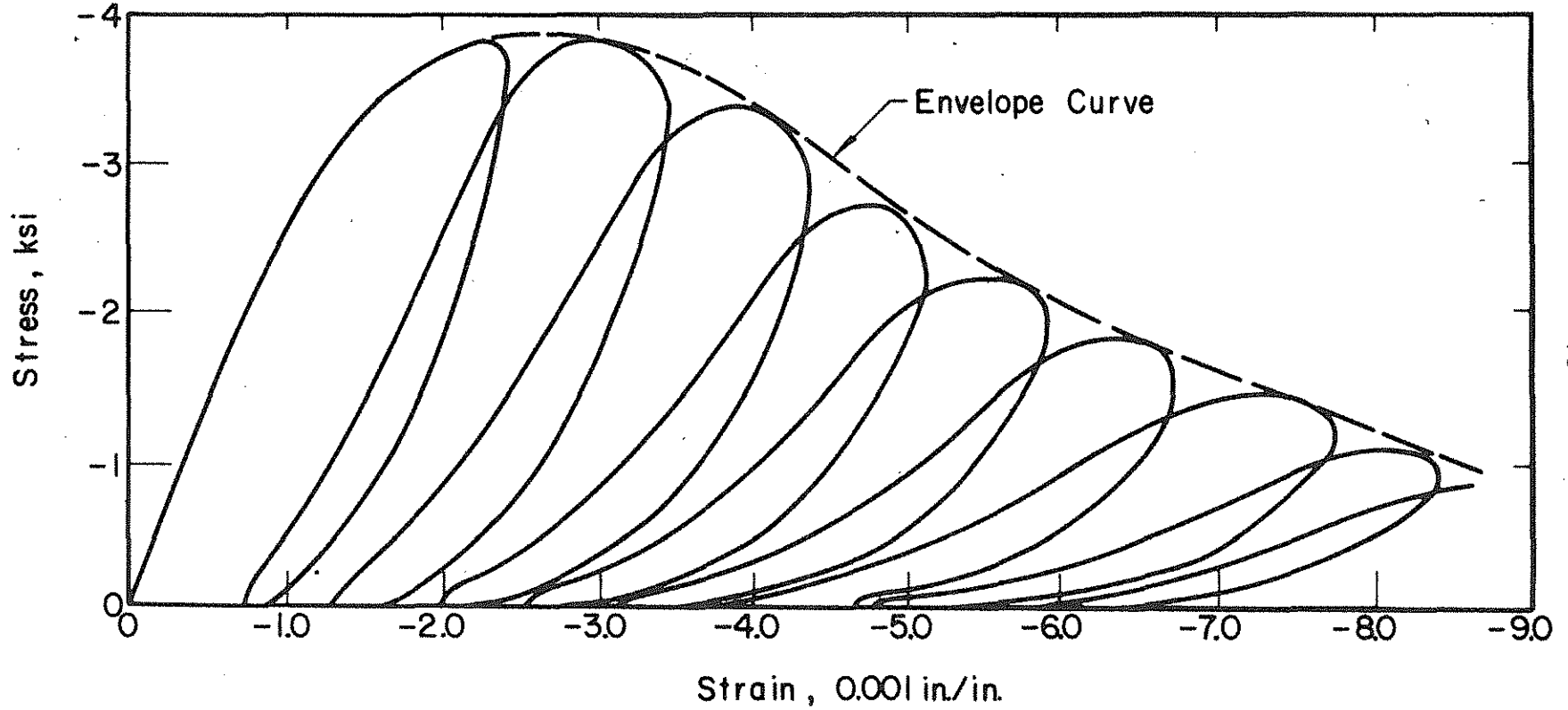

Figure 2.5 Behavior of Concrete Under Cycles of Compressive Loading (35)

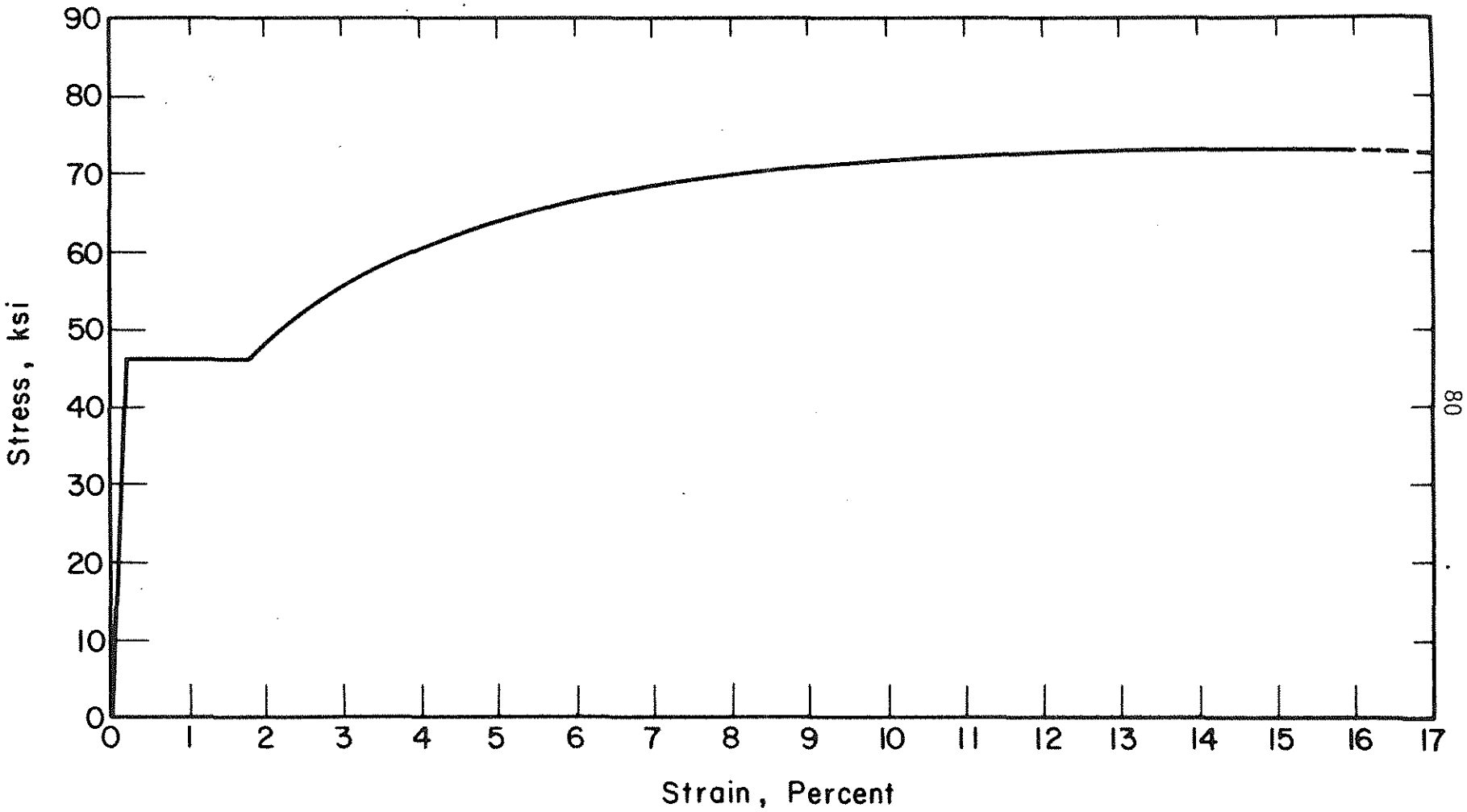

Figure 2.6 Typical Stress-Strain Curve for Reinforcing Steel Under Monotonic Load (7)

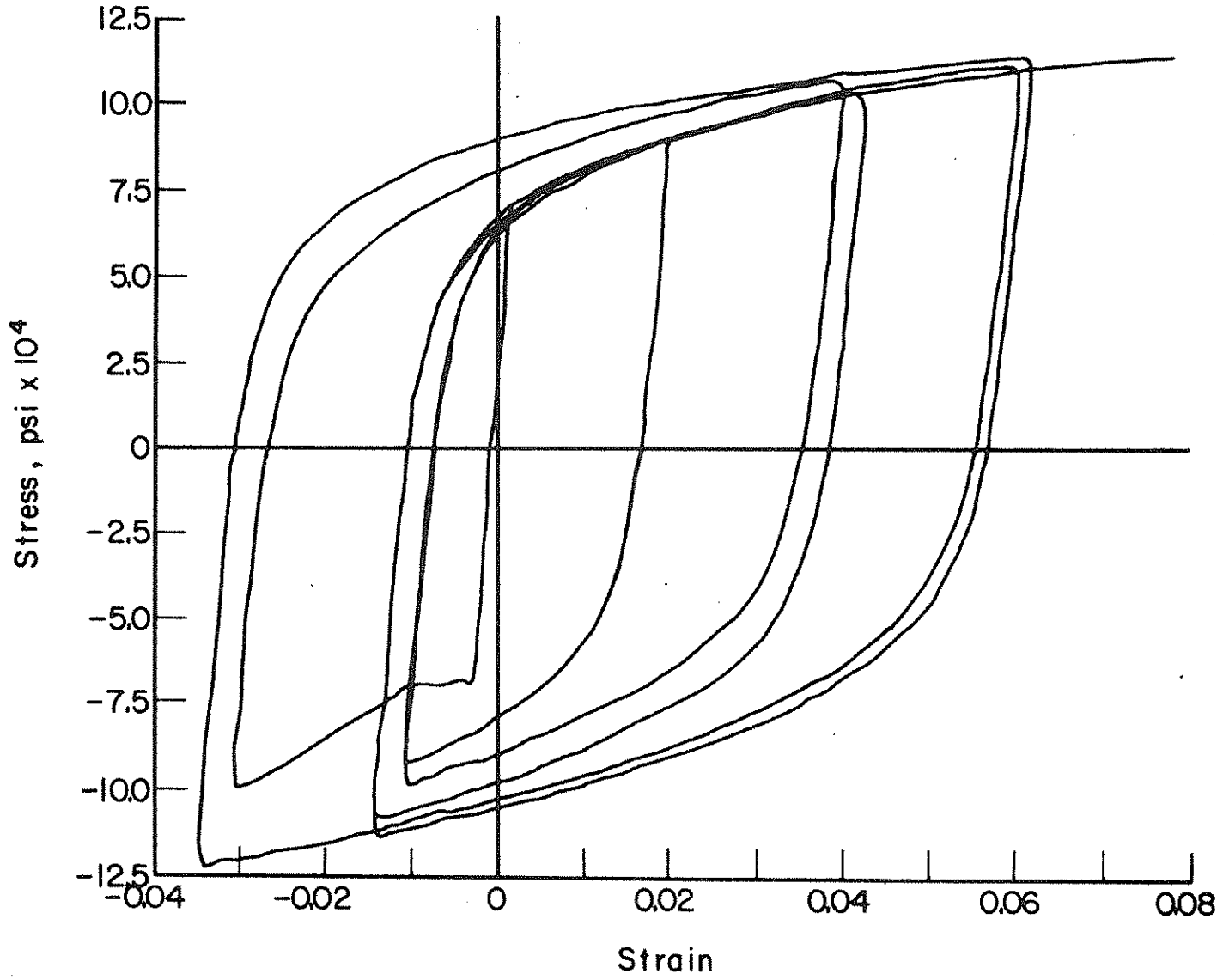

Figure 2.7 Behavior of Reinforcing Steel Under Cycles of Load (1)

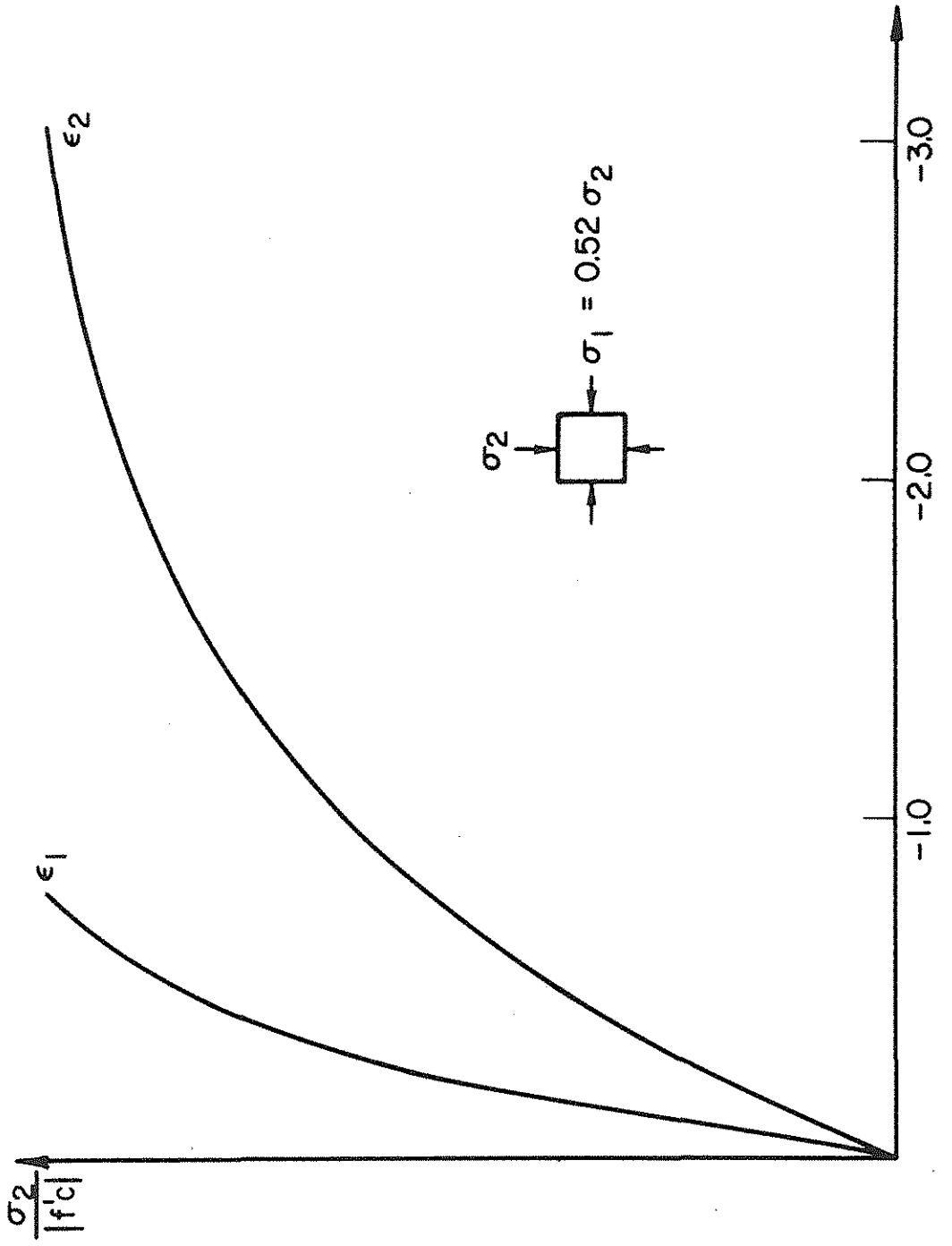

Figure 2.8 Behavior of Plain Concrete Under Biaxial Compression (20)

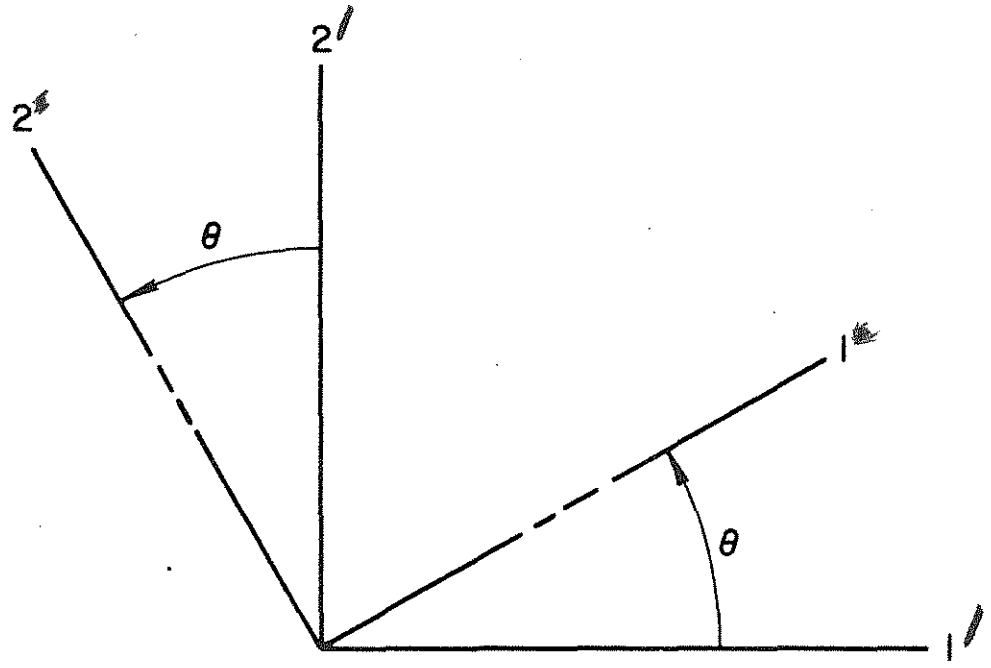

Figure 2.9 Rotation of Axes

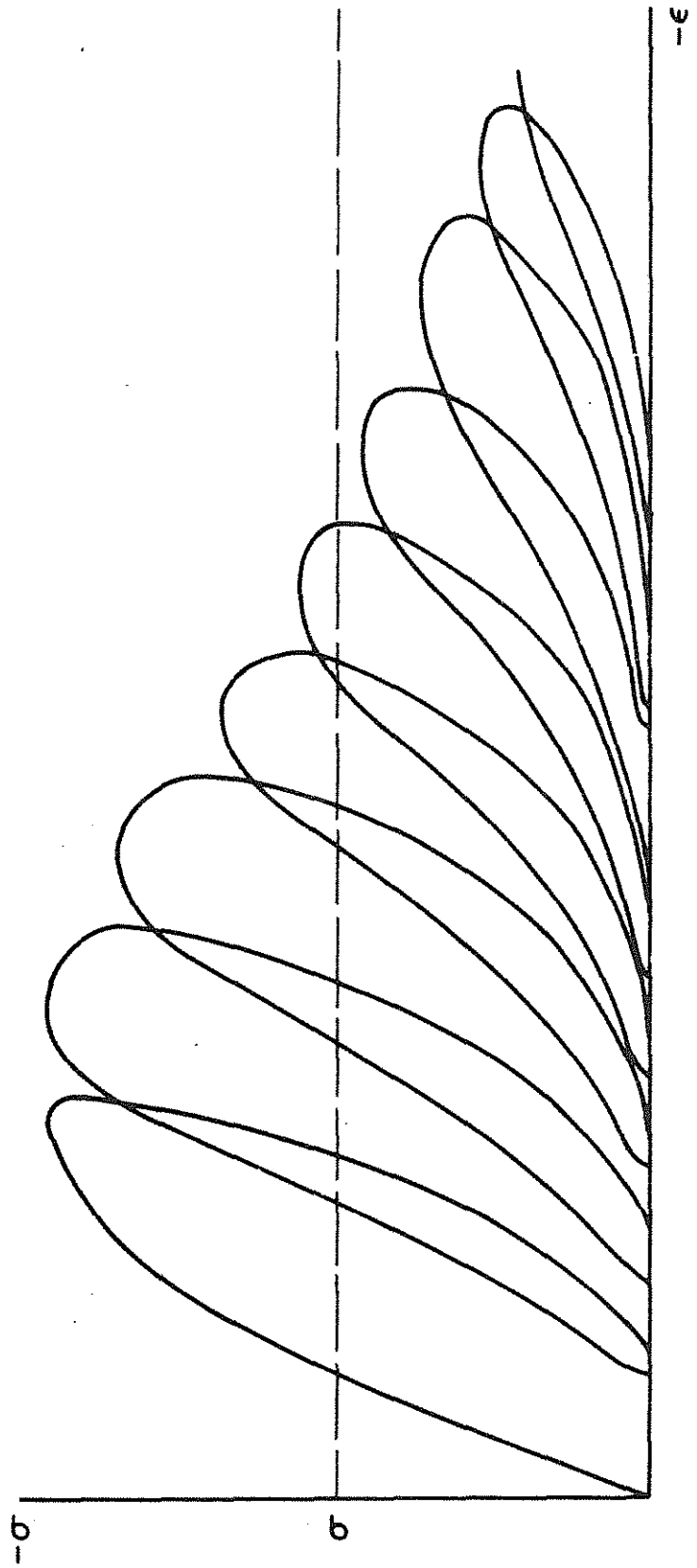

Figure 2.10 Cyclic Loading of Concrete

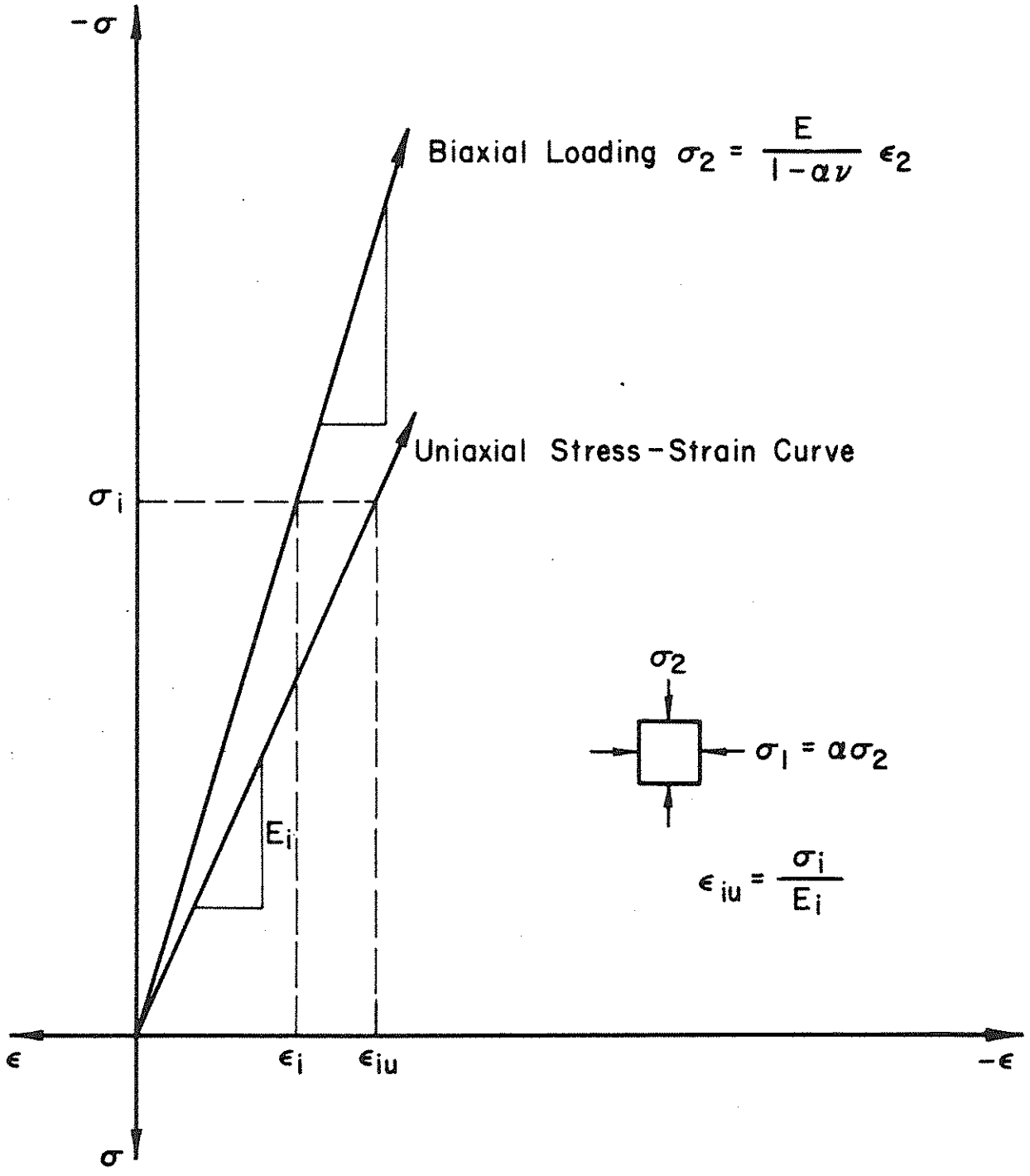

Figure 2.11 Equivalent Uniaxial Strain, ϵ_{iu}, for Linear Material

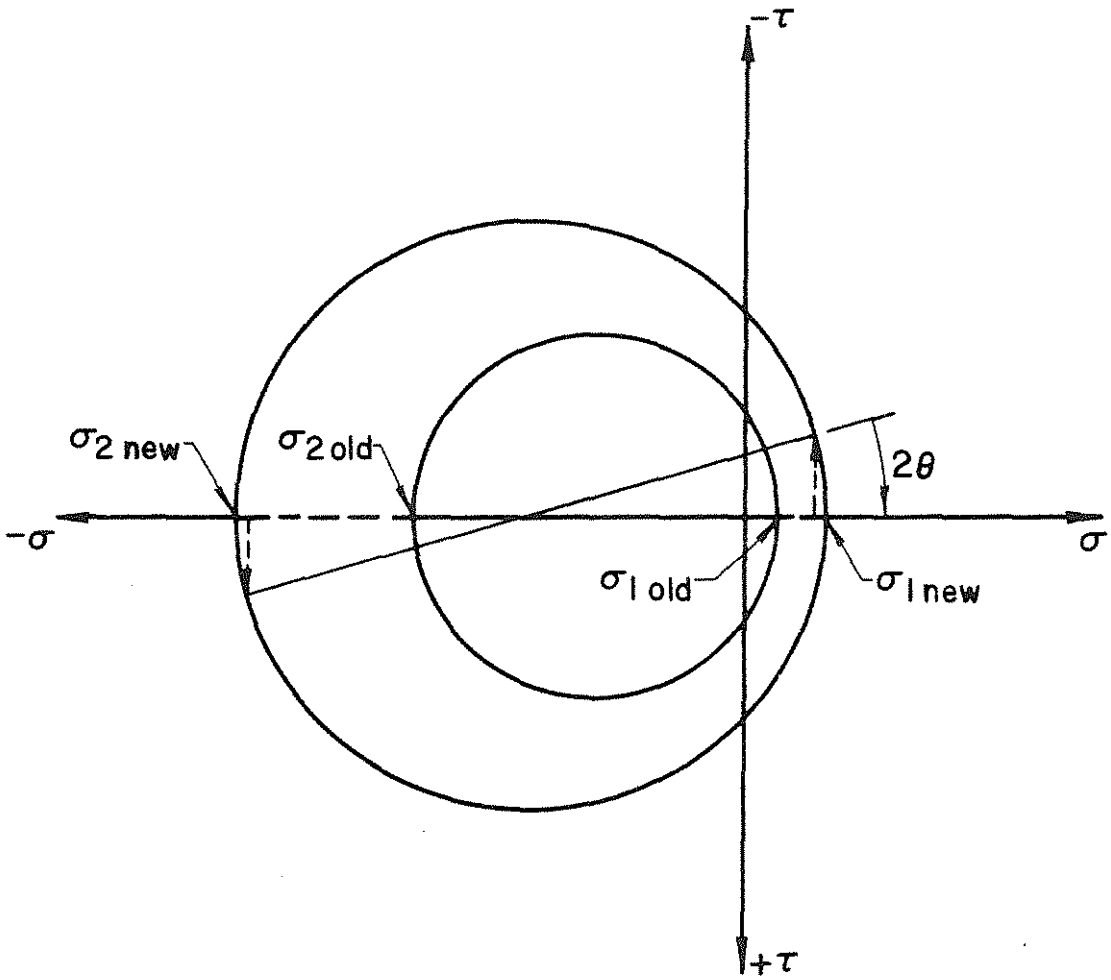

Figure 2.12a Rotation of Principal Stress Axes

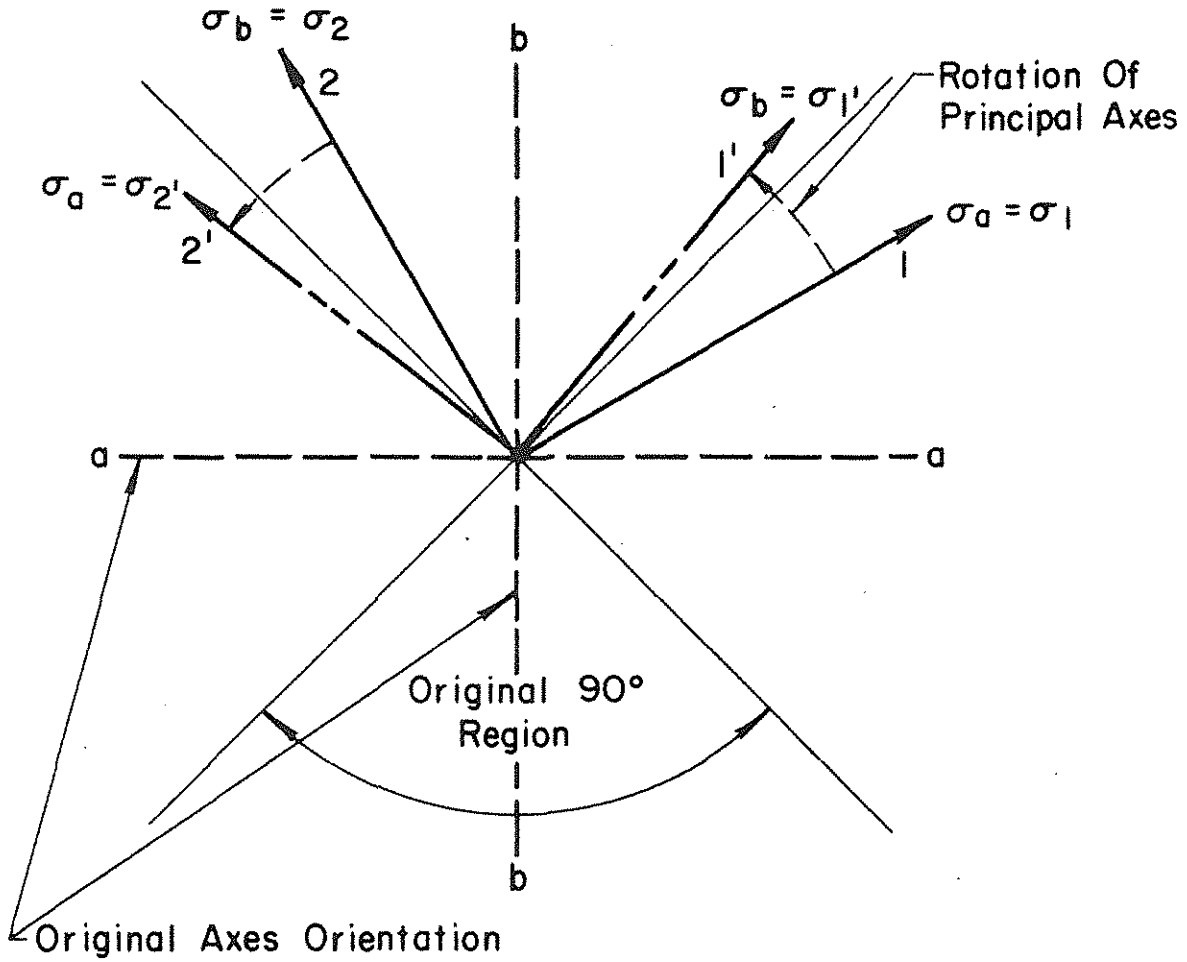

Before Rotation	After Rotation
1 Axis Associated W/Region a	1' Axis Associated W/Region b
2 Axis Associated W/Region b	2' Axis Associated W/Region a

Figure 2.12b Rotation of Principal Axes Out of Originally Defined Regions

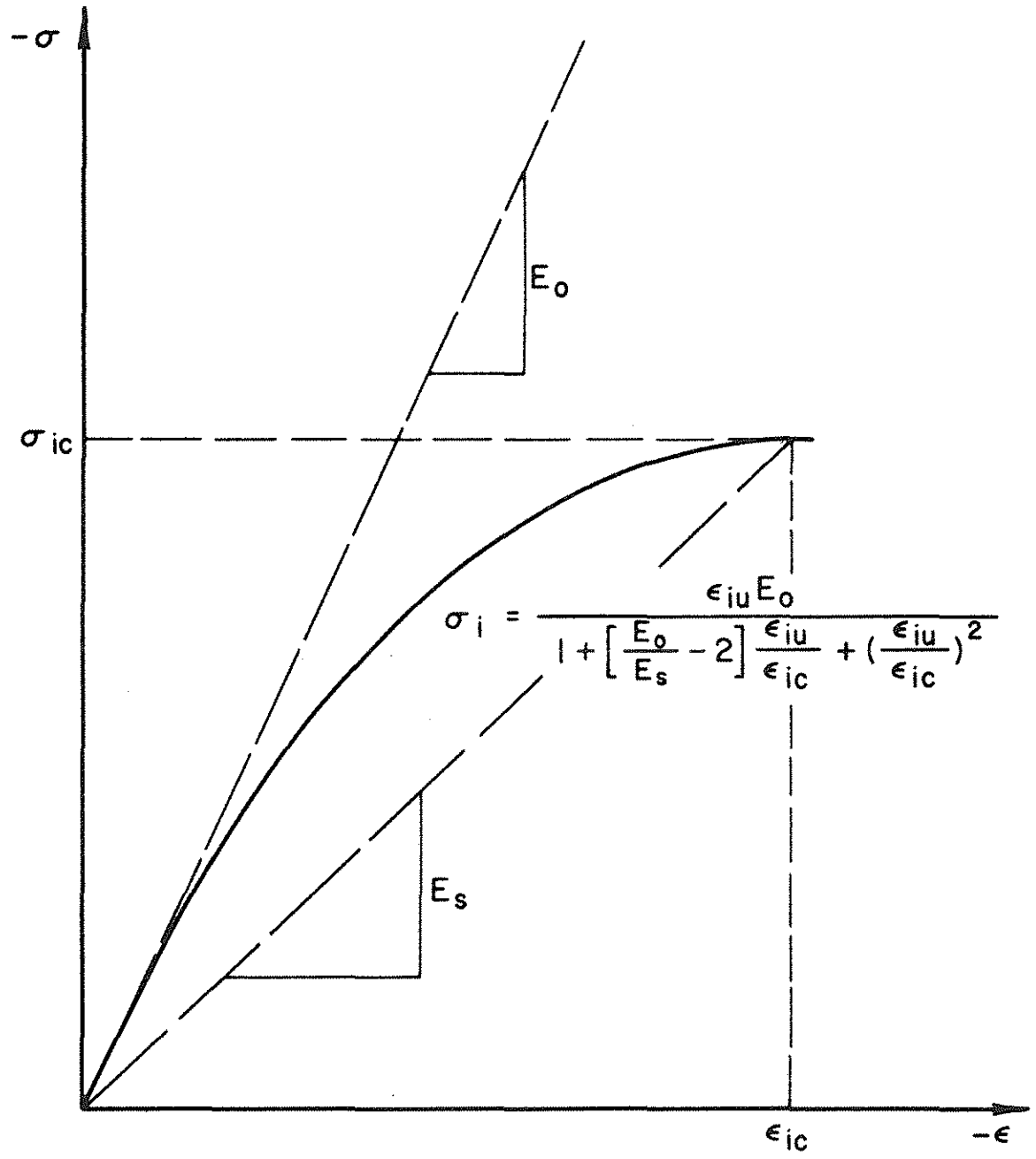

Figure 2.13 Equivalent Uniaxial Stress-Strain Curve

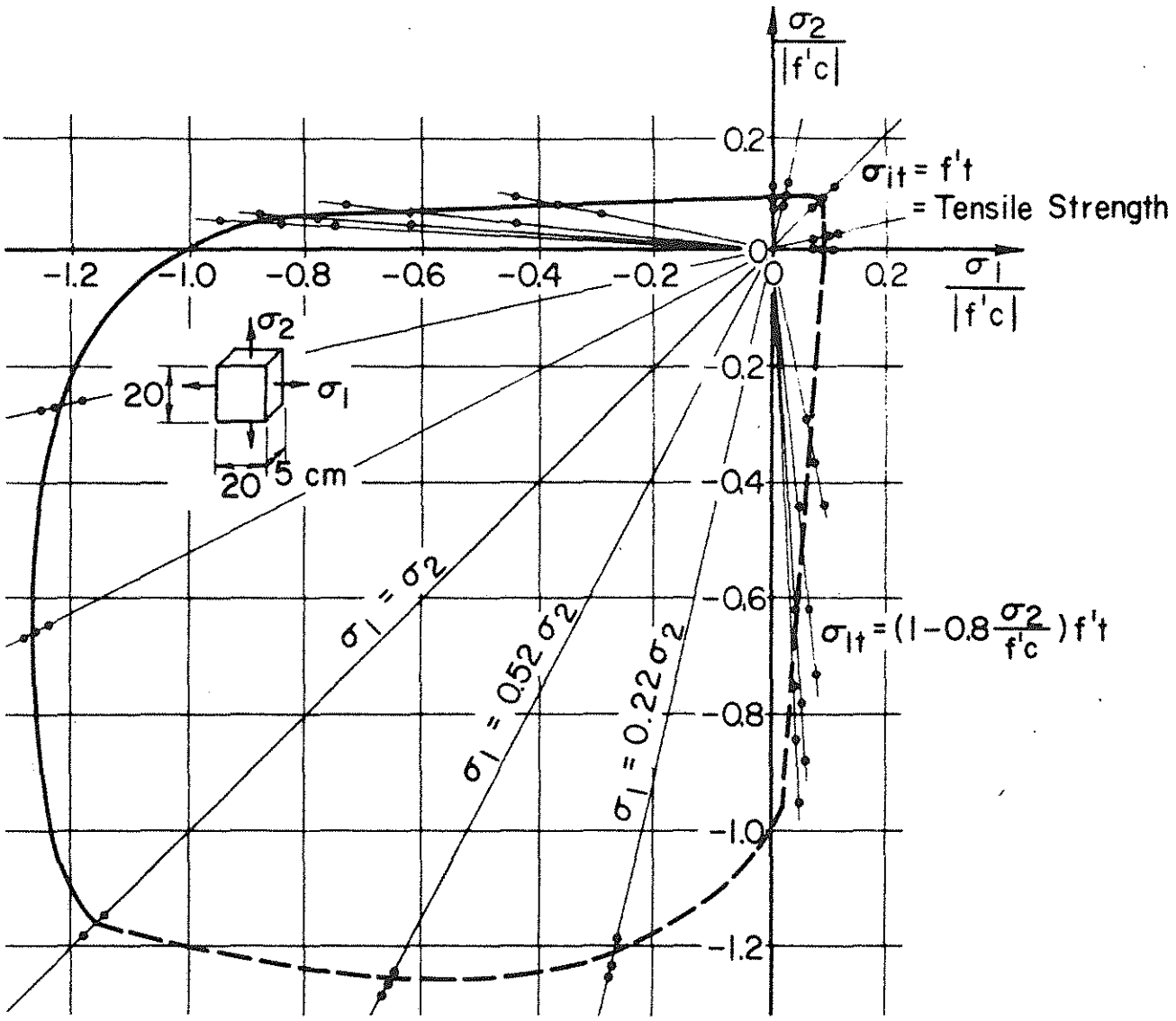

$$\left(\frac{\sigma_1}{f'c} + \frac{\sigma_2}{f'c}\right)^2 - \frac{\sigma_2}{f'c} - 3.65\frac{\sigma_1}{f'c} = 0$$

$$\text{or} \qquad \sigma_{2c} = \frac{1 + 3.65\alpha}{(1+\alpha)^2} f'c \qquad \alpha = \frac{\sigma_1}{\sigma_2}$$

Figure 2.14a Analytical Biaxial Strength Envelope (19)
(Used for Material Simulation)

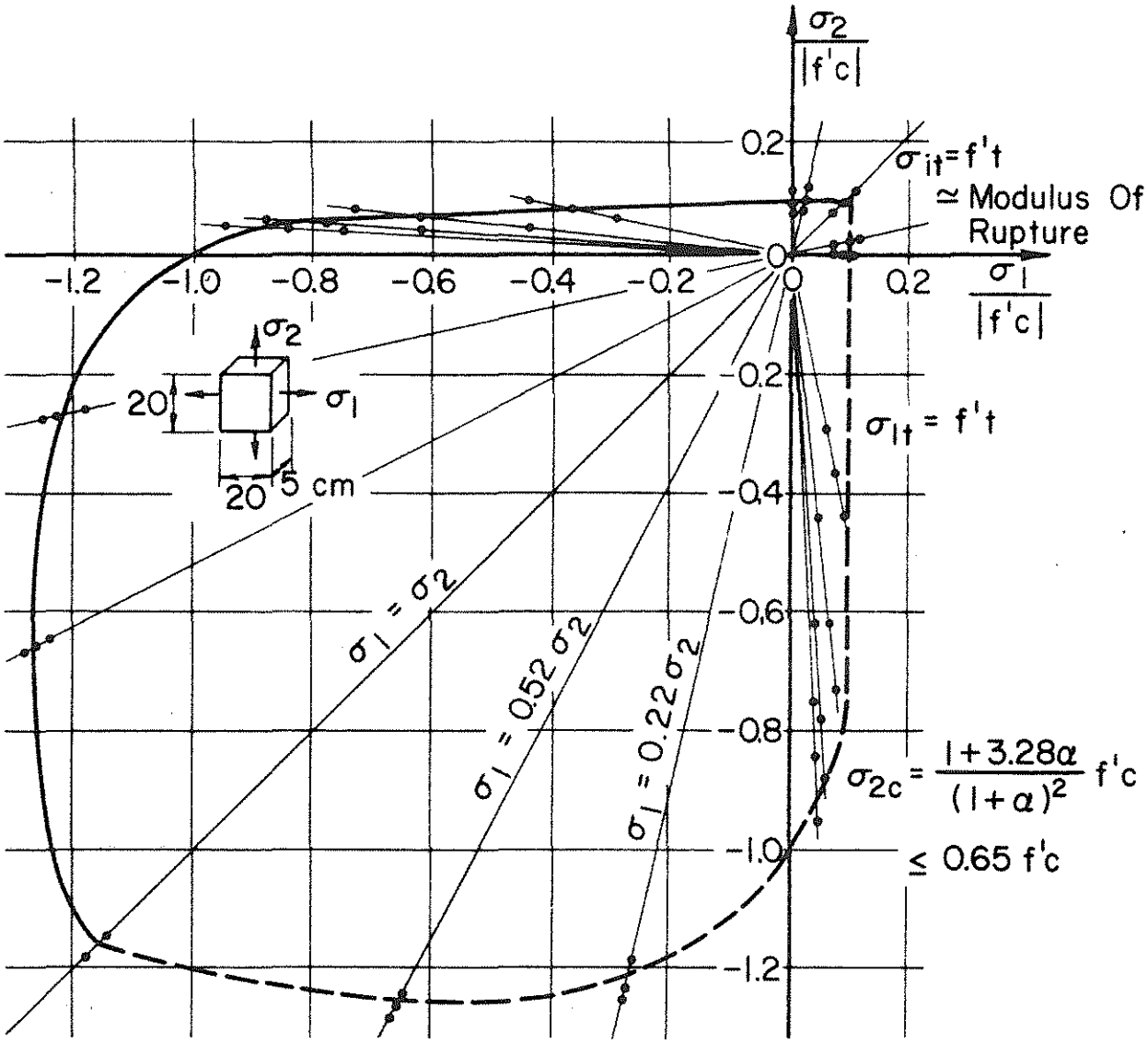

$$\sigma_{2c} = \frac{1+3.65\alpha}{(1+\alpha)^2} f'c \qquad \alpha = \frac{\sigma_1}{\sigma_2}$$

$$\sigma_{1c} = \alpha\, \sigma_{2c}$$

Figure 2.14b Analytical Biaxial Strength Envelope for Proposed Model

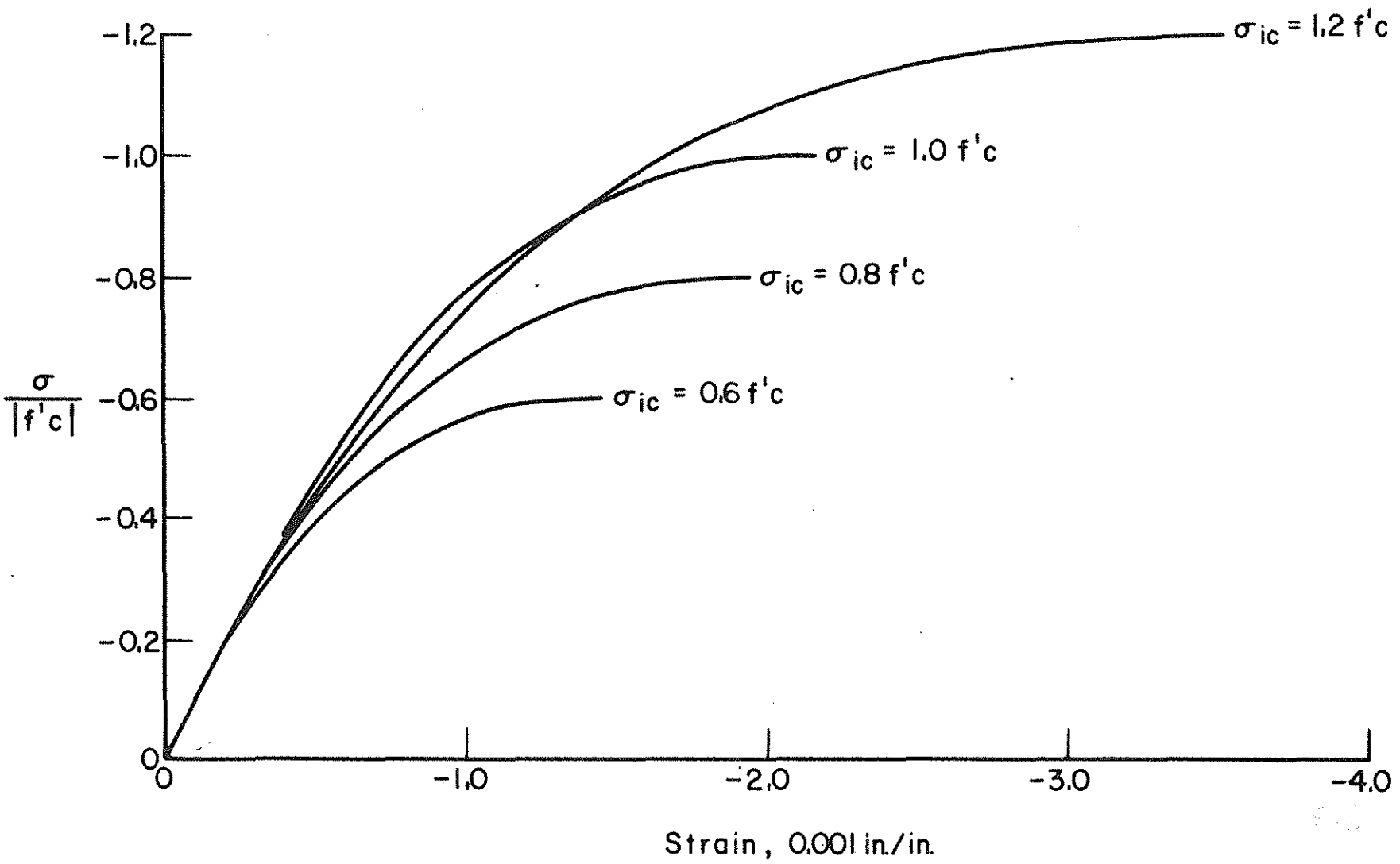

Figure 2.15 Equivalent Uniaxial Curves for Compression

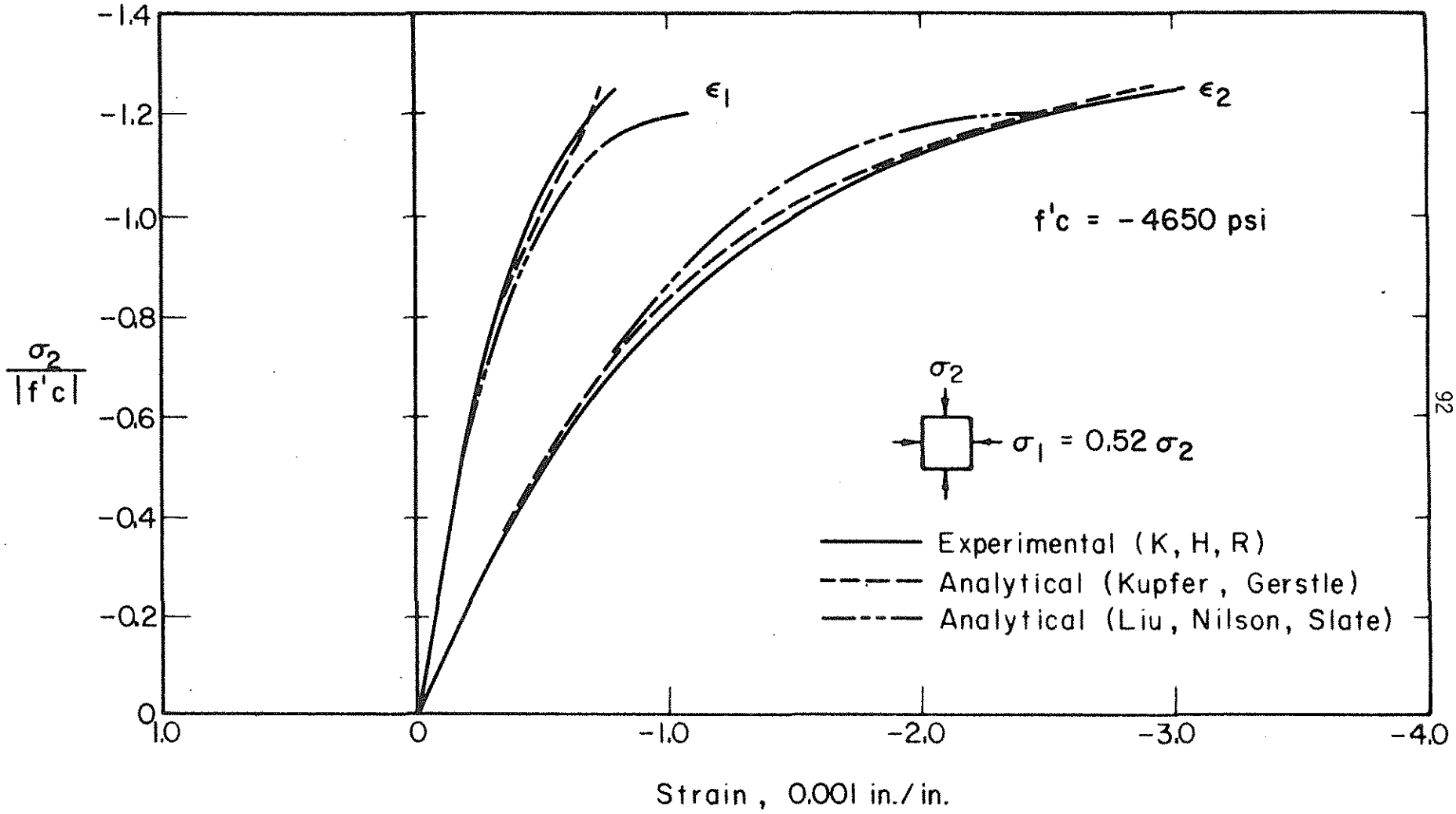

Figure 2.16 Comparison of Analytical Models (19,23) with Biaxial Compression Test, $\alpha = 0.52$ (20)

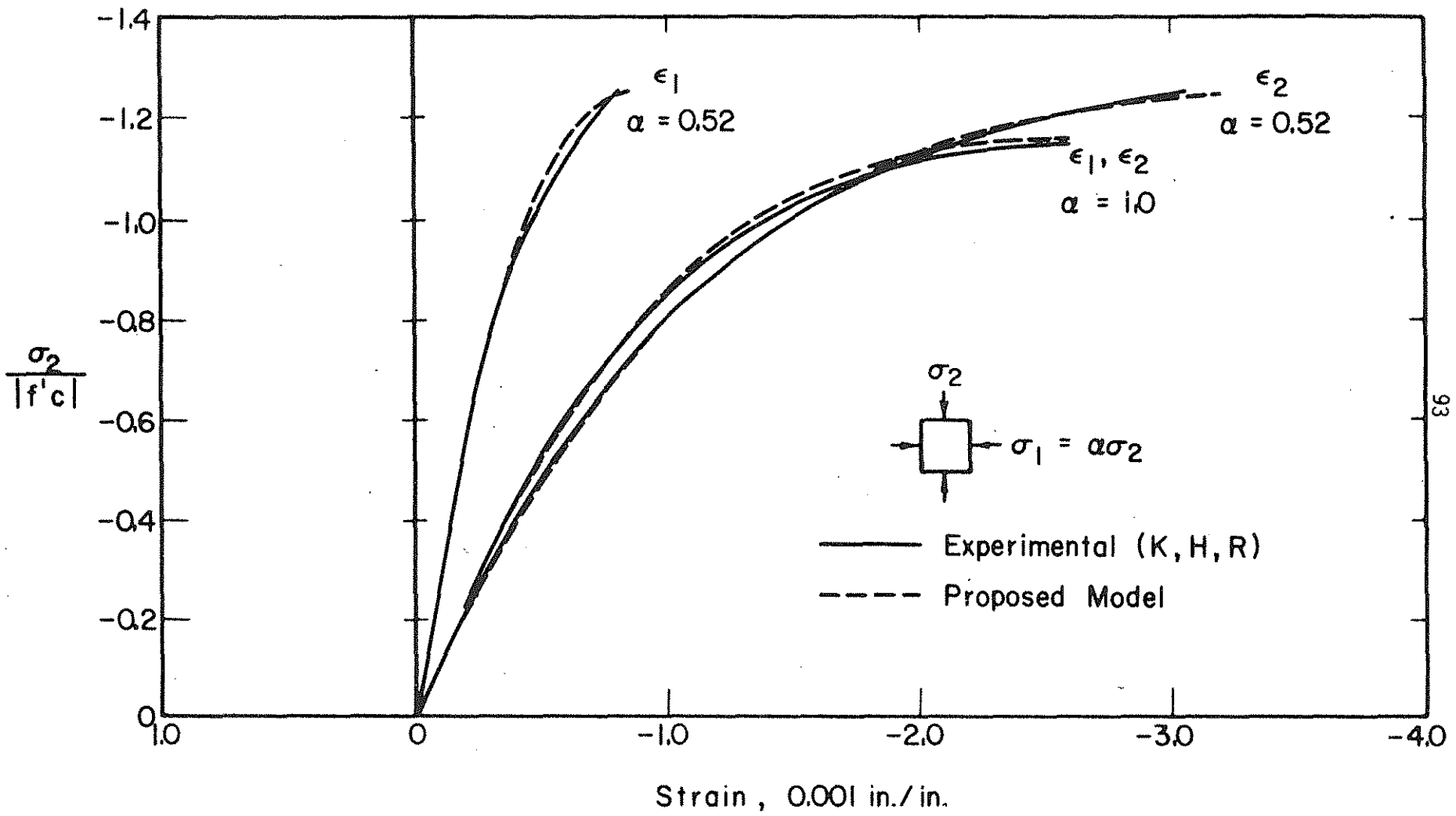

Figure 2.17 Comparison of the Proposed Model with Biaxial Compression Tests (20)

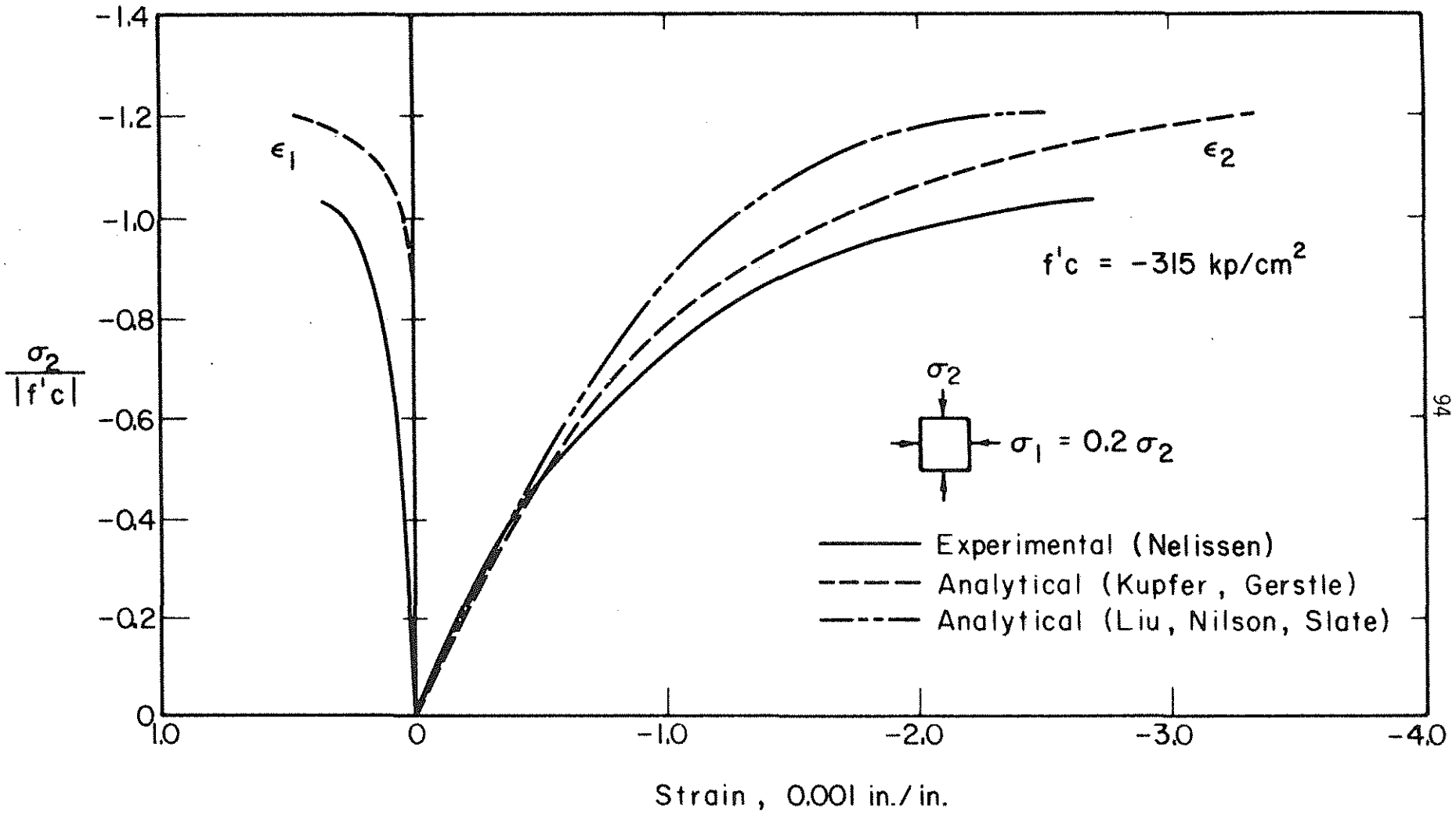

Figure 2.18 Comparison of Analytical Models (19,23) with Biaxial Compression Test, $\alpha = 0.2$ (26)

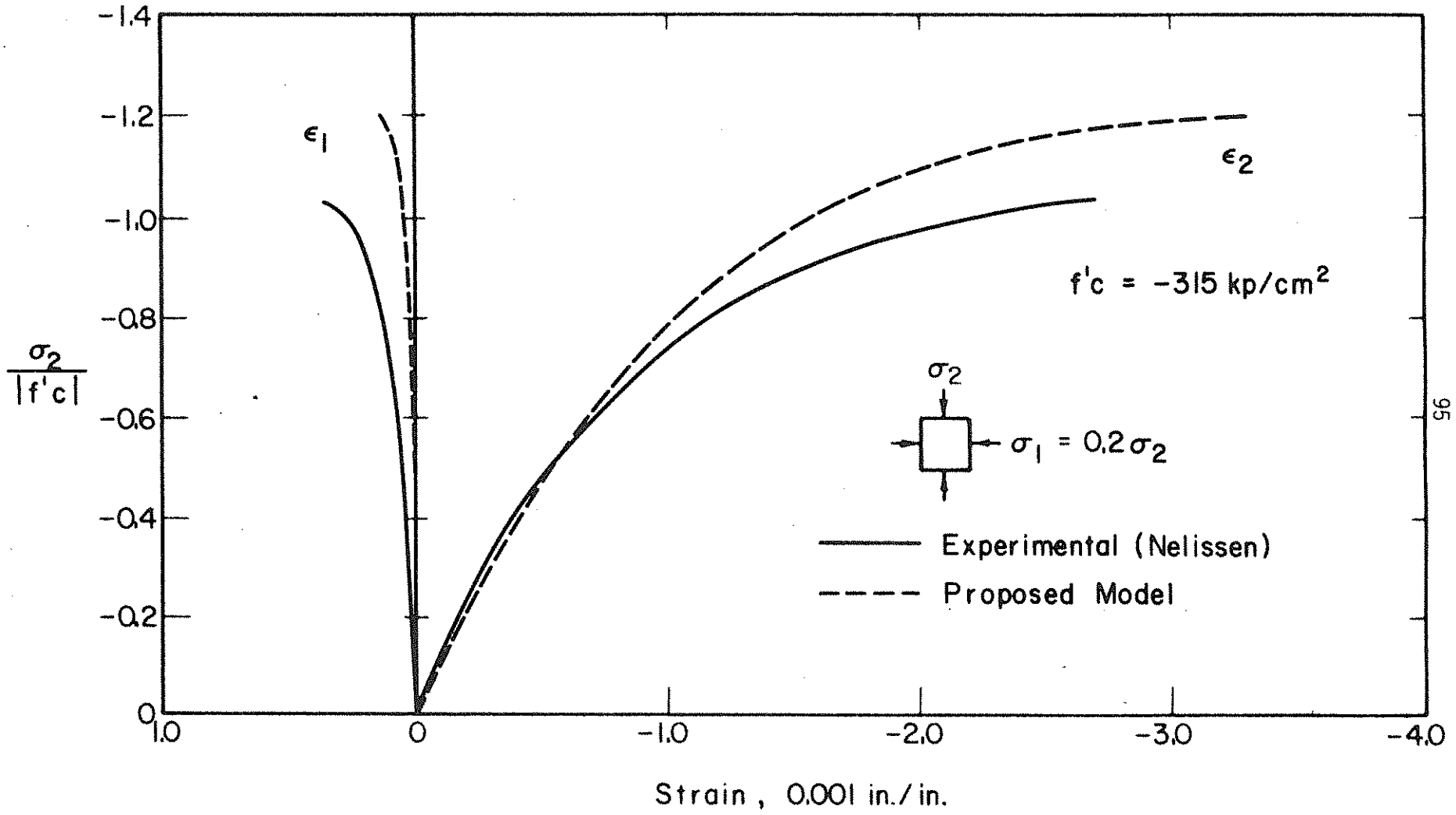

Figure 2.19 Comparison of the Proposed Model with Biaxial Compression Test, $\alpha = 0.2$ (26)

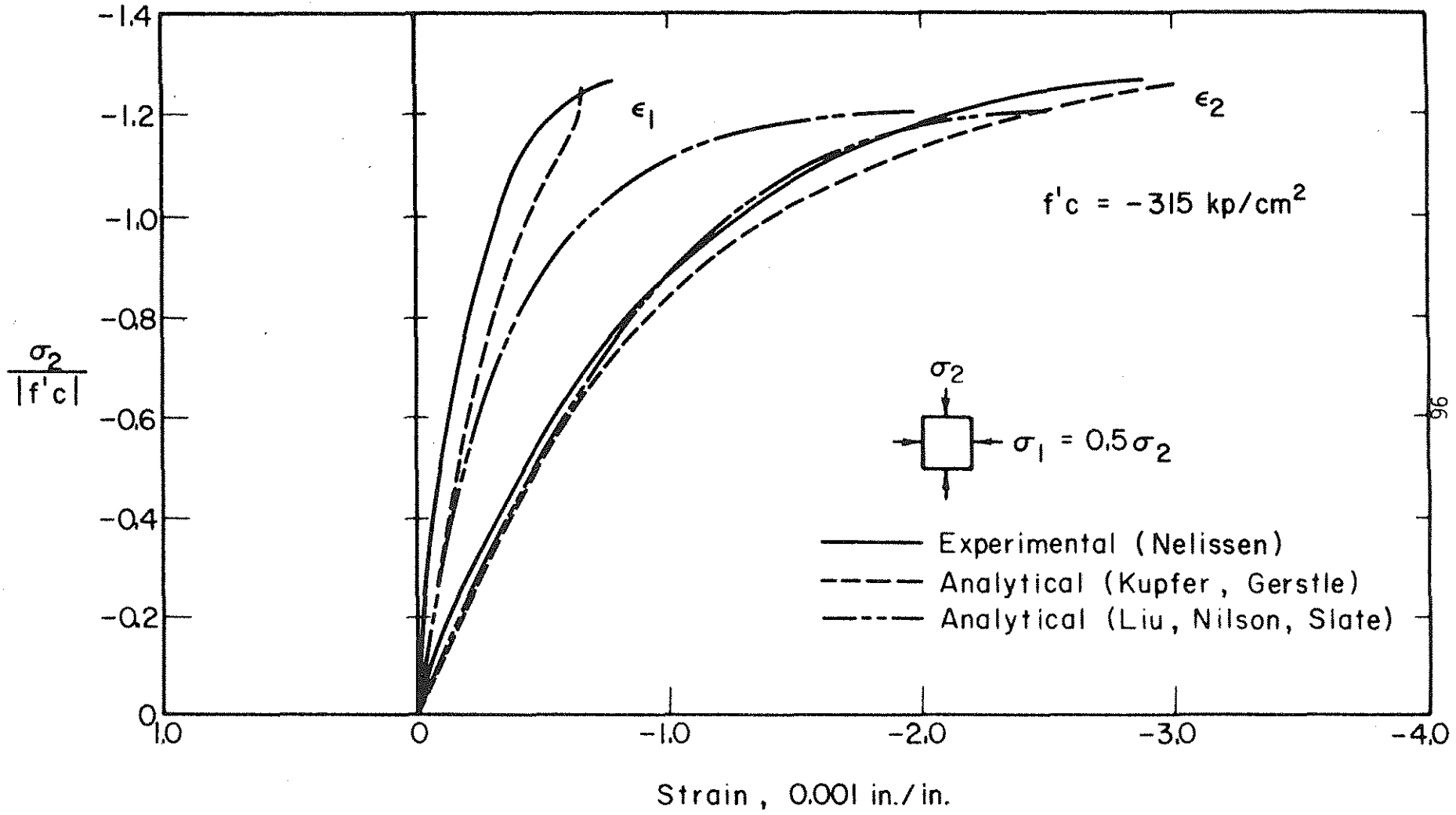

Figure 2.20 Comparison of Analytical Models (19,23) with Biaxial Compression Test, $\alpha = 0.5$ (26)

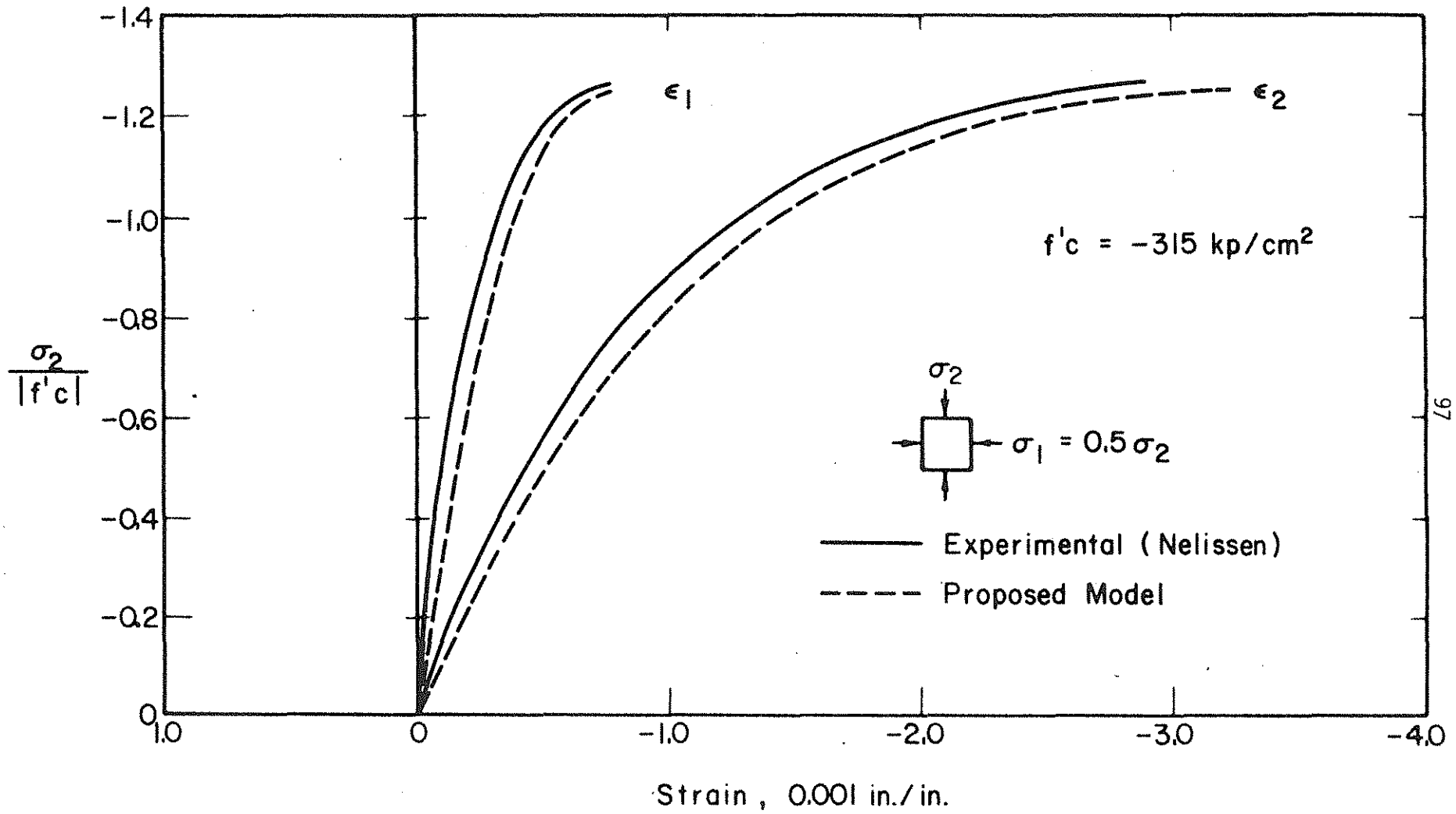

Figure 2.21 Comparison of the Proposed Model with Biaxial Compression Test, $\alpha = 0.5$ (26)

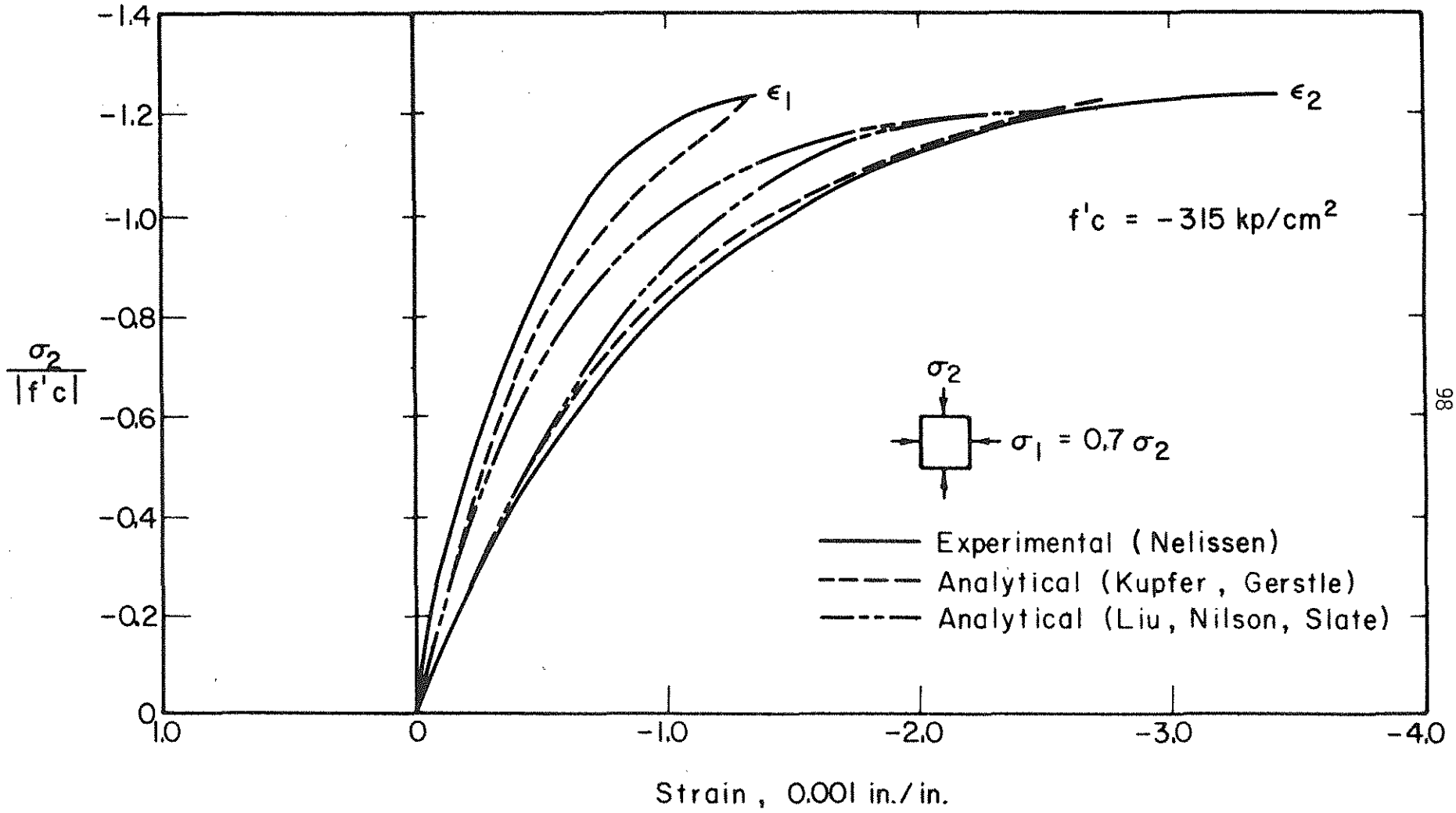

Figure 2.22 Comparison of Analytical Models (19,23) with Biaxial Compression Test, $\alpha = 0.7$ (26)

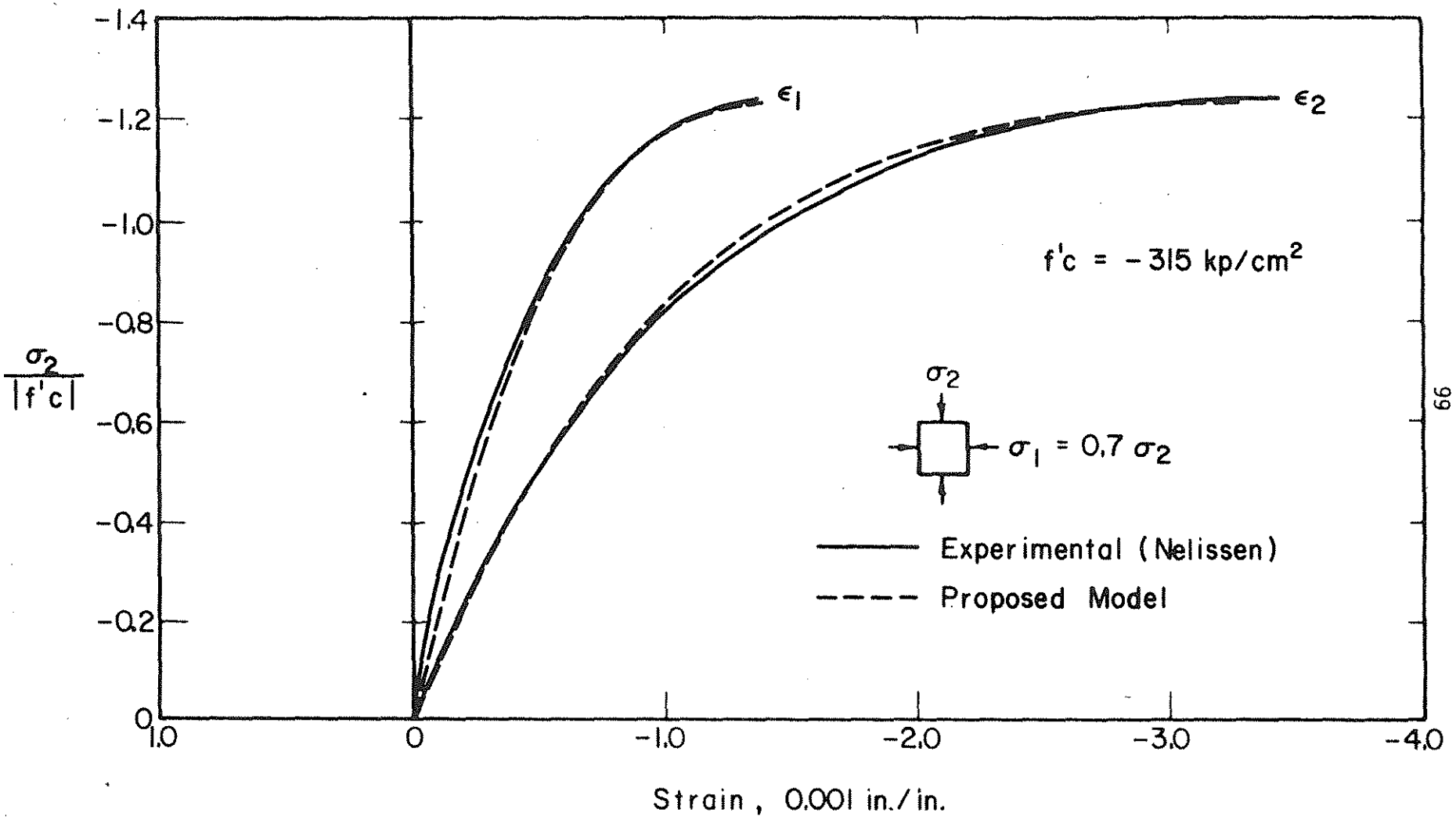

Figure 2.23 Comparison of the Proposed Model with Biaxial Compression Test, $\alpha = 0.7$ (26)

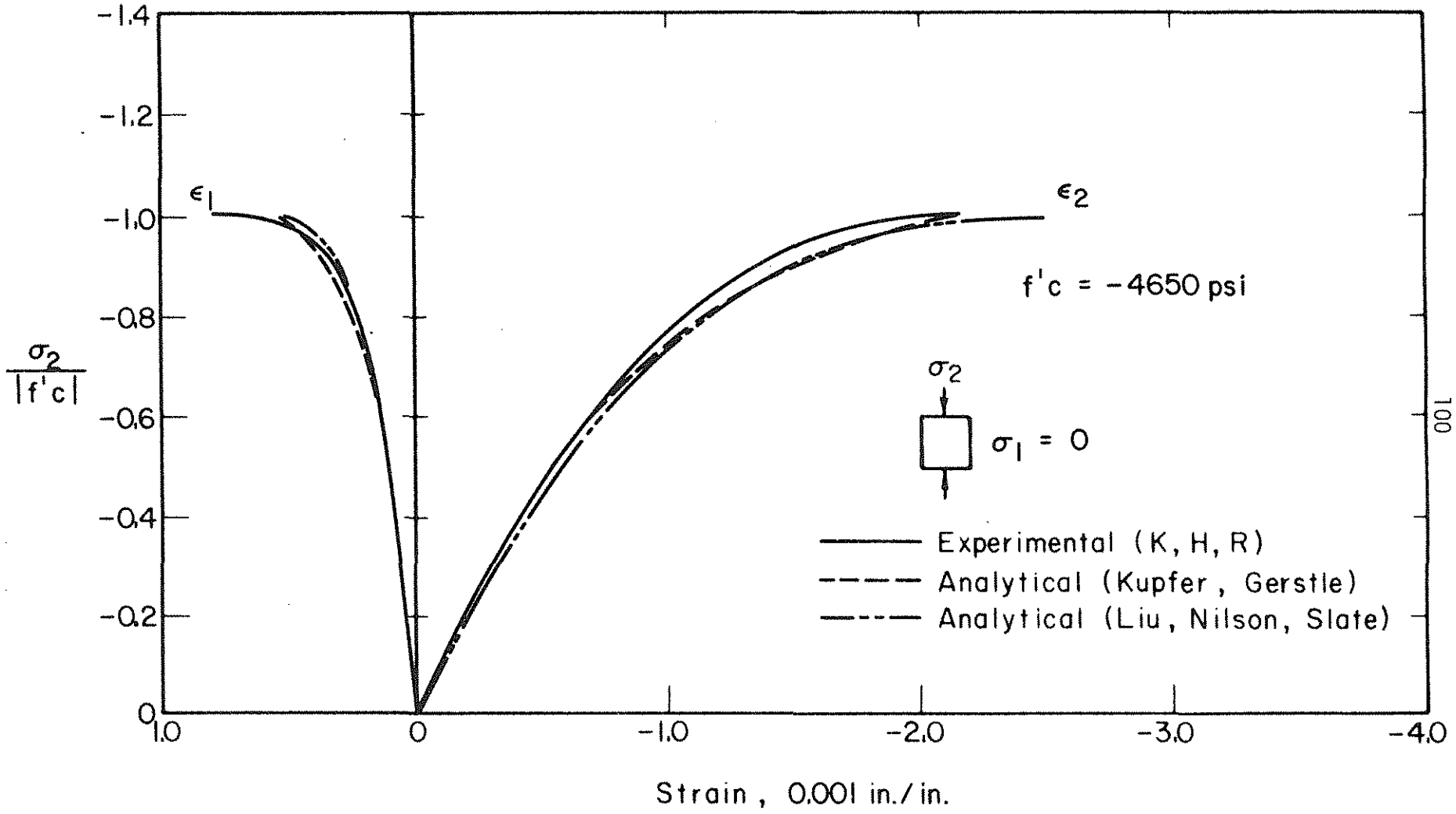

Figure 2.24 Comparison of Analytical Models (19,23) with Uniaxial Compression Test (20)

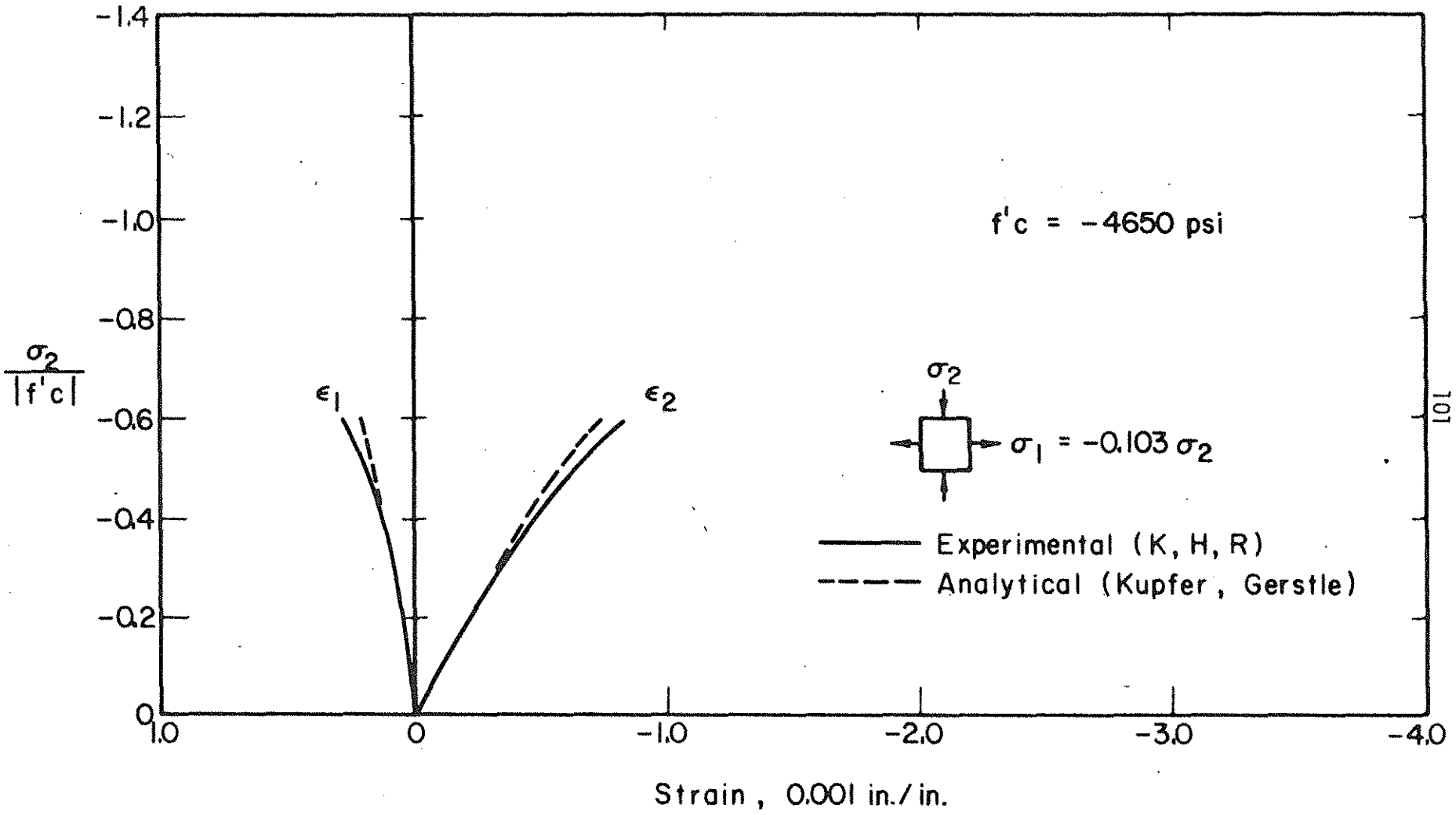

Figure 2.25 Comparison of Analytical Model (19) with Tension-Compression Test, α = -0.103 (20)

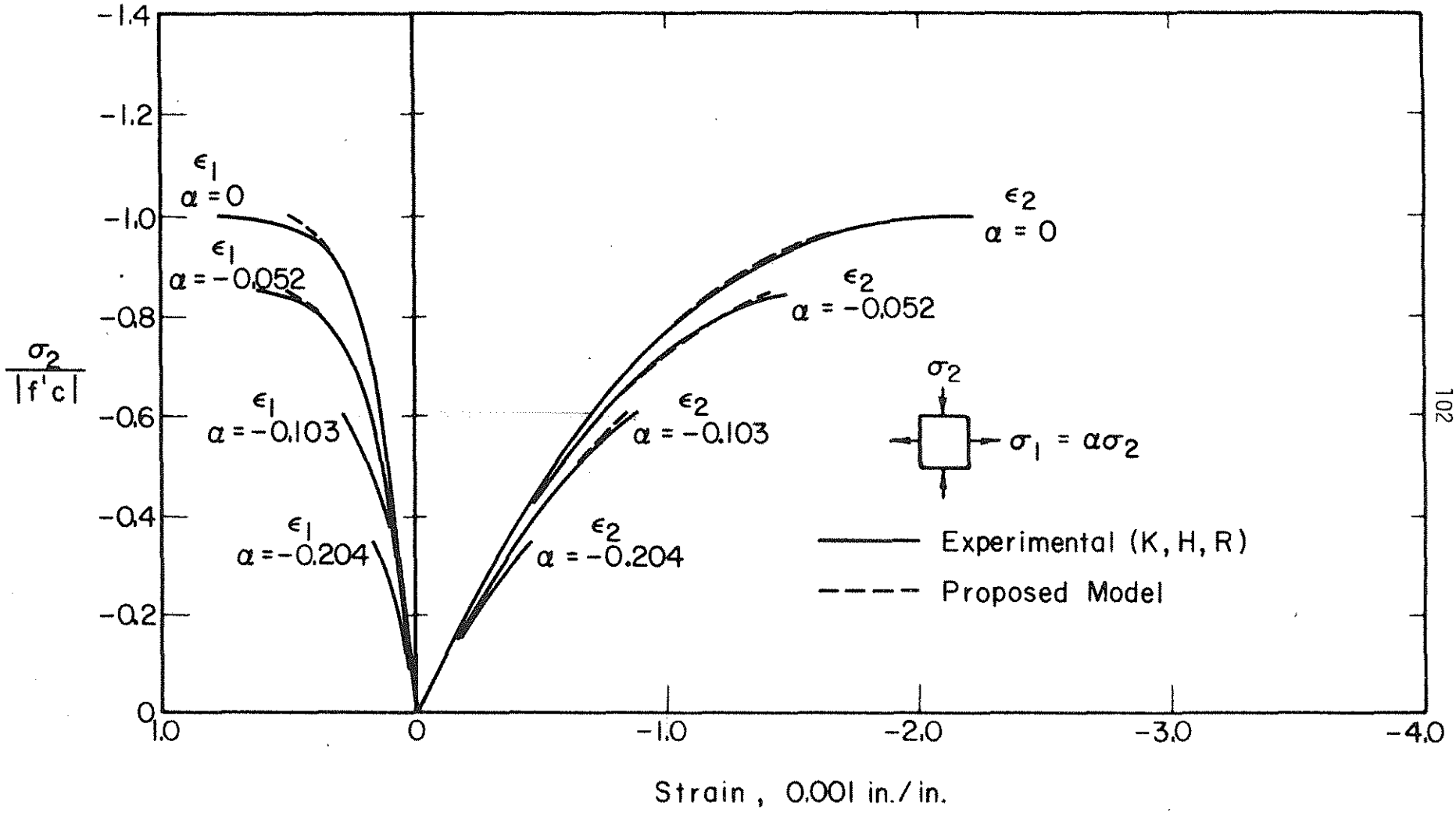

Figure 2.26 Comparison of the Proposed Model with Tension-Compression and Uniaxial Compression Tests (20)

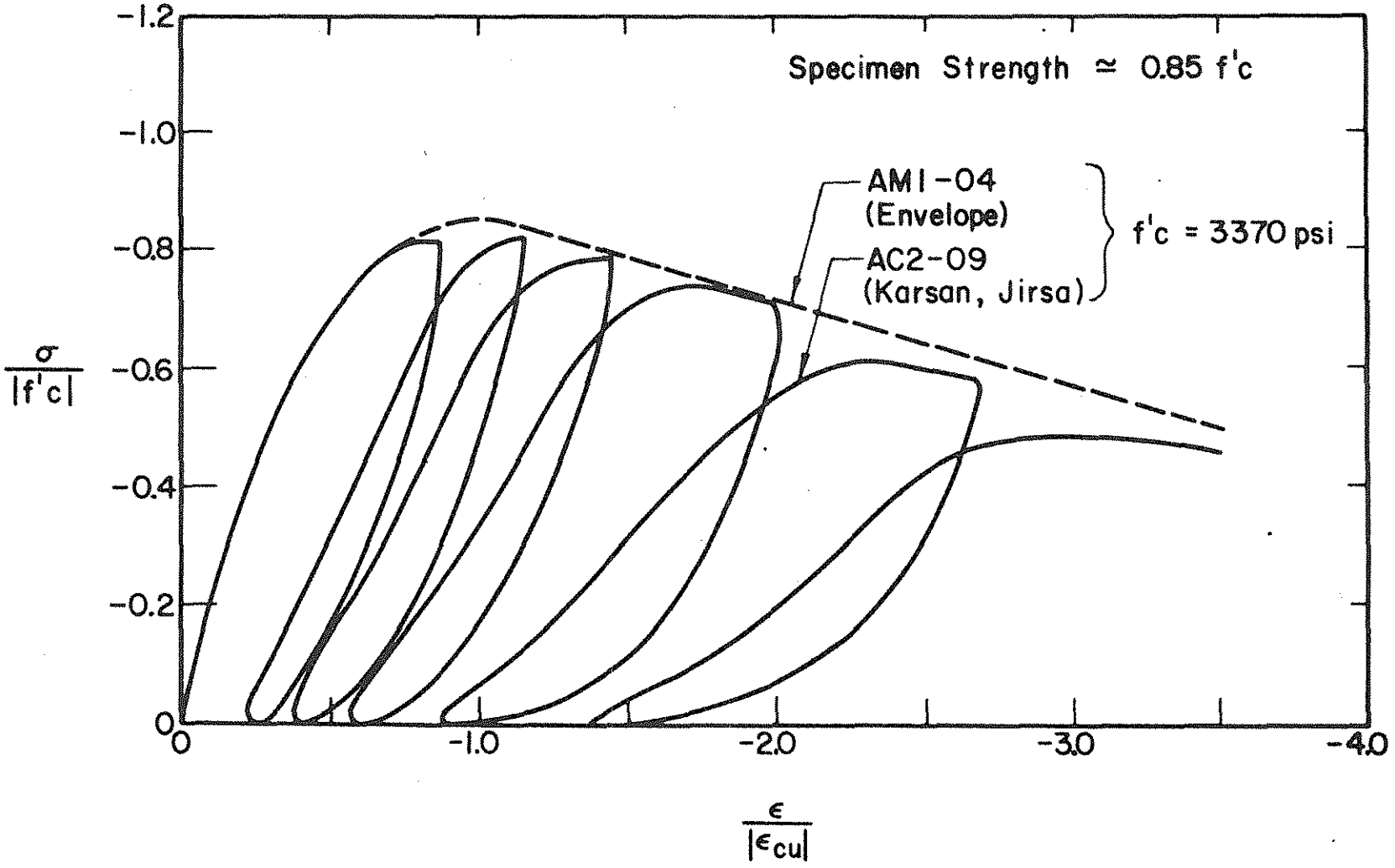

Figure 2.27 Behavior of Concrete Under Cyclic Load, Comparison with Envelope Curve (16,17)

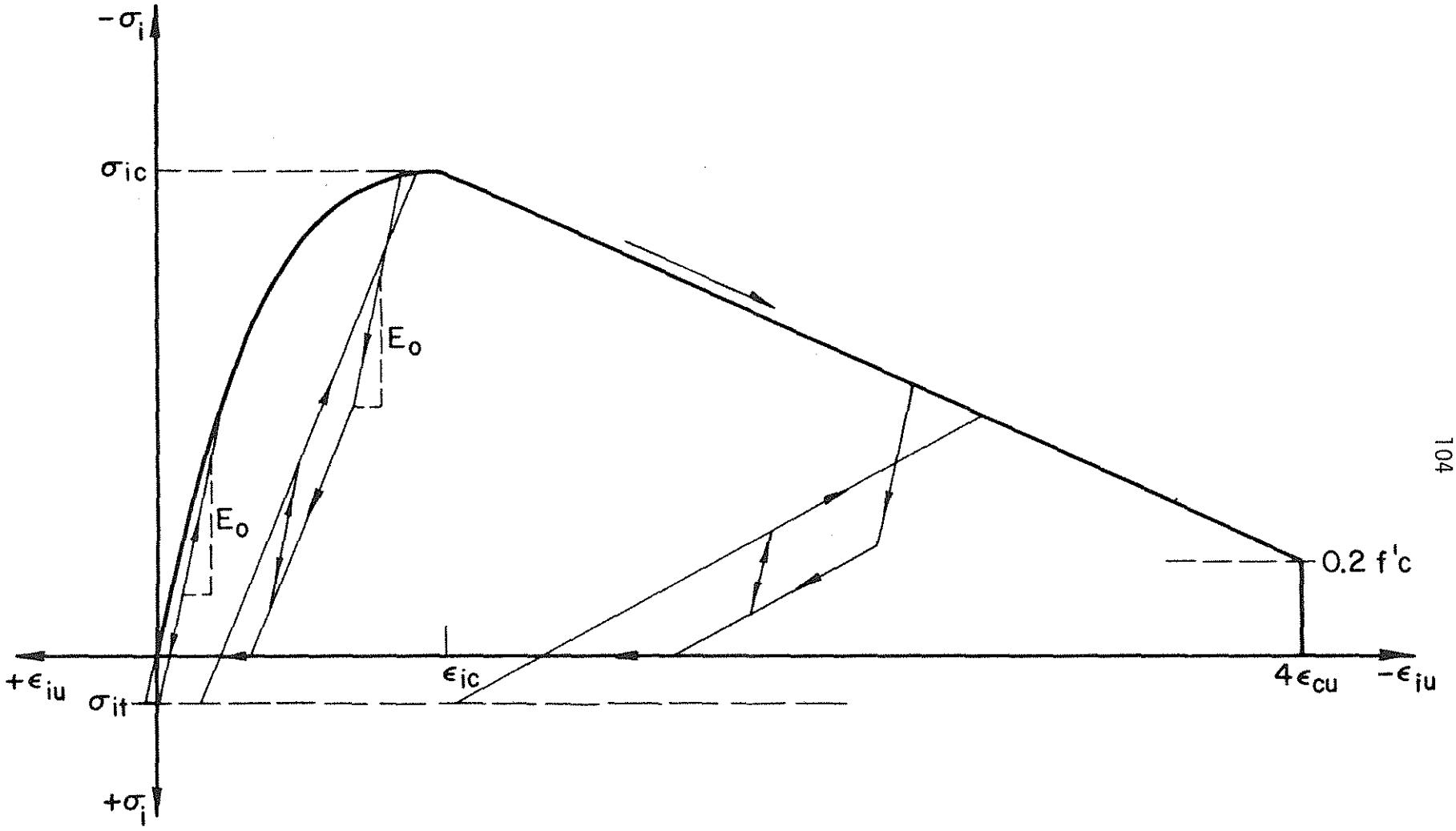

Figure 2.28 Proposed Model Under Cyclic Load

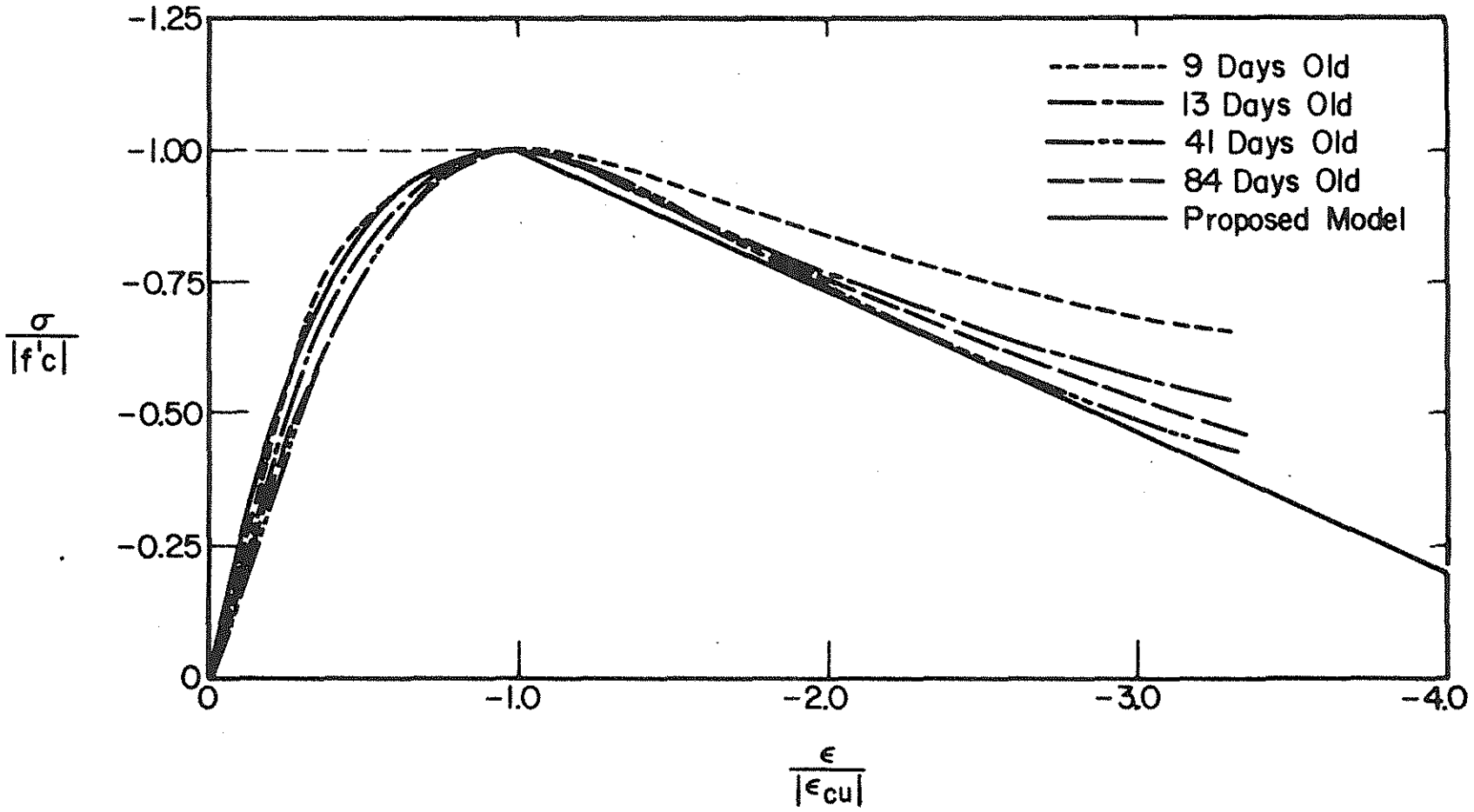

Figure 2.29 Comparison of Envelope Curve for Proposed Model to Experimental Curves (39)

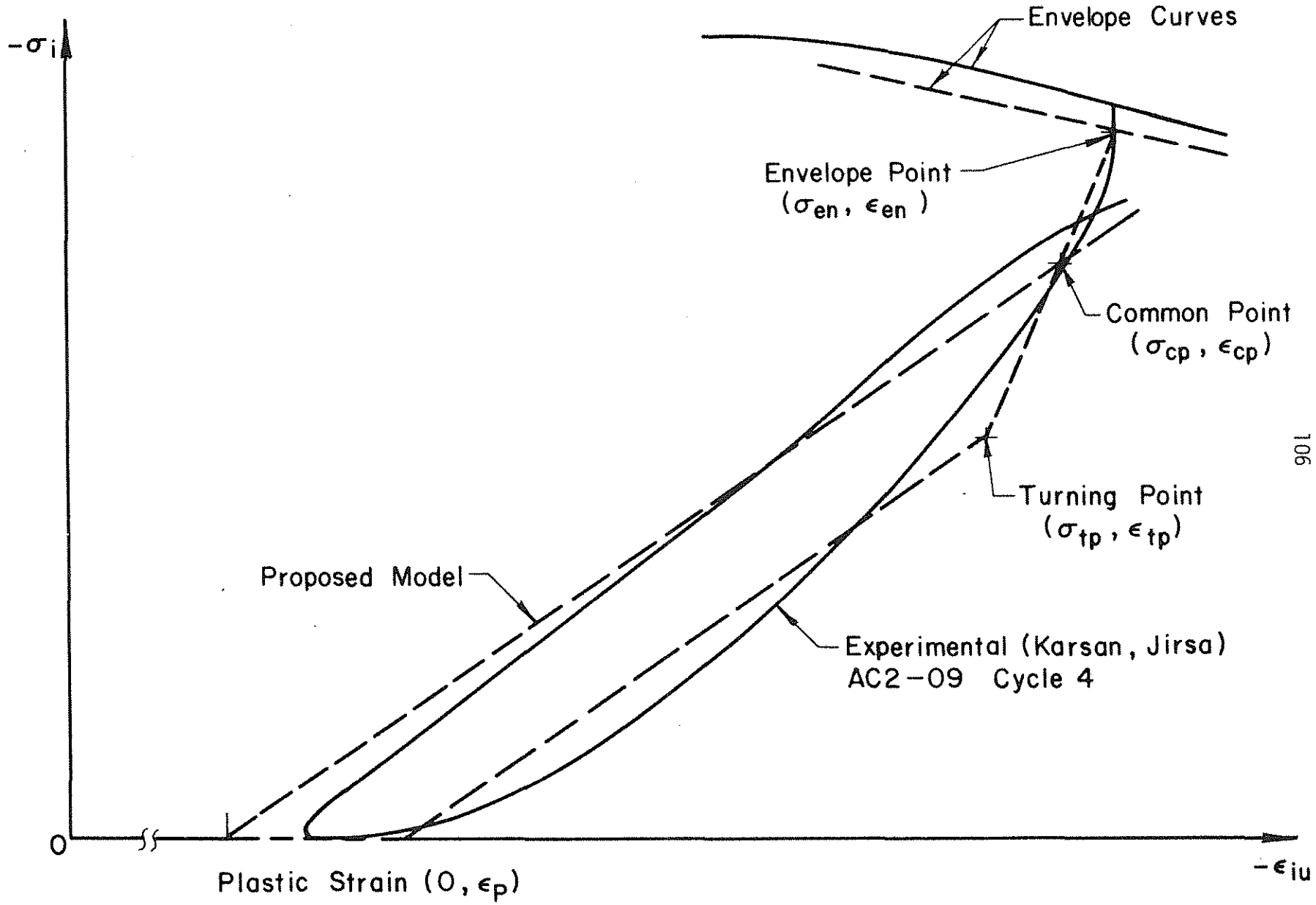

Figure 2.30 Typical Hysteresis Curves

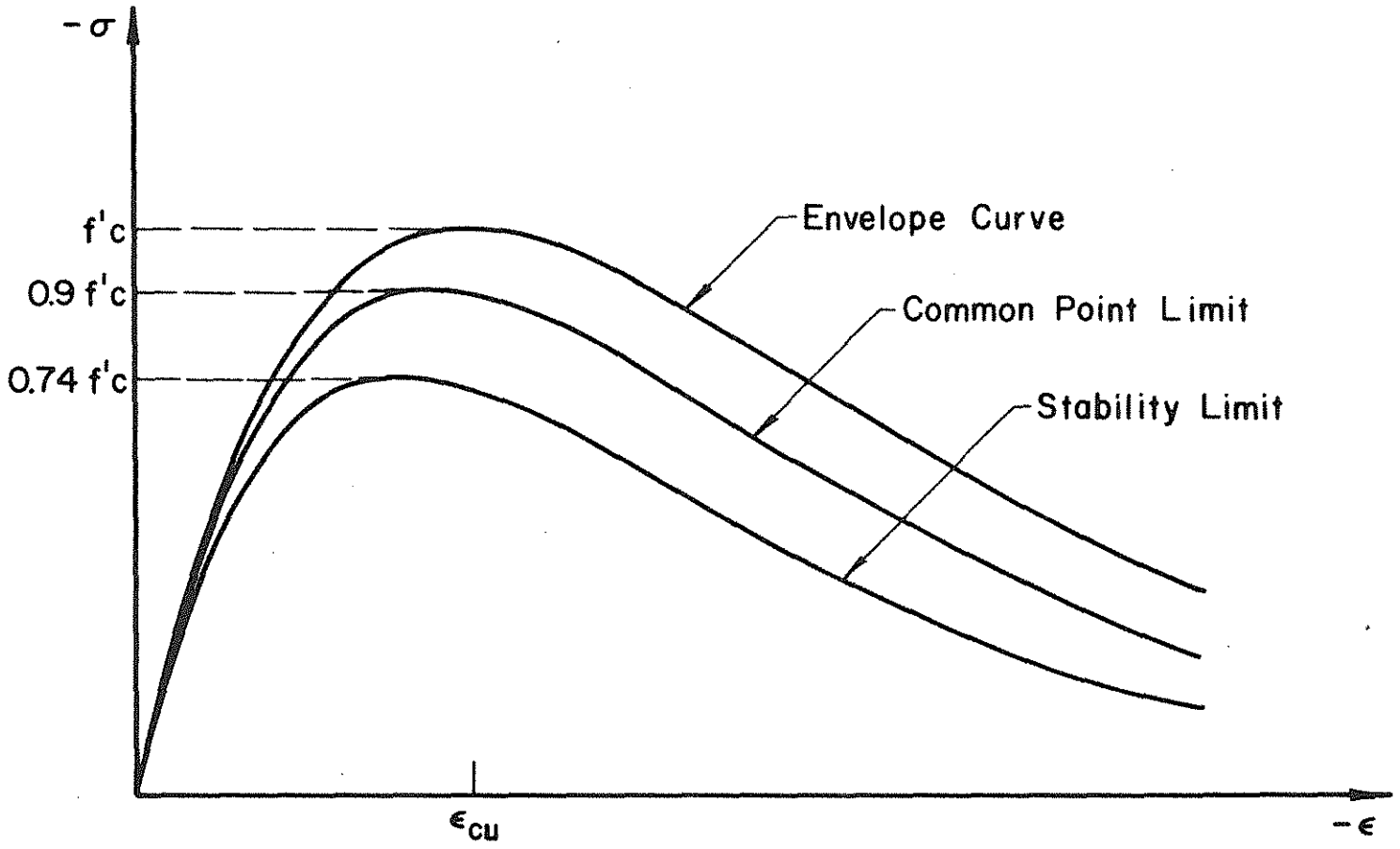

Figure 2.31 Common Point Limit and Stability Limit (17)

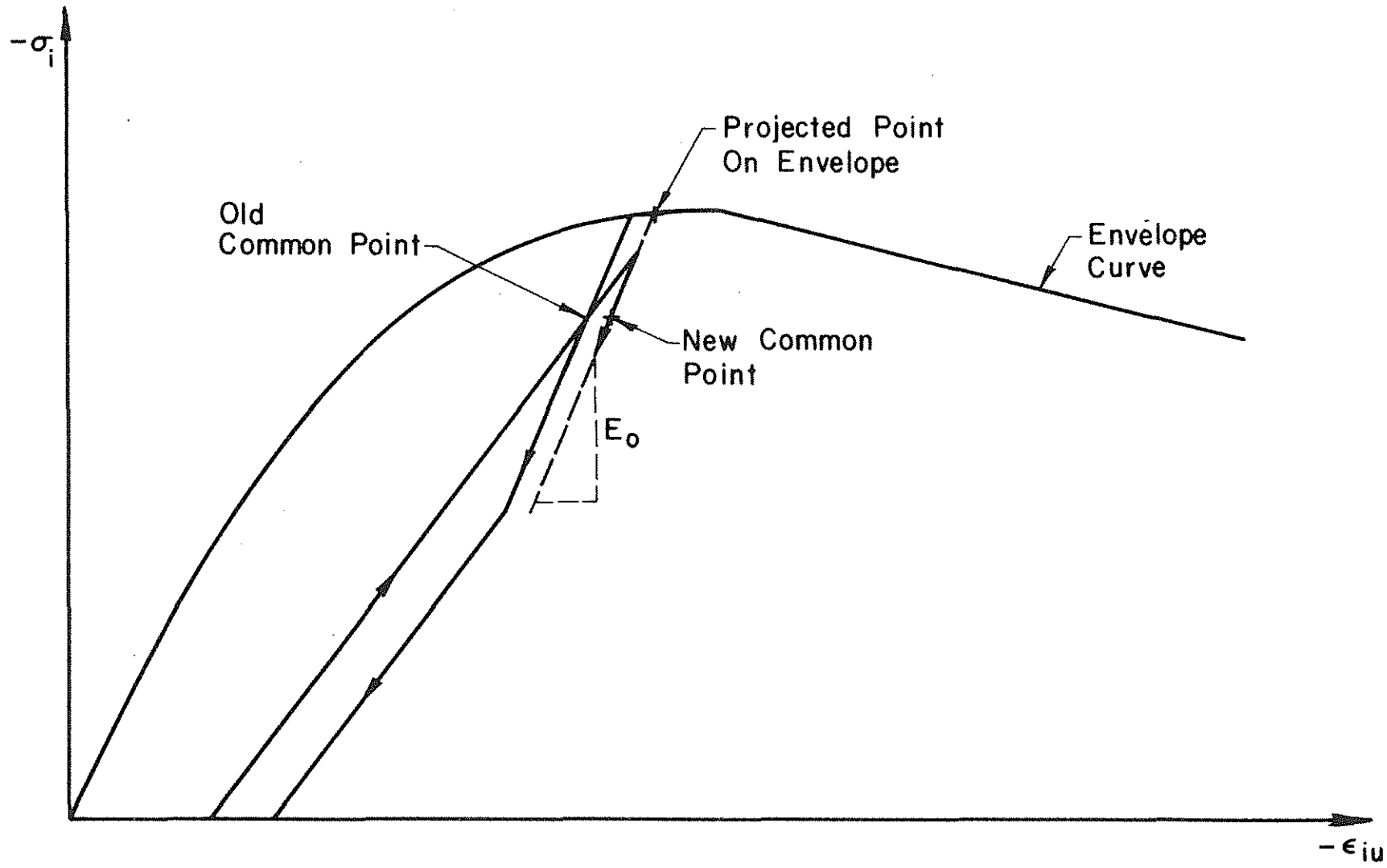

Figure 2.32 Strain Reversal Between Common Point and Envelope Curve

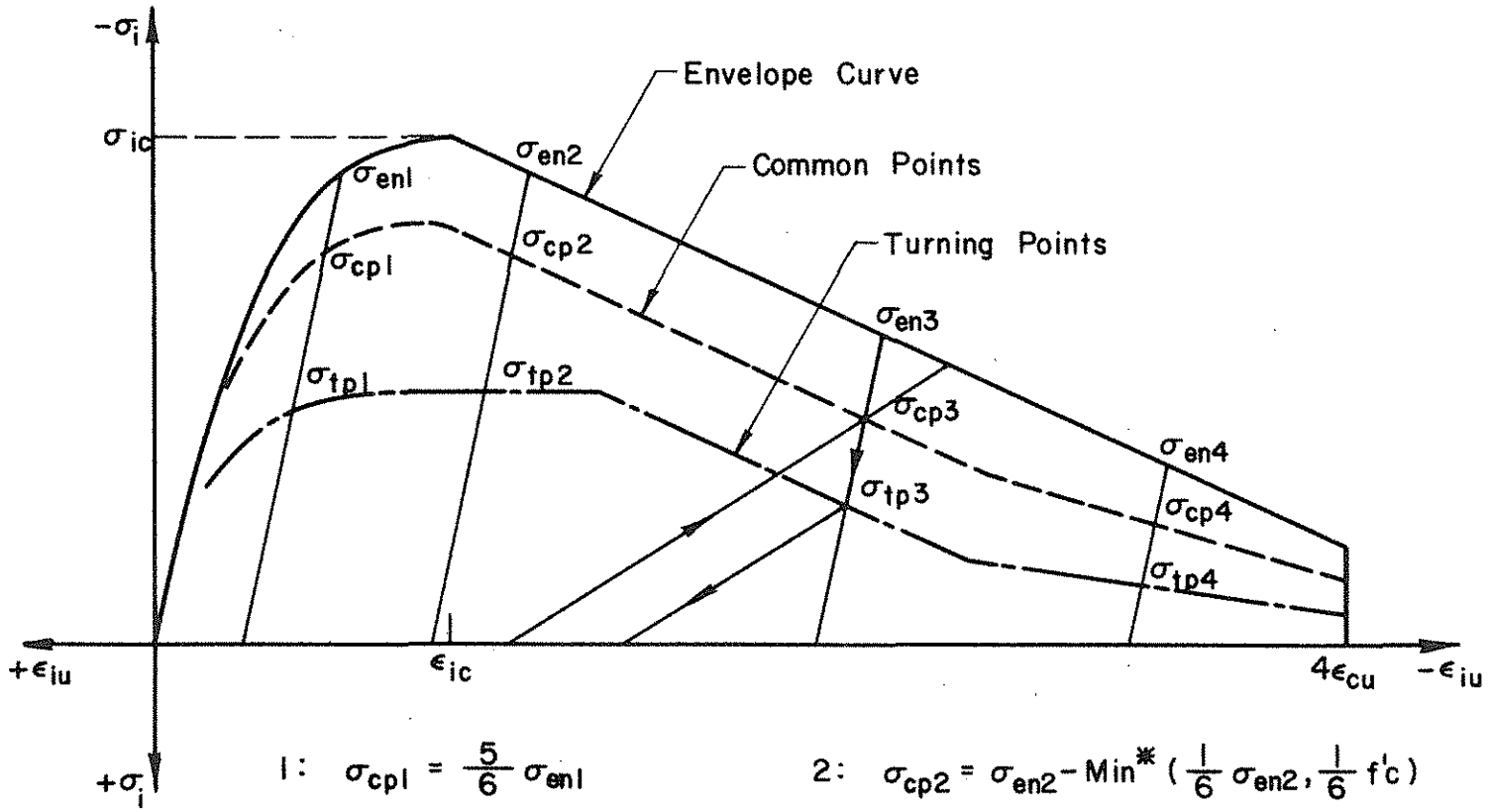

1: $\sigma_{cp1} = \frac{5}{6}\sigma_{en1}$

$\sigma_{tp1} = \frac{1}{2}\sigma_{en1}$

2: $\sigma_{cp2} = \sigma_{en2} - \text{Min}^{*}\left(\frac{1}{6}\sigma_{en2}, \frac{1}{6}f'c\right)$

$\sigma_{tp2} = \text{Min}^{*}\left(\frac{1}{2}\sigma_{en2}, \frac{1}{2}f'c\right)$

* Largest In Absolute Magnitude

3: $\sigma_{cp3} = \sigma_{en3} - \frac{1}{6}f'c$

$\sigma_{tp3} = \sigma_{en3} - 2(\sigma_{en3} - \sigma_{cp3})$

$= \sigma_{en3} - \frac{1}{3}f'c$

4: $\sigma_{cp4} = \frac{2}{3}\sigma_{en4}$

$\sigma_{tp4} = \frac{1}{3}\sigma_{en4}$

Figure 2.33 Envelope Curve, Common Points, and Turning Points

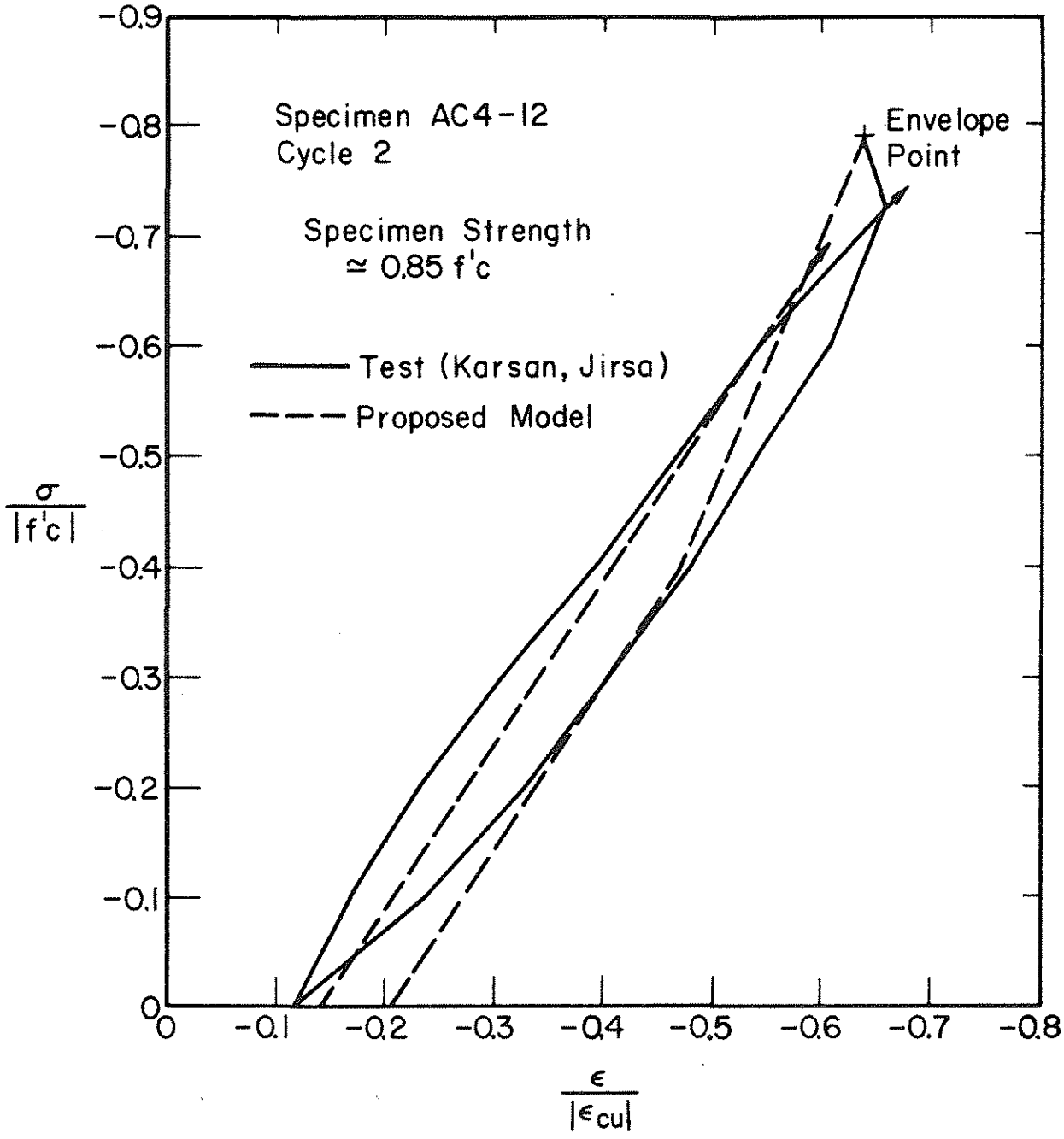

Figure 2.34 Comparison of Proposed Model with Experimental Hysteresis Curve #1 (16,17)

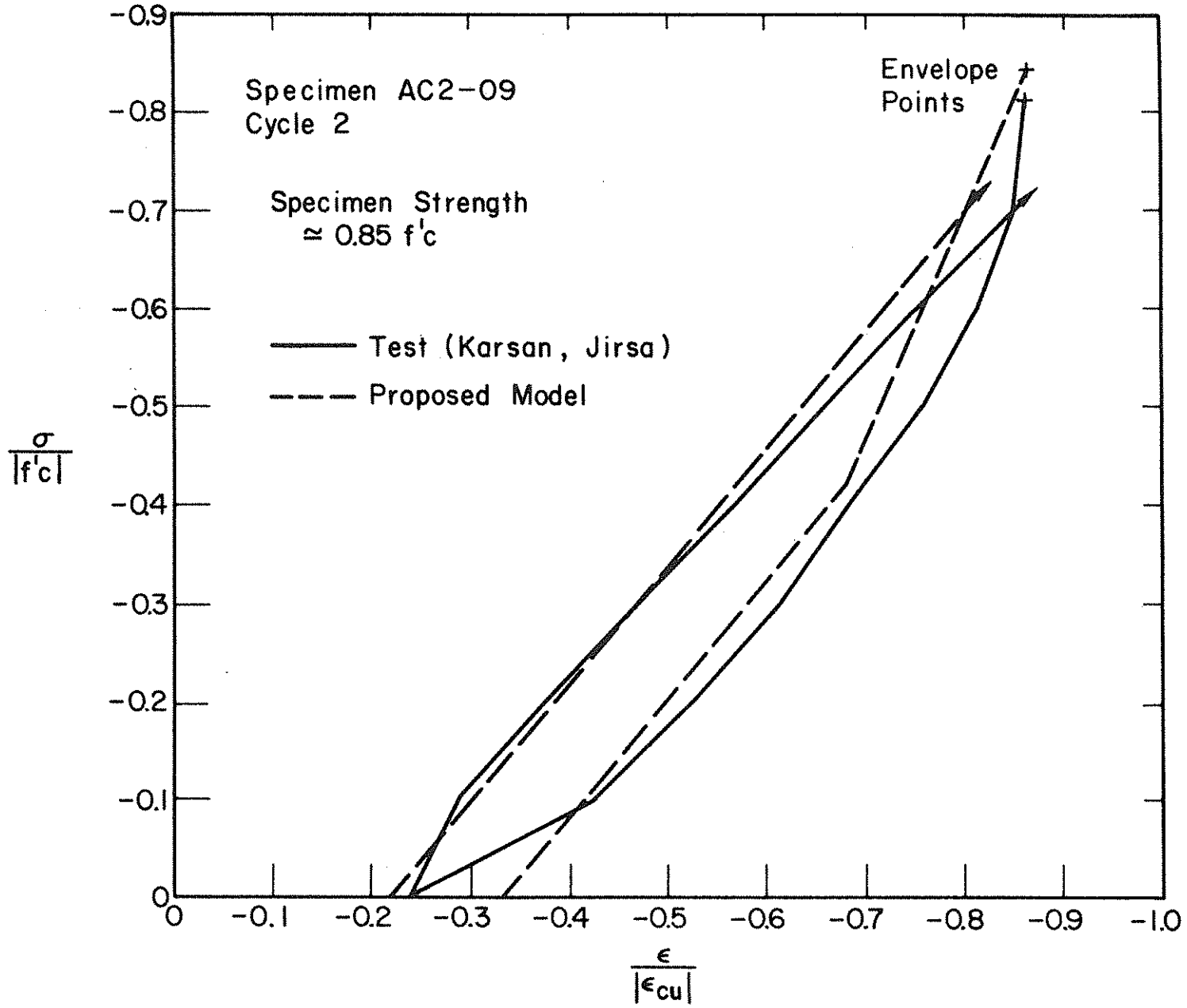

Figure 2.35 Comparison of Proposed Model with Experimental Hysteresis Curve #2 (16,17)

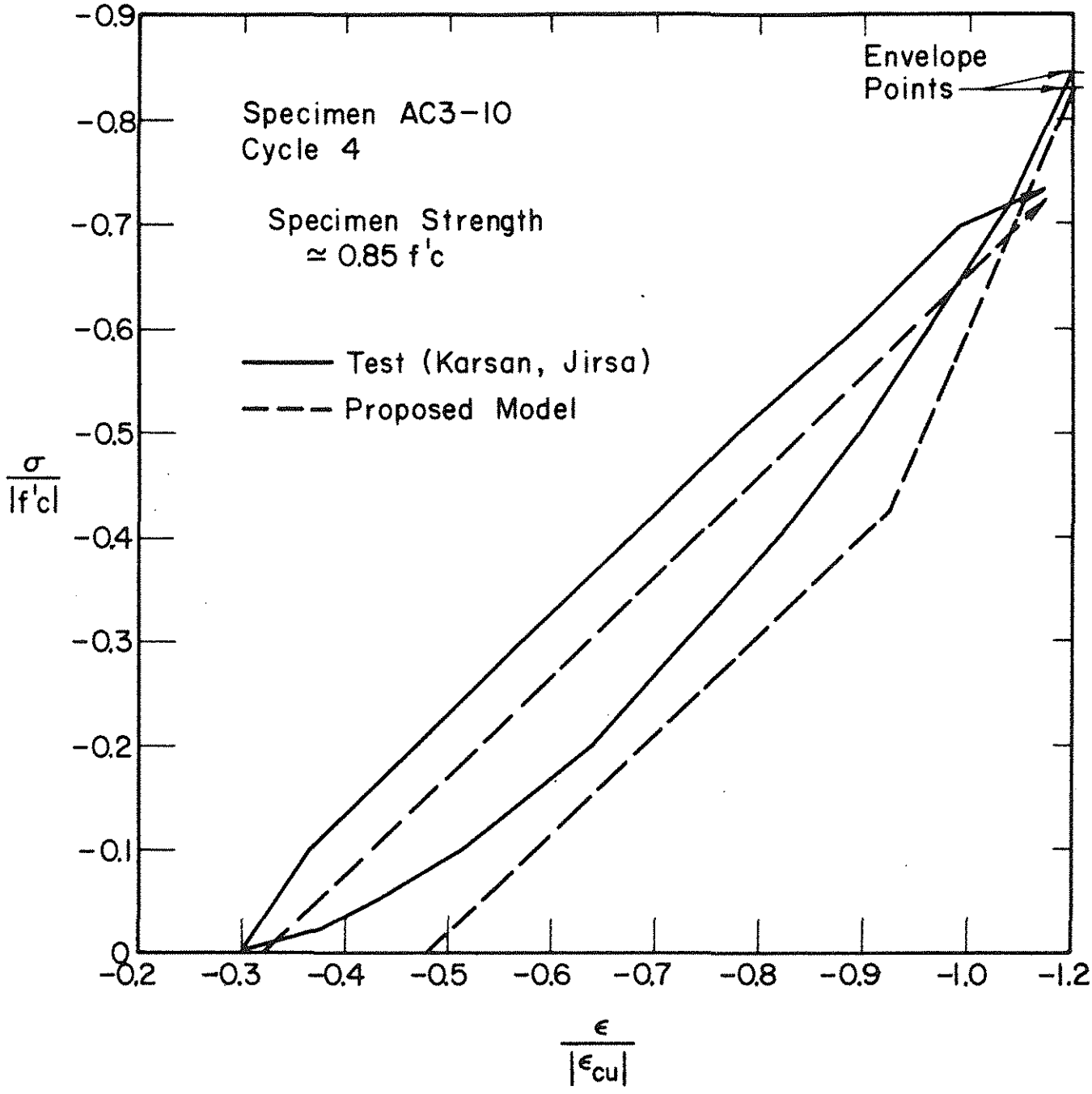

Figure 2.36 Comparison of Proposed Model with Experimental Hysteresis Curve #3 (16,17)

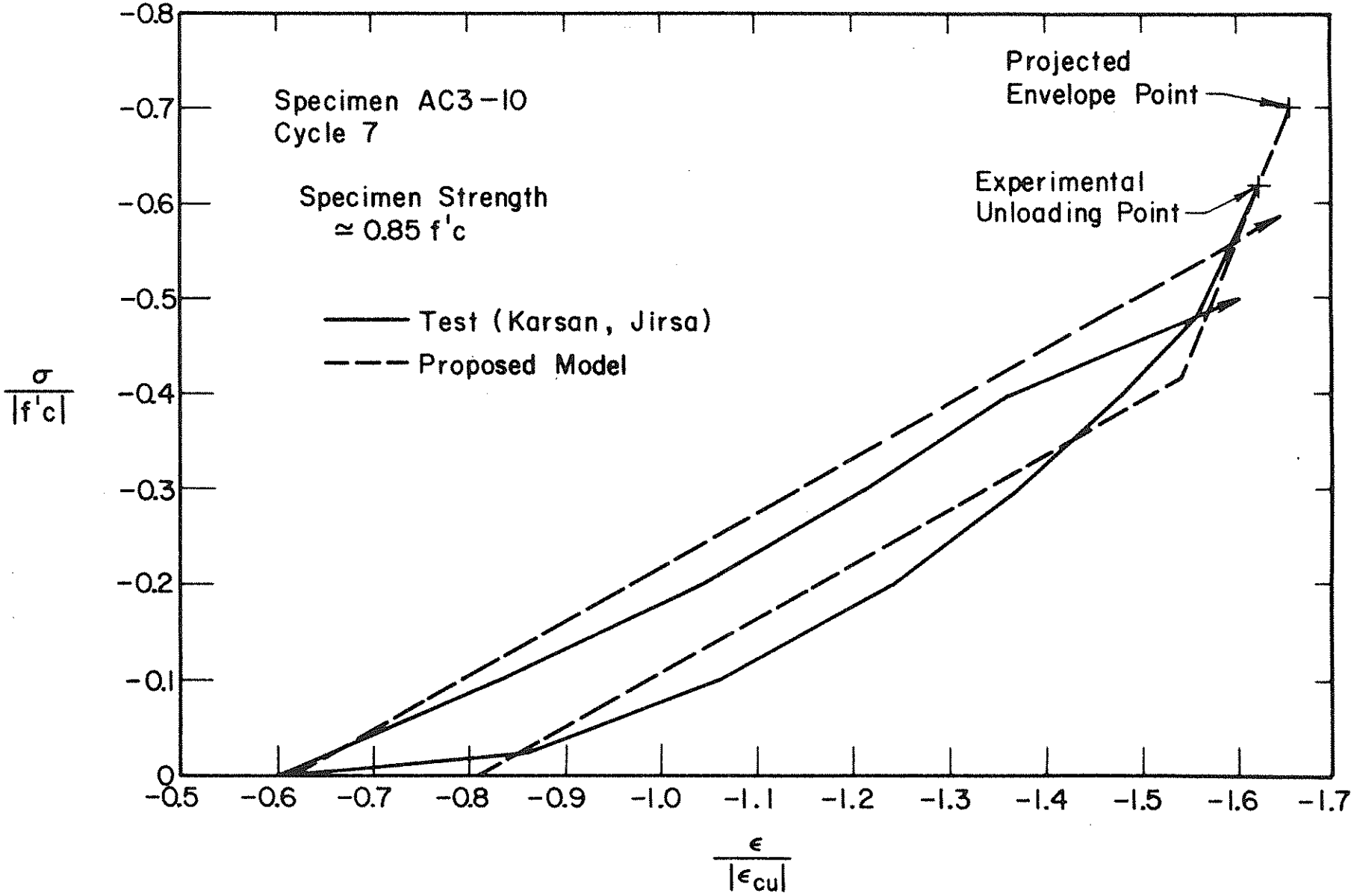

Figure 2.37 Comparison of Proposed Model with Experimental Hysteresis Curve #4 (16,17)

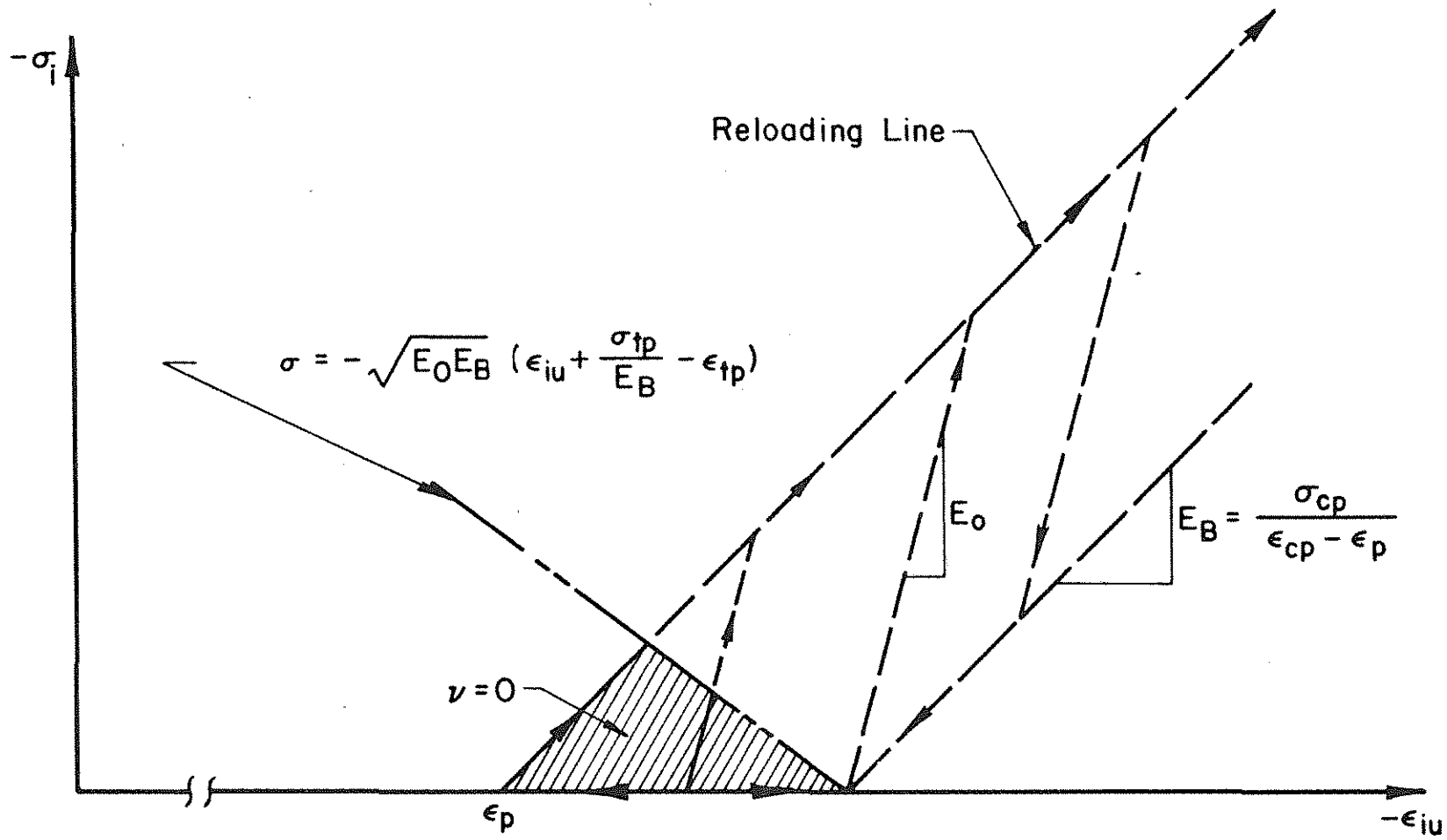

Figure 2.38 Region of Zero Poisson's Ratio to Prevent "Jacking Effect"

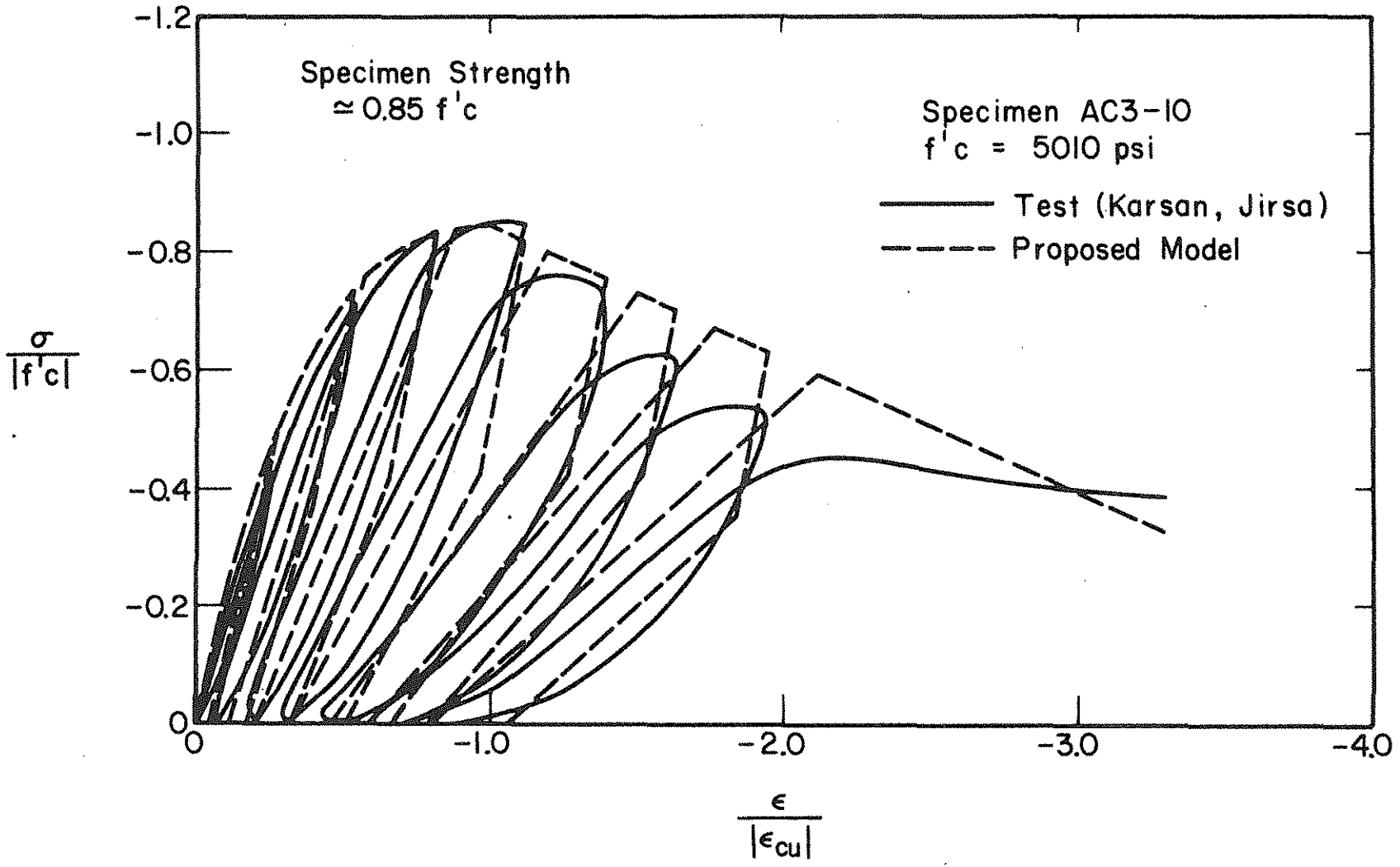

Figure 2.39 Comparison of Proposed Model with Cyclic Loading Producing Given Strain Increment (16,17)

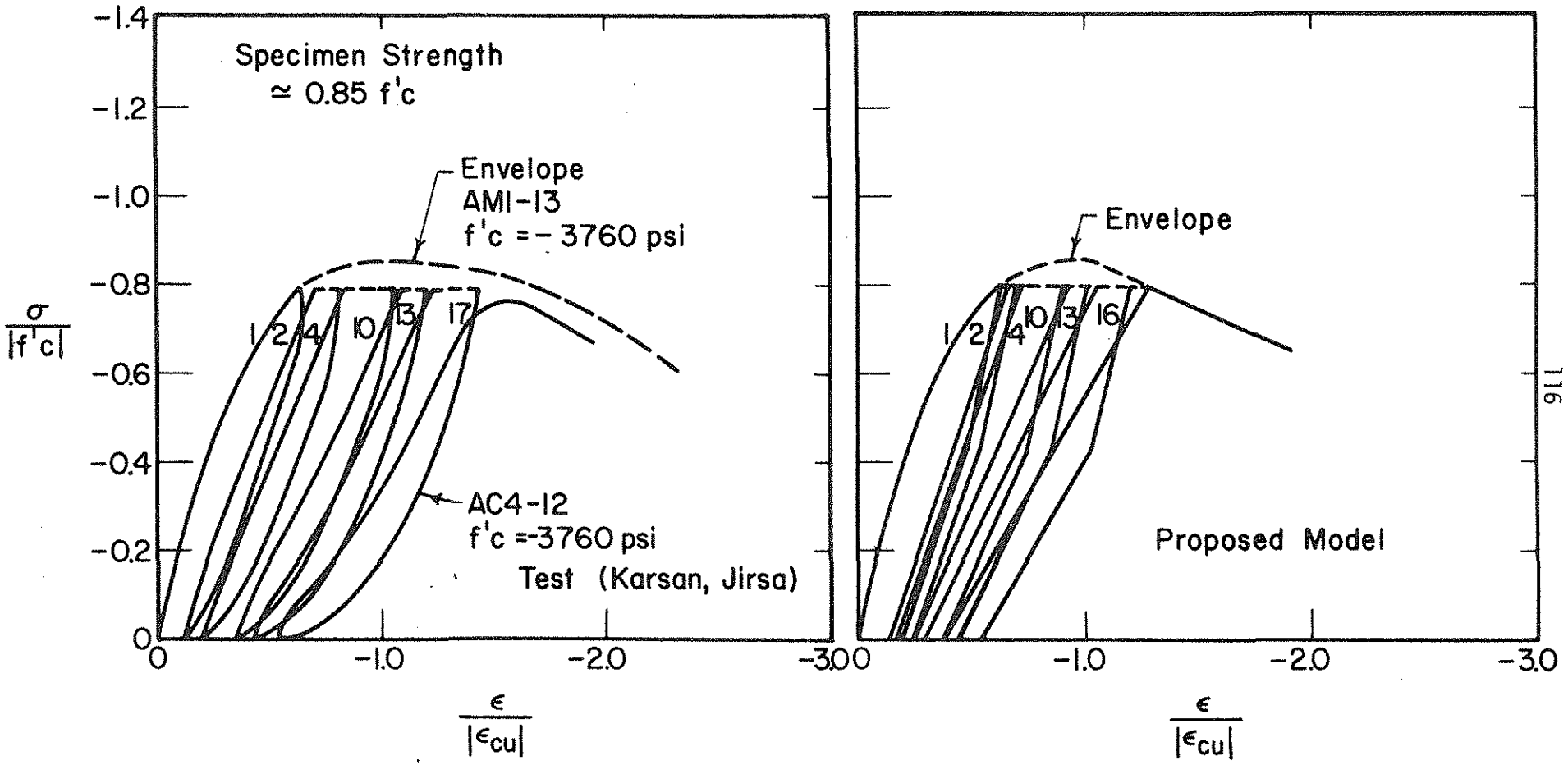

Figure 2.40 Comparison of Proposed Model with Cyclic Loading Between Fixed Stresses

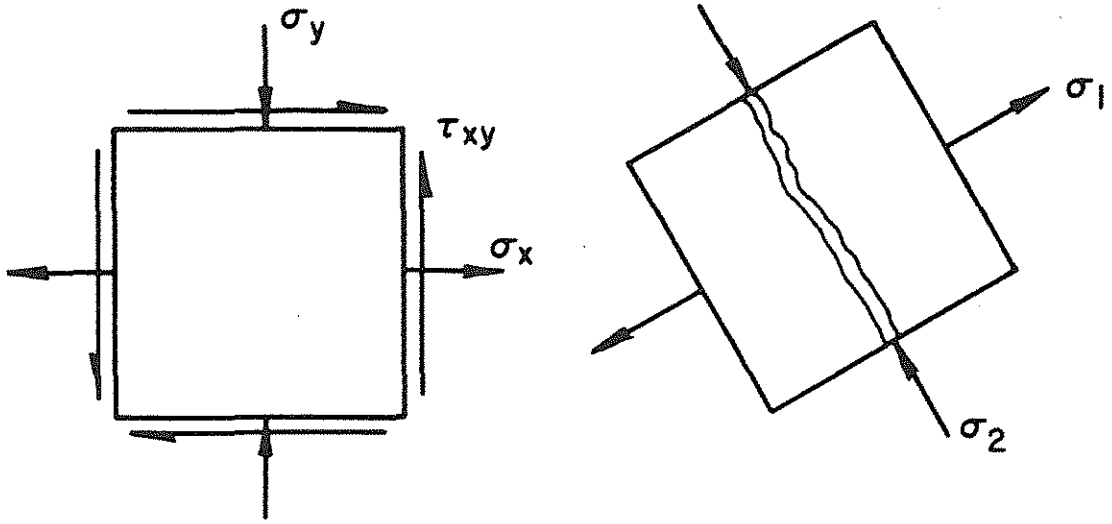

Figure 2.41a Crack Formation in Principal Tension Direction

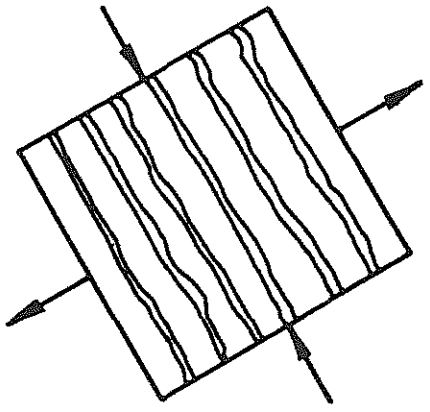

Figure 2.41b Idealization of a Single Crack

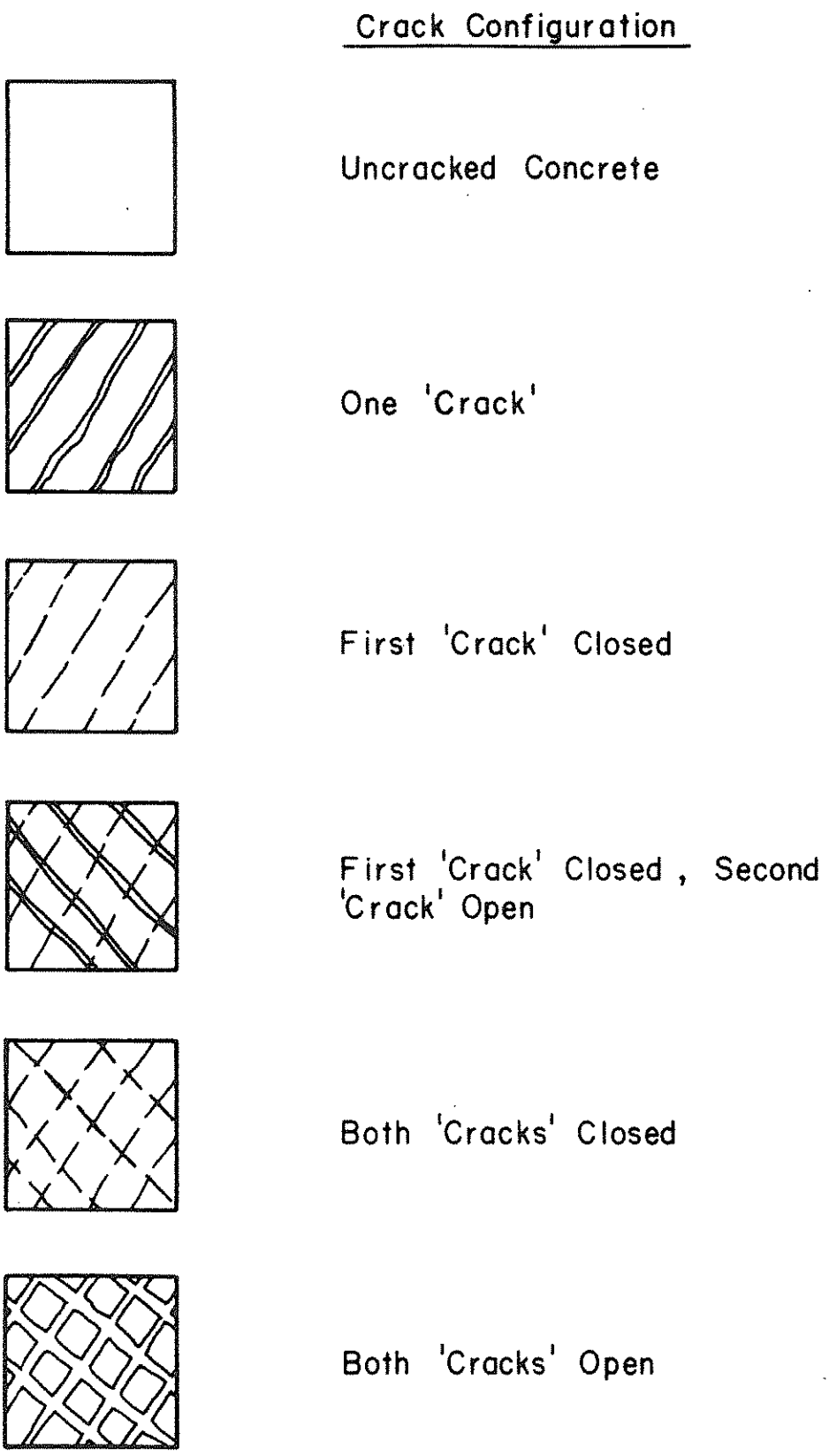

Figure 2.42 Possible Crack Configurations

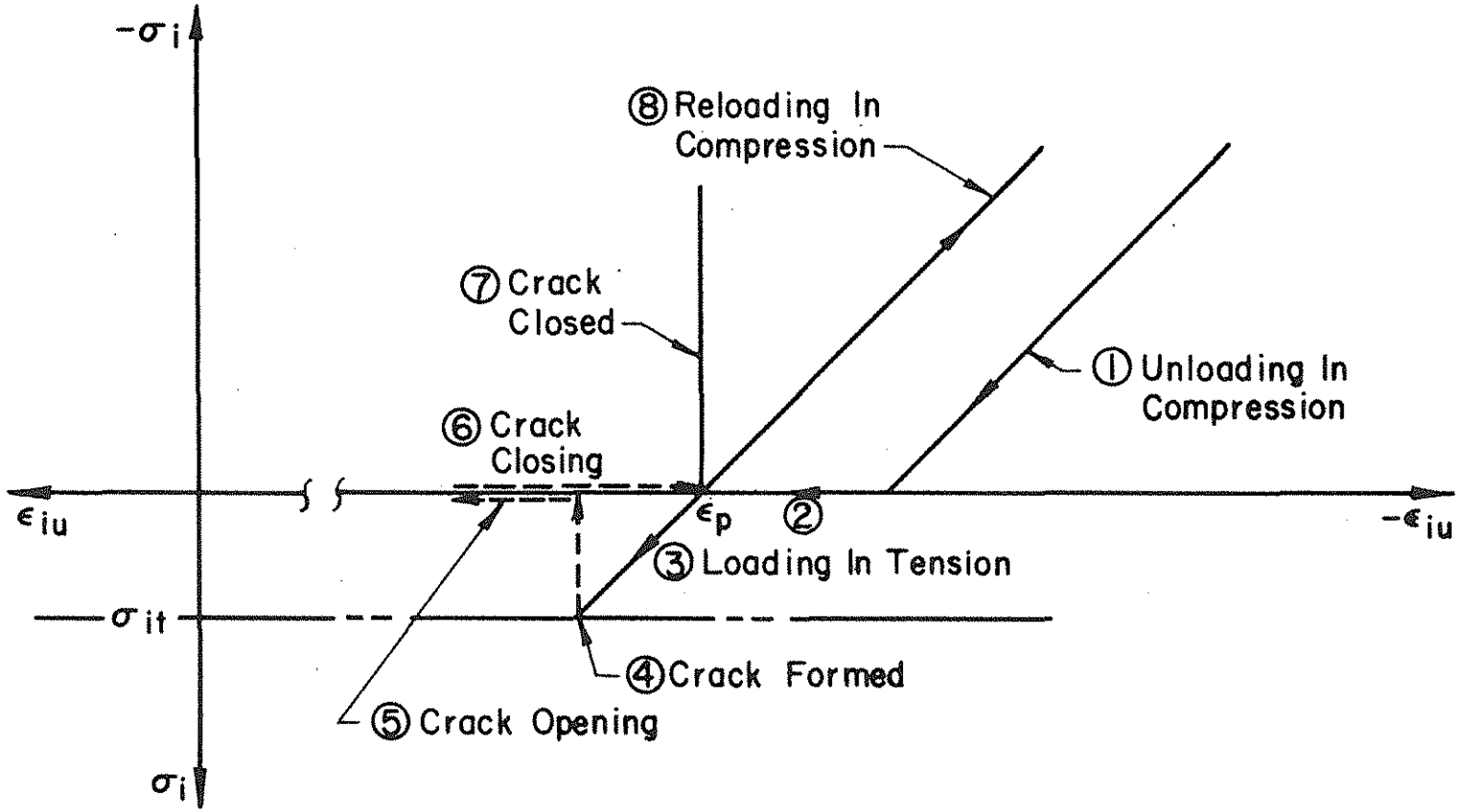

Figure 2.43 Crack Formation and Closing

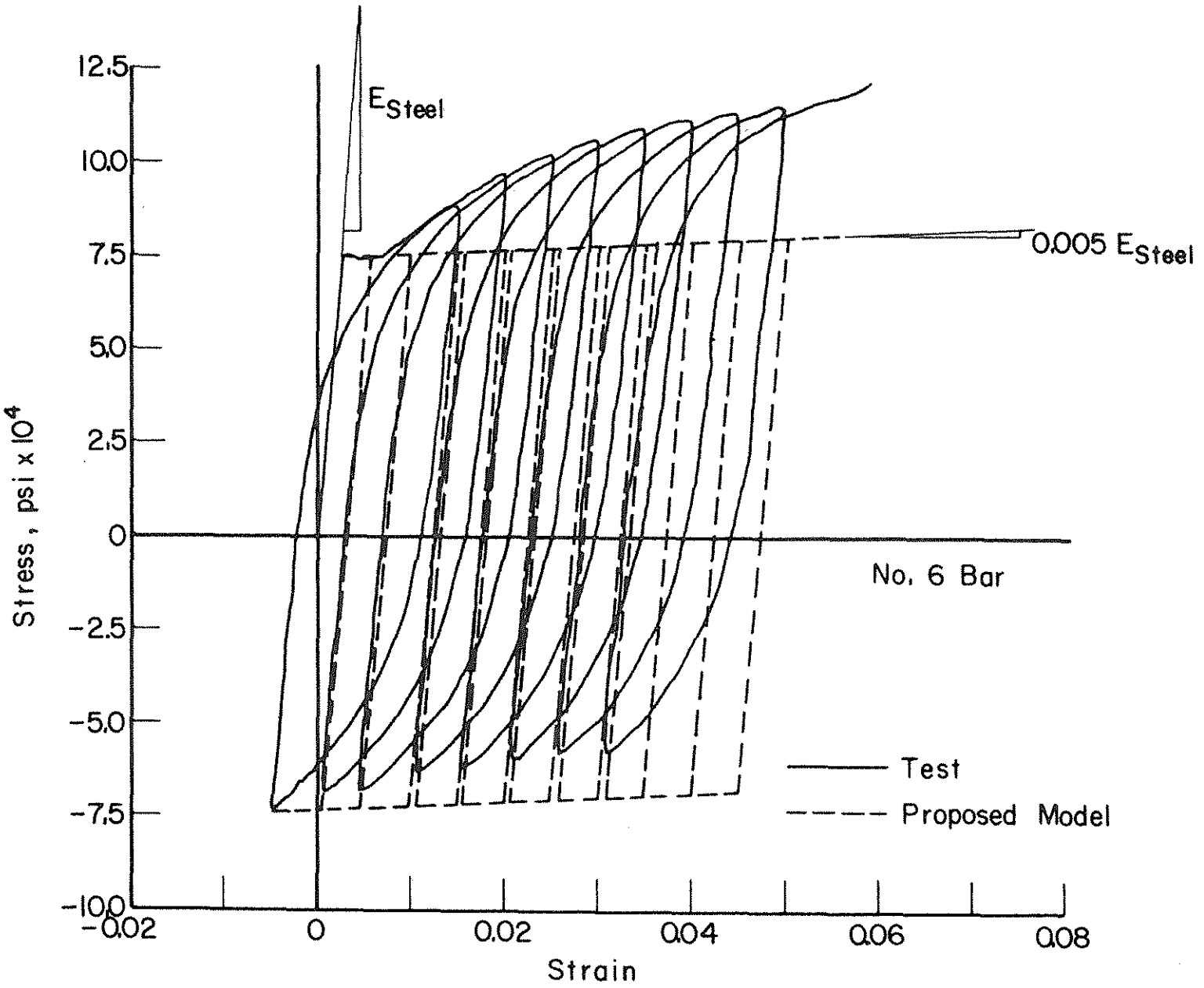

Figure 2.44 Cyclic Loading of Reinforcing Steel (1)

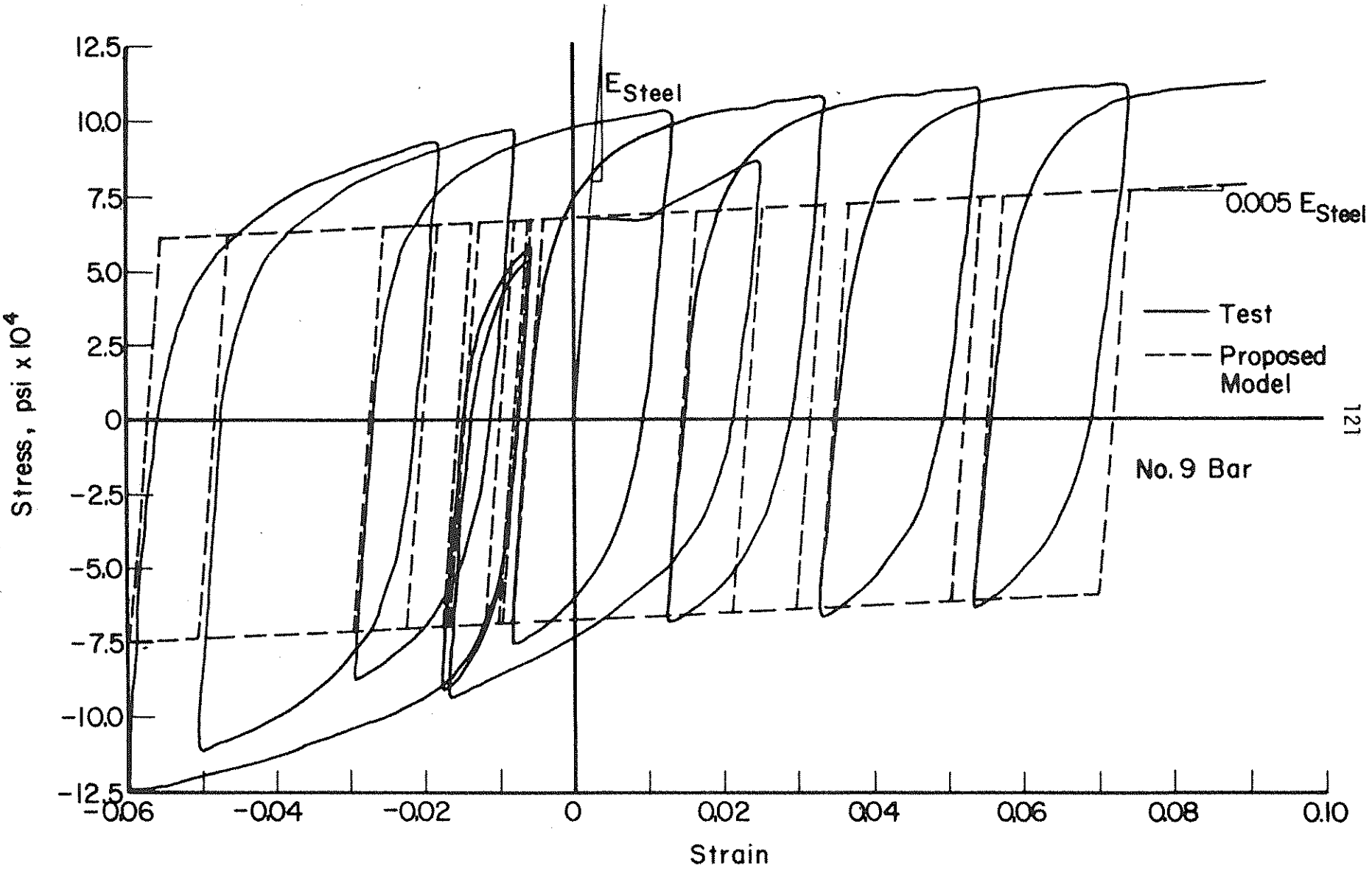

Figure 2.45 Cyclic Loading of Reinforcing Steel (1)

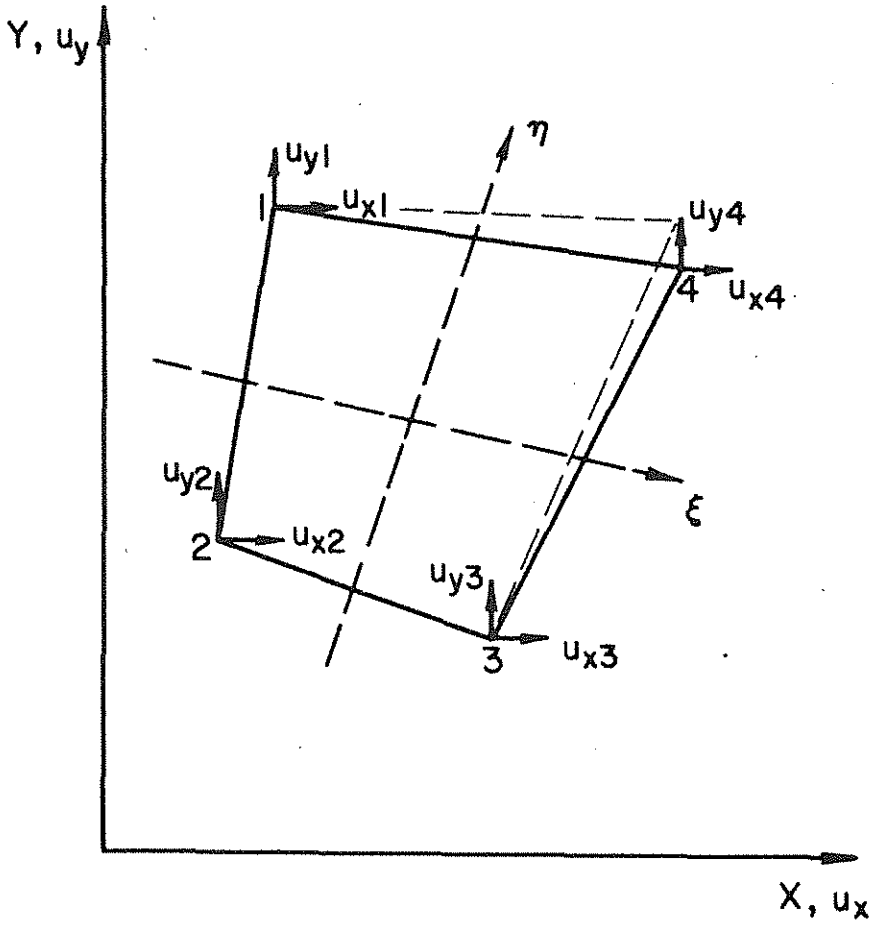

Figure 3.1a Compatible Displacement Modes for Quadrilateral Element

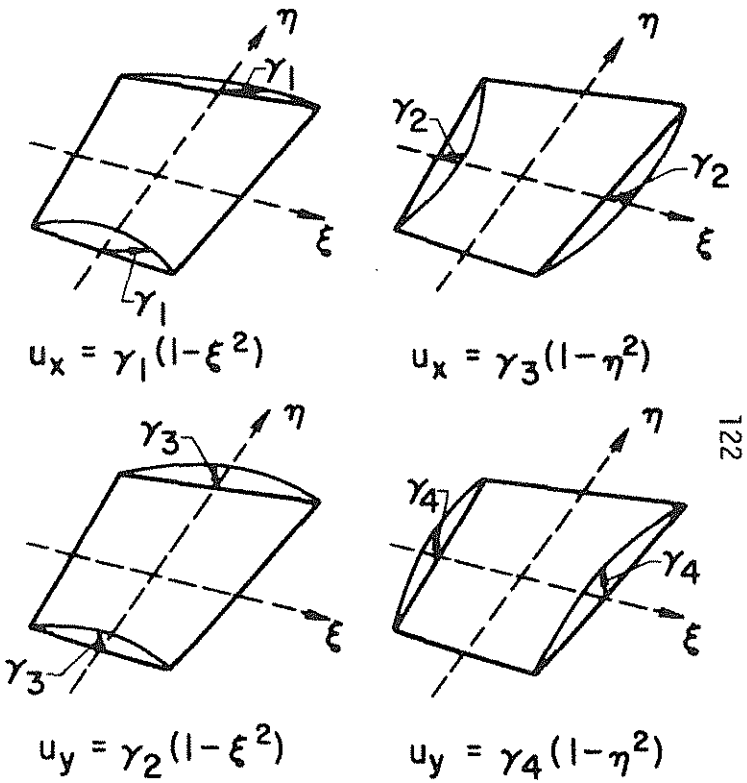

Figure 3.1b Incompatible Displacement Modes for Quadrilateral Element (41)

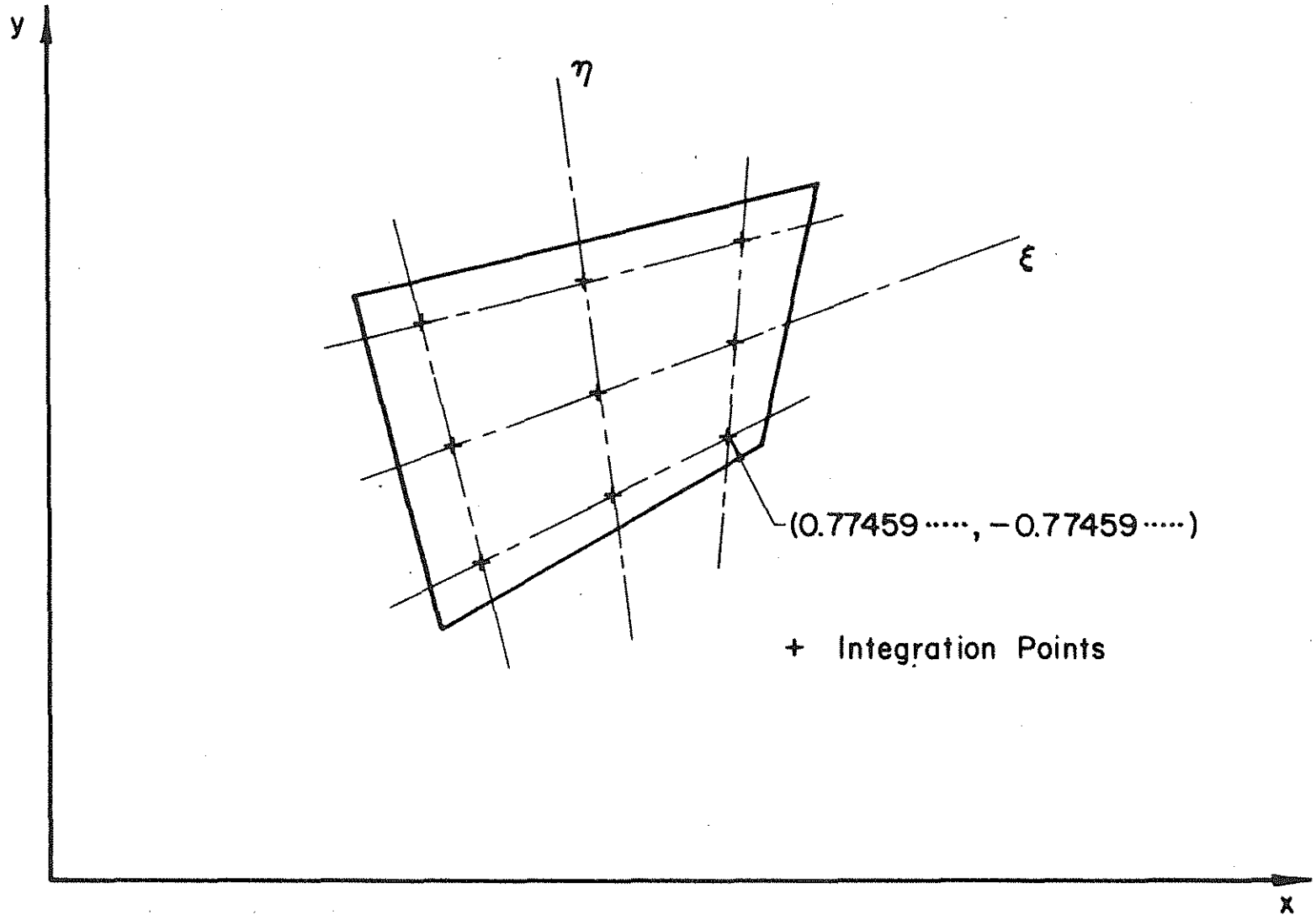

Figure 3.2 Location of Gaussian Integration Points in a 3 x 3 Grid

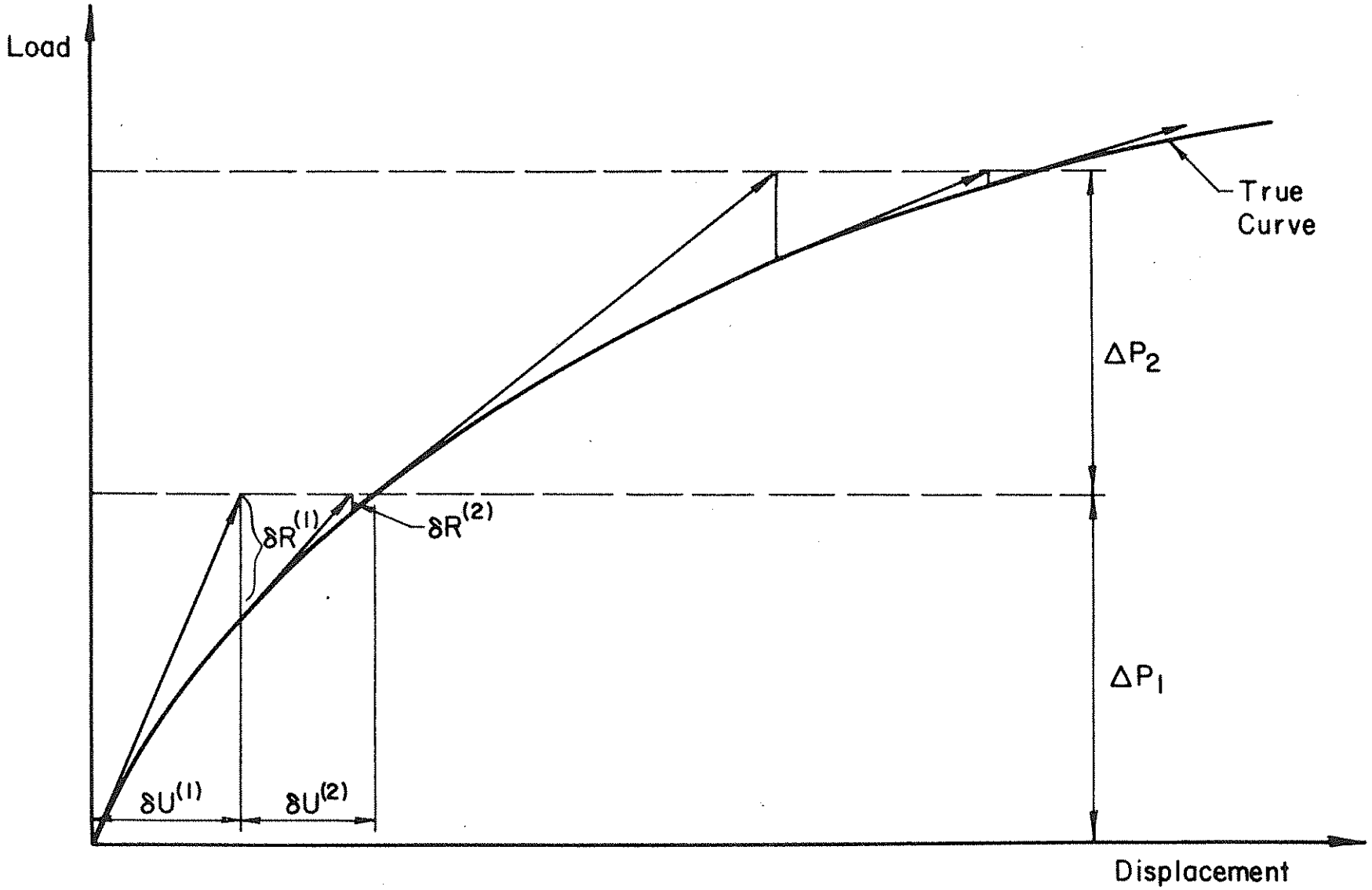

Figure 3.3 Adaptation of Initial Stress Method (44) - Forces, Stiffness Updated with Each Iteration

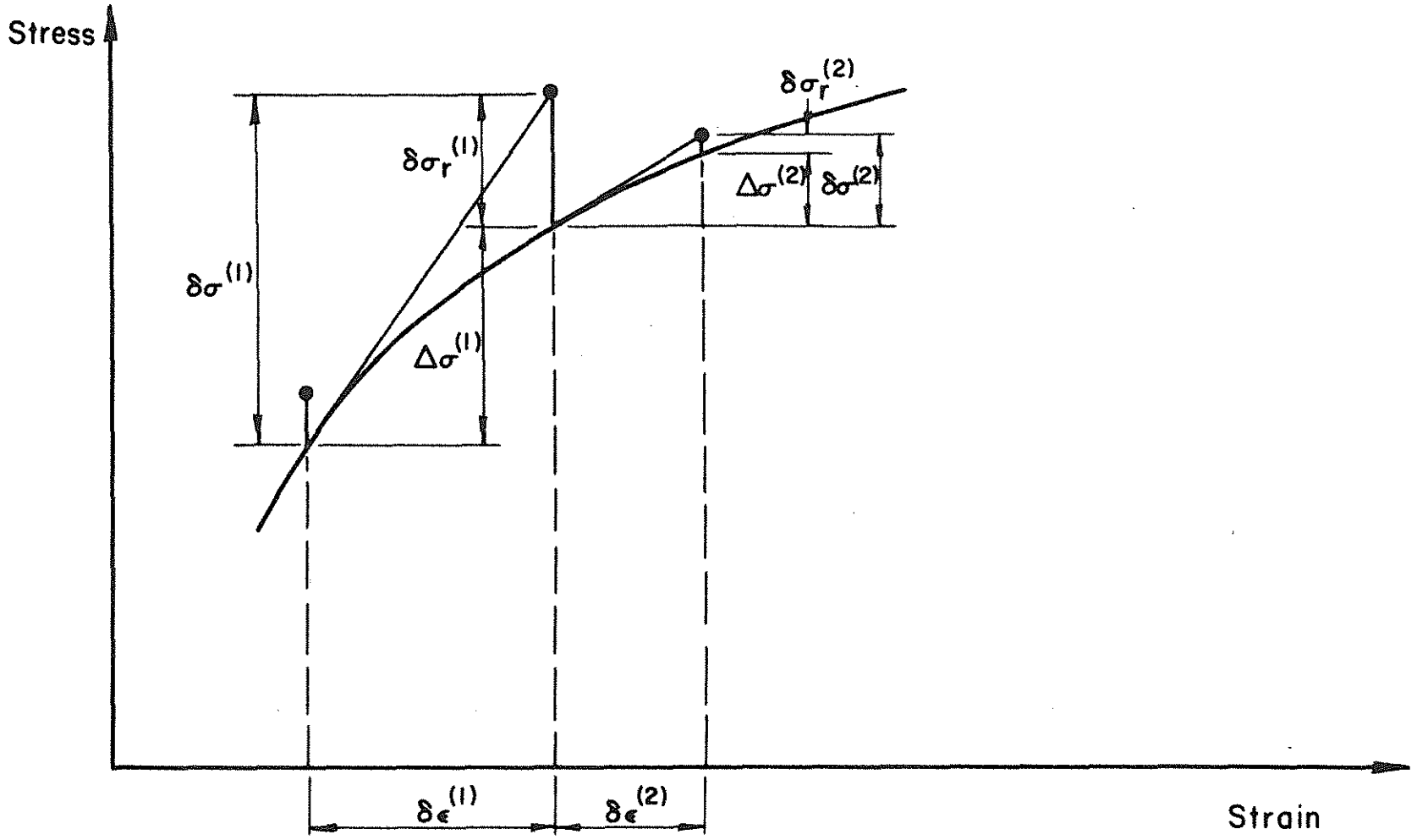

Figure 3.4 Adaptation of Initial Stress Method (44) - Stresses, Stiffness Updated with Each Iteration

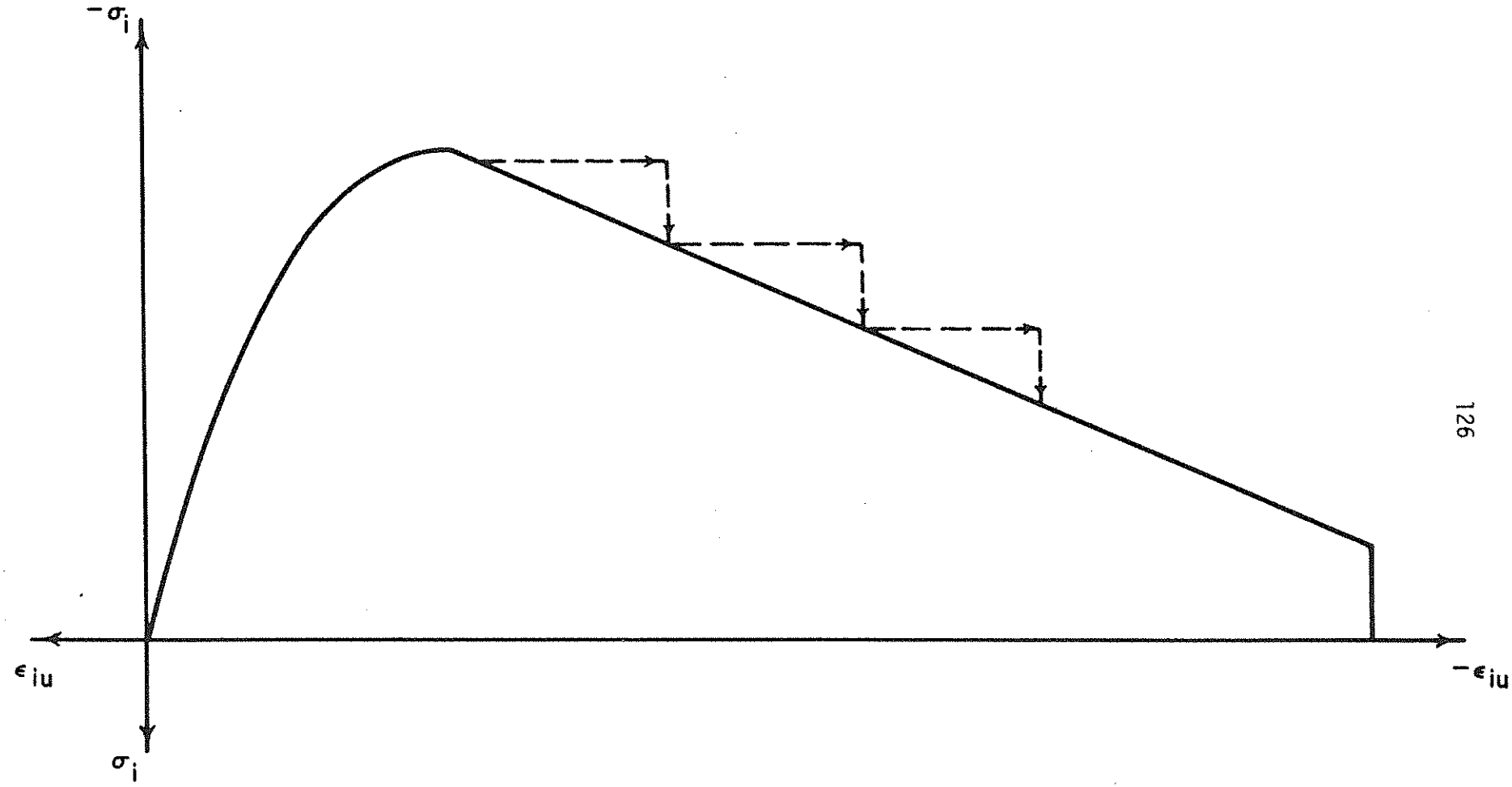

Figure 3.5 Solution Technique for Downward Portion of Stress-Strain Curve

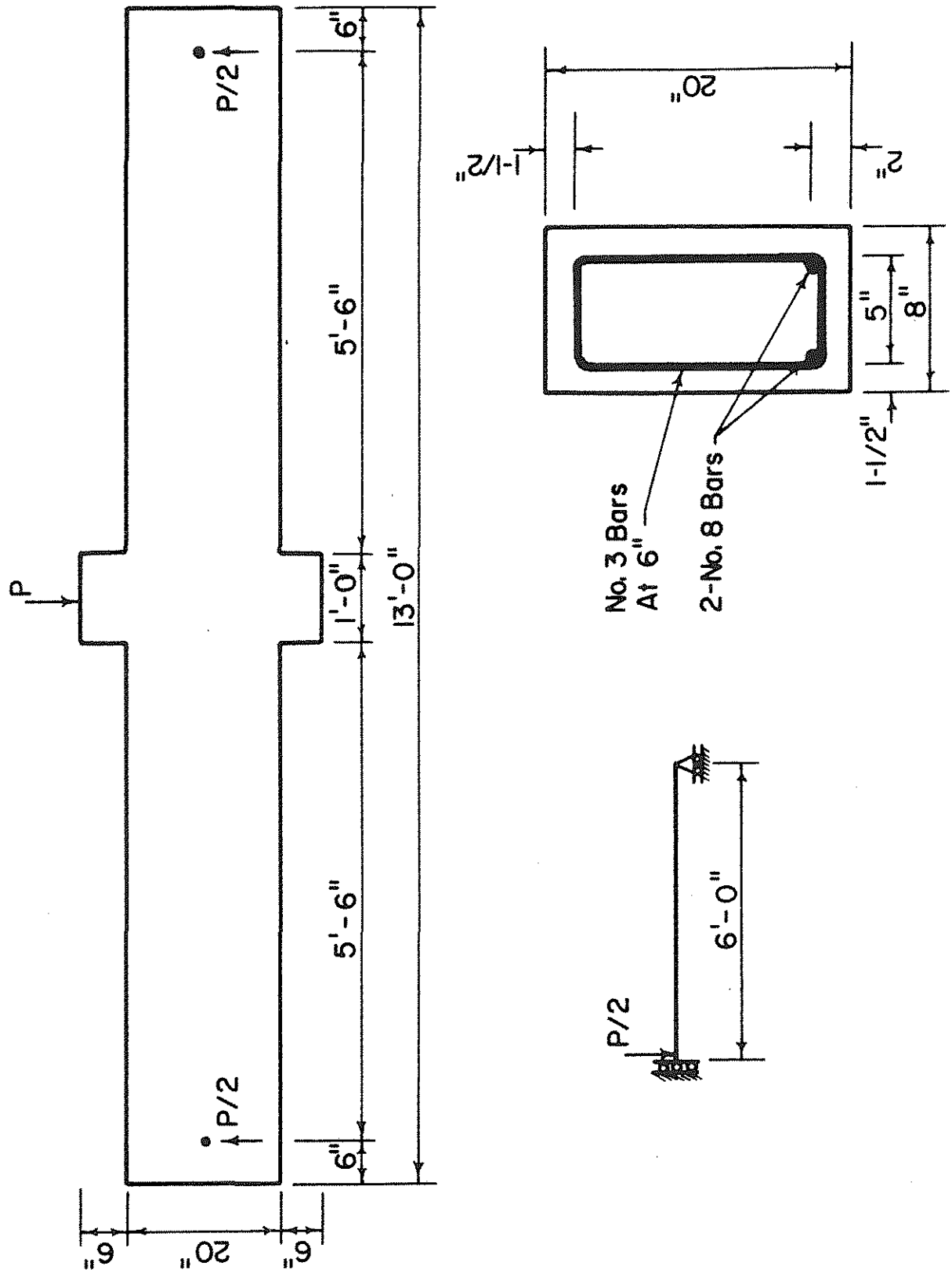

Figure 4.1 Beam Test Specimen J-4 (7)

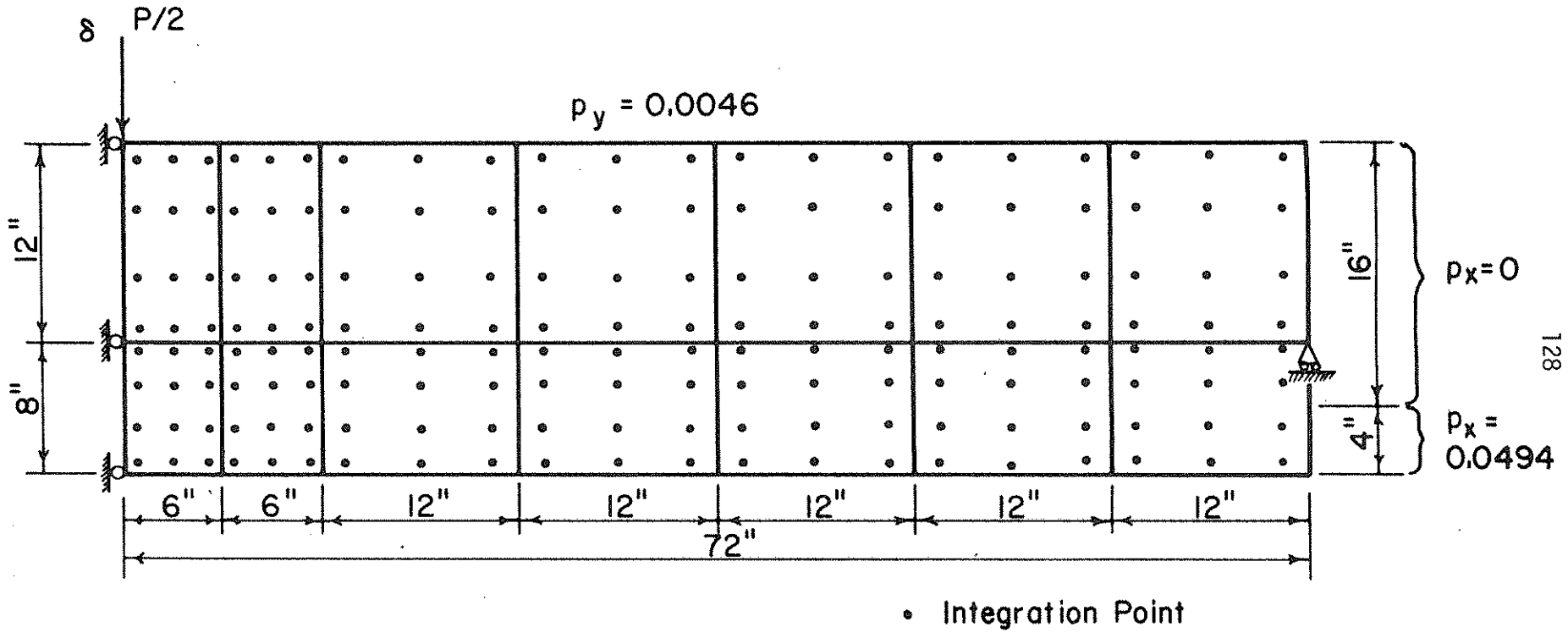

Figure 4.2 Finite Element Model of Beam Test Specimen J-4

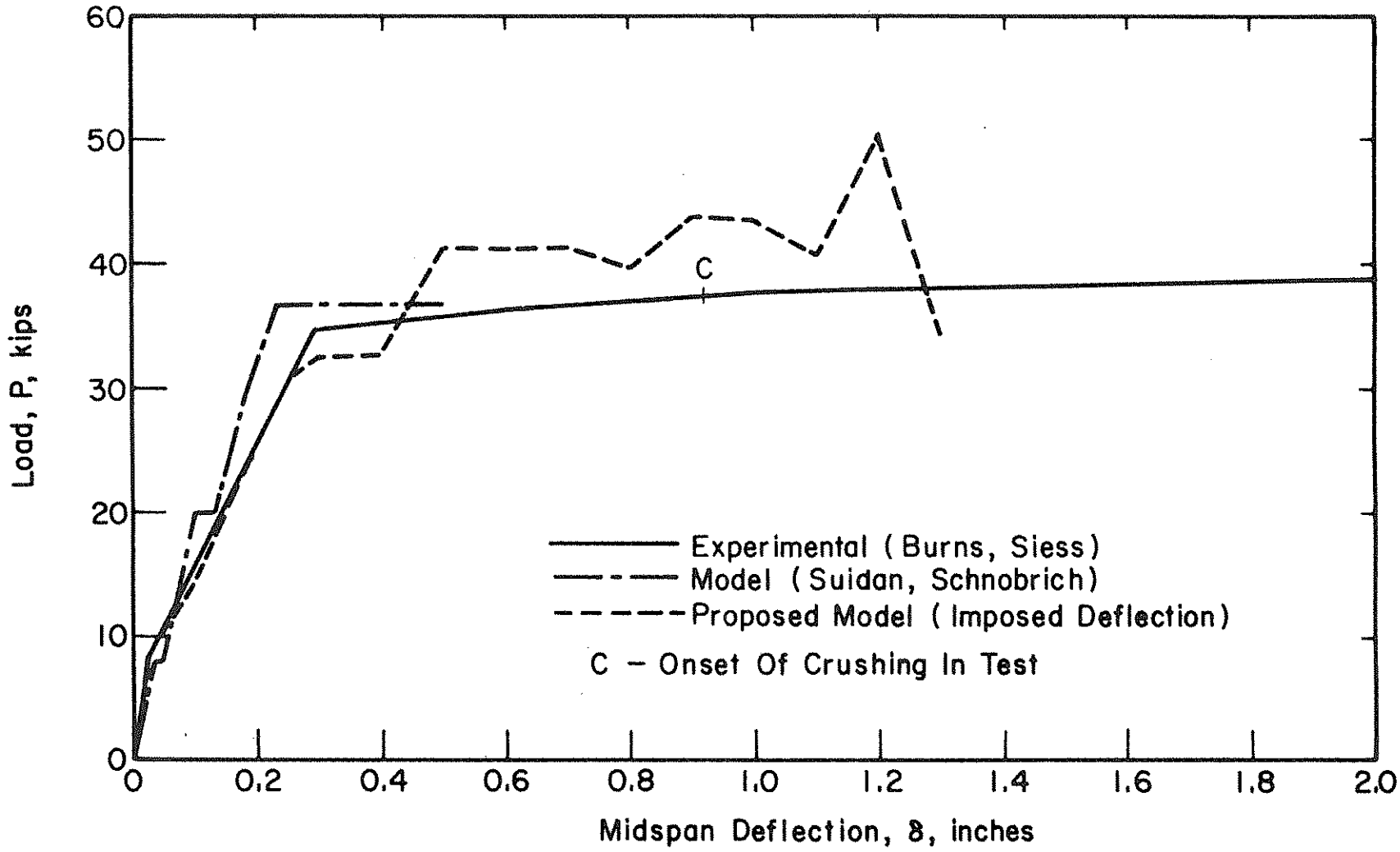

Figure 4.3 Load-Deflection Curves for Beam Test Specimen J-4 (7)

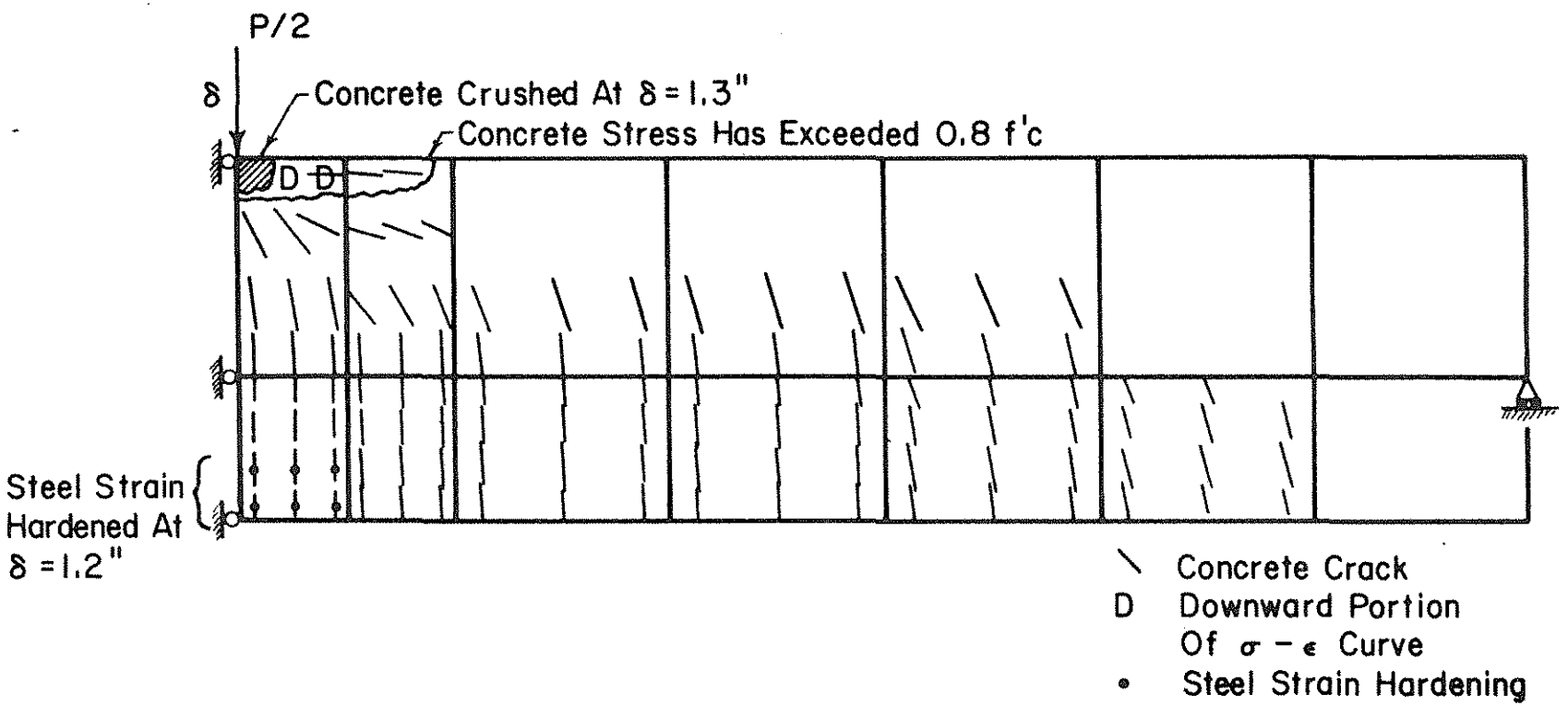

Figure 4.4 Analytical Crack Pattern for Beam Test Specimen J-4

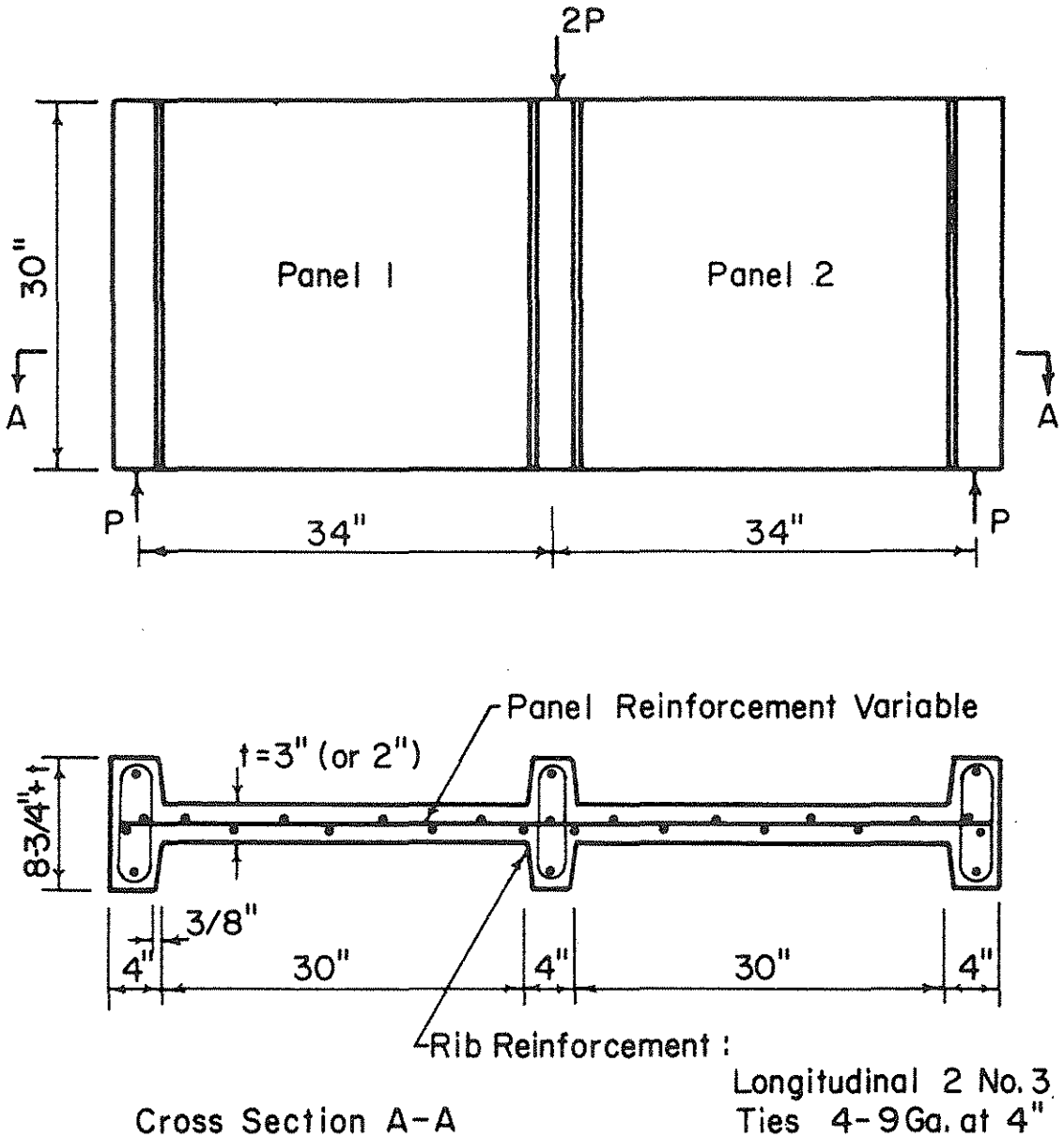

Figure 4.5 Shear Panel Test Specimens, W-1, W-2, W-4 (8)

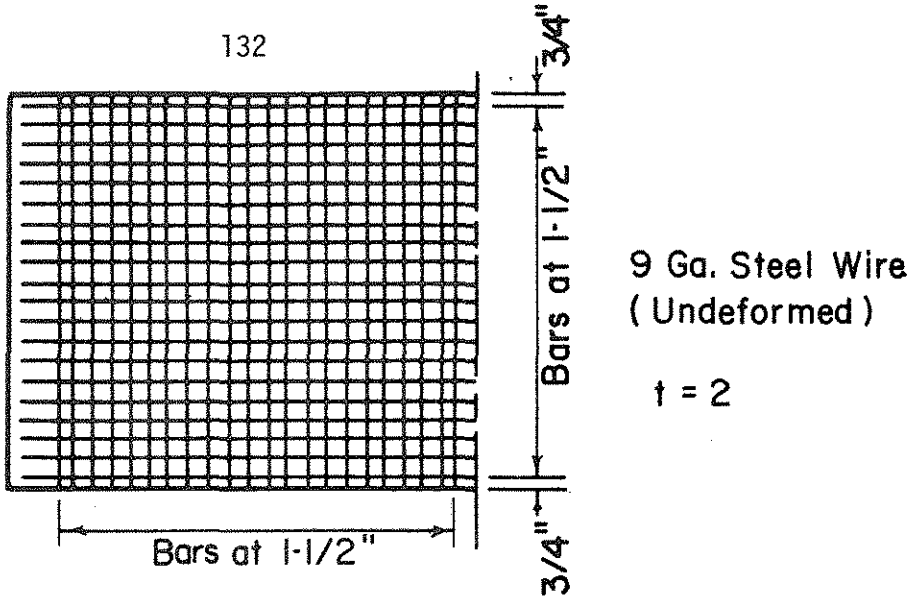

Figure 4.6a Reinforcing for Shear Panel W-1

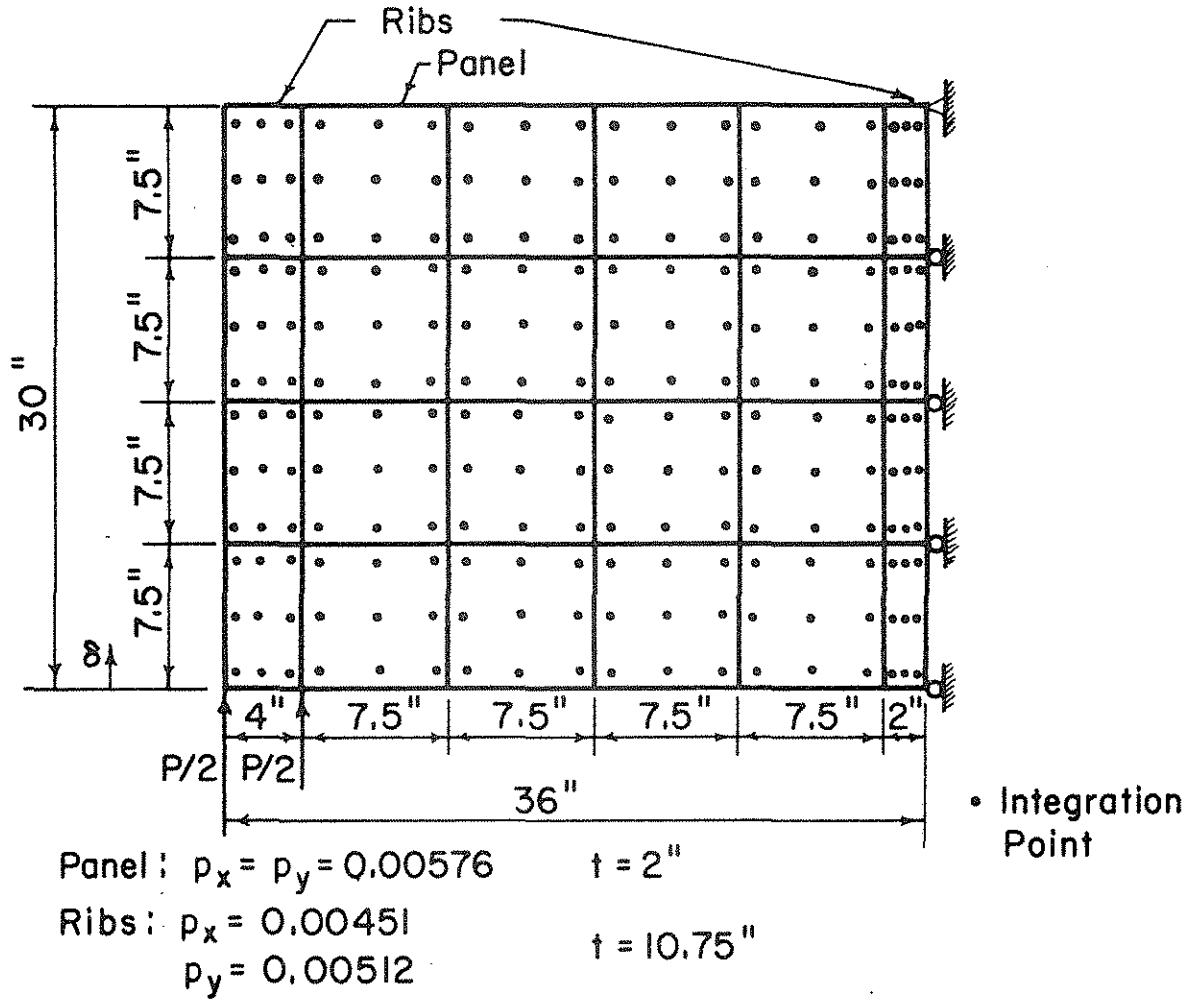

Figure 4.6b Finite Element Model of Shear Panel W-1

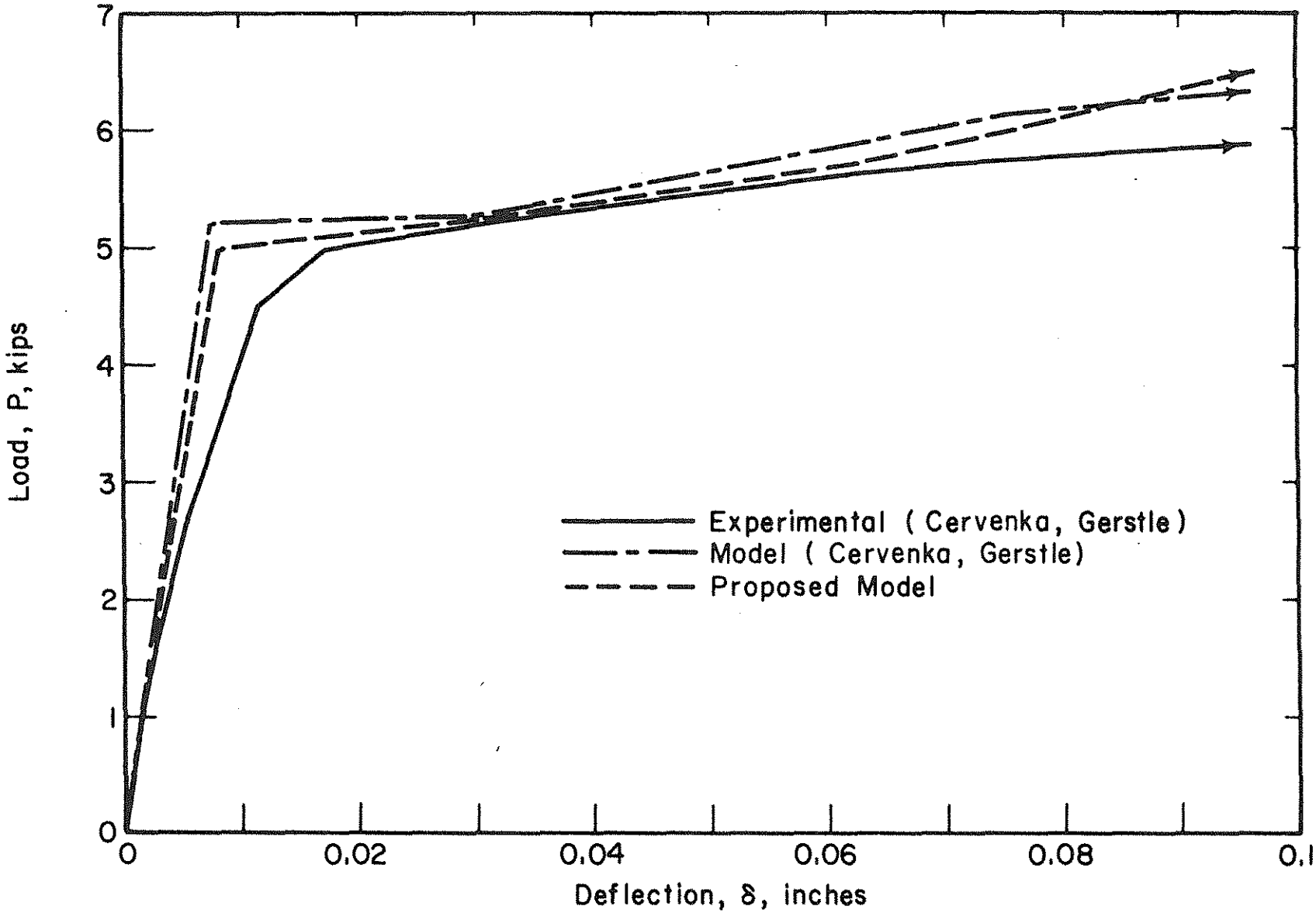

Figure 4.7 Load-Deflection Curves for Shear Panel W-1 (8,10)

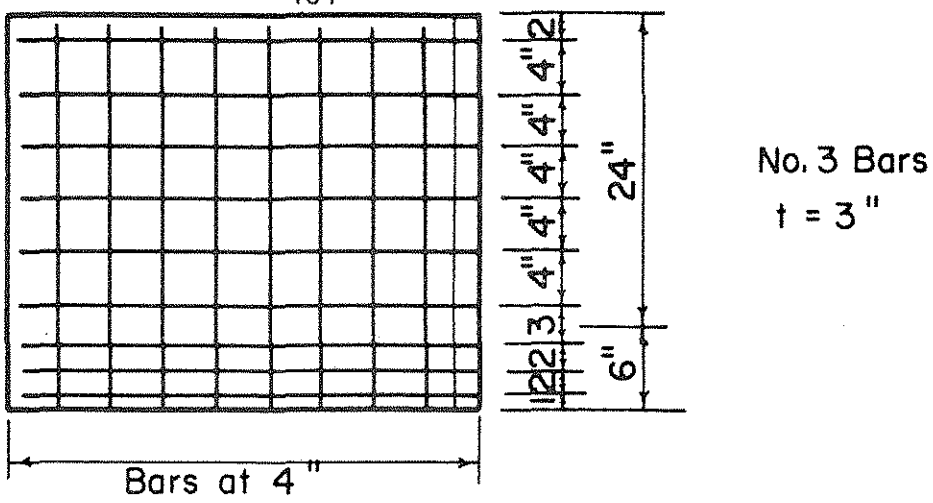

Figure 4.8a Reinforcing for Shear Panel W-2

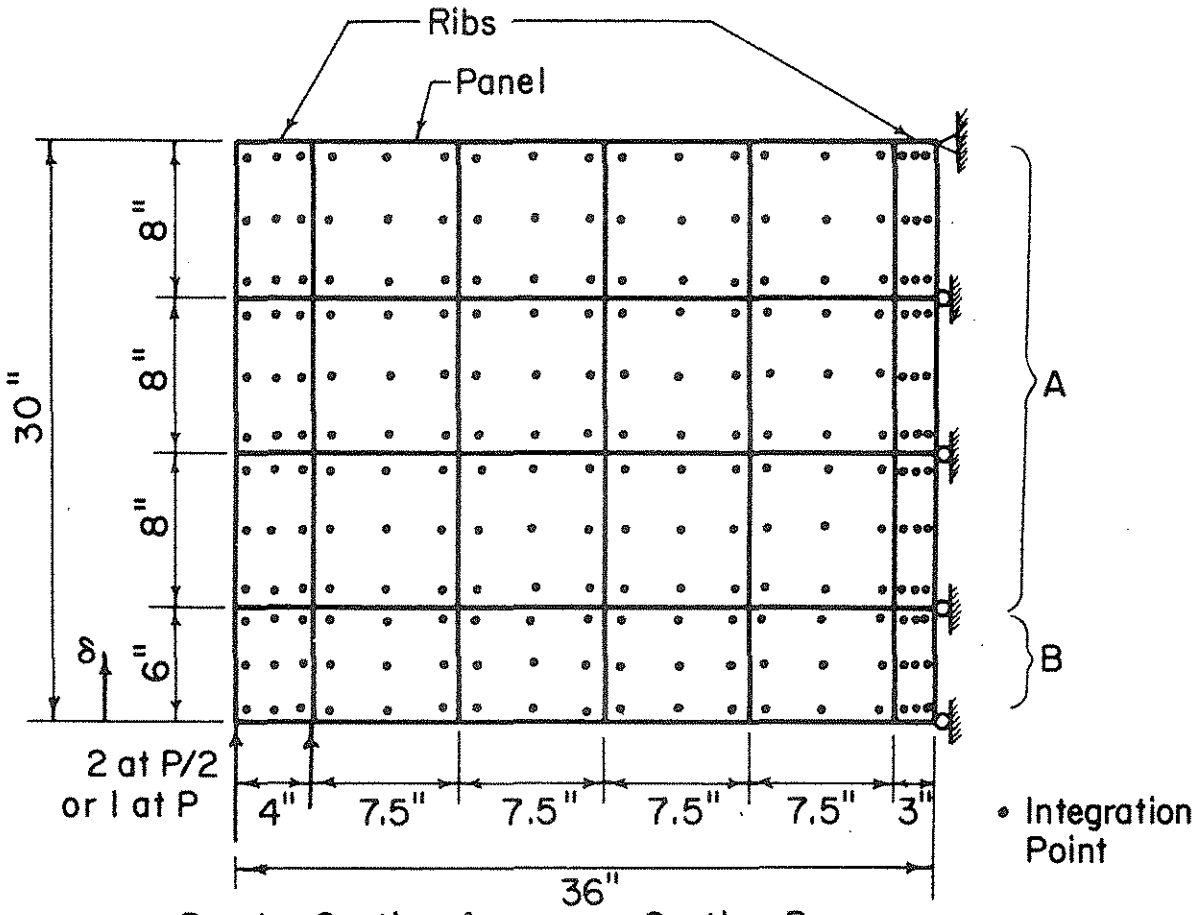

	Section A	Section B	
Panel :	$p_x = p_y = 0.00917$	$p_x = 0.01833$ $p_y = 0.00917$	t = 3"
Ribs :	$p_x = 0.00528$ $p_y = 0.00468$	$p_x = 0.01326$ $p_y = 0.00468$	t = 11.75"

Figure 4.8b Finite Element Model of Shear Panel W-2

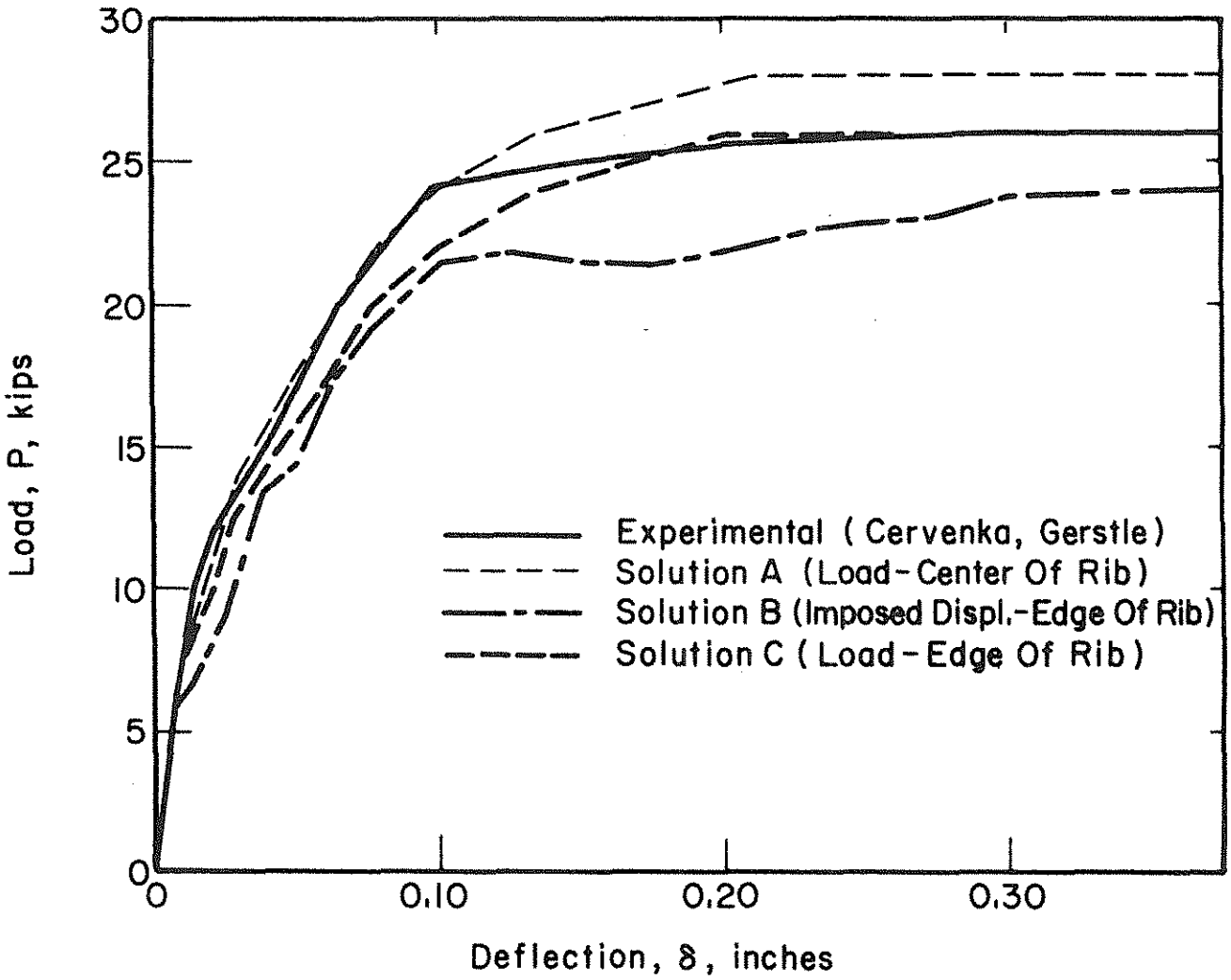

Figure 4.9 Load-Deflection Curves for Shear Panel W-2 (8,10)

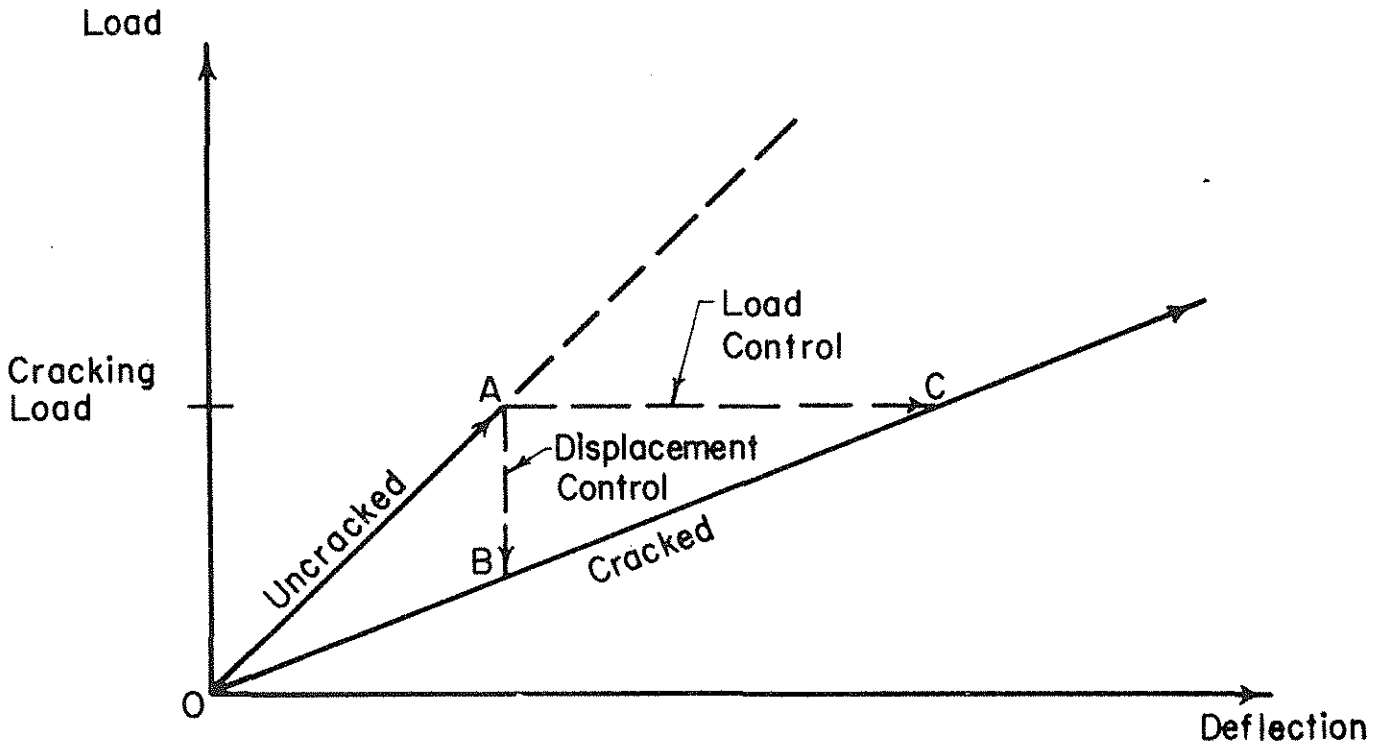

Figure 4.10 Load-Deflection Curves for Cracked and Uncracked Sections

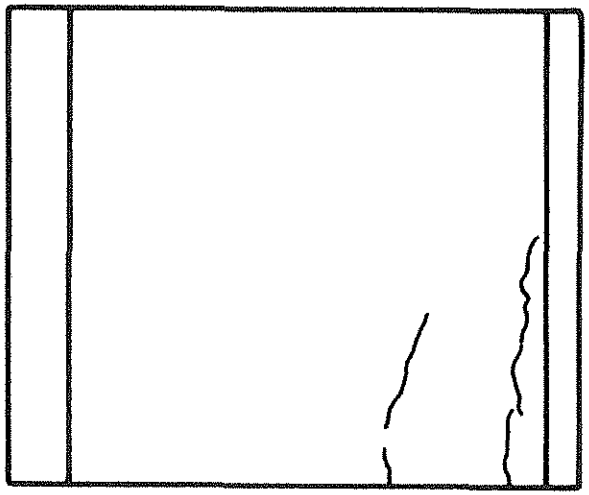

Experimental (Cervenka, Gerstle)

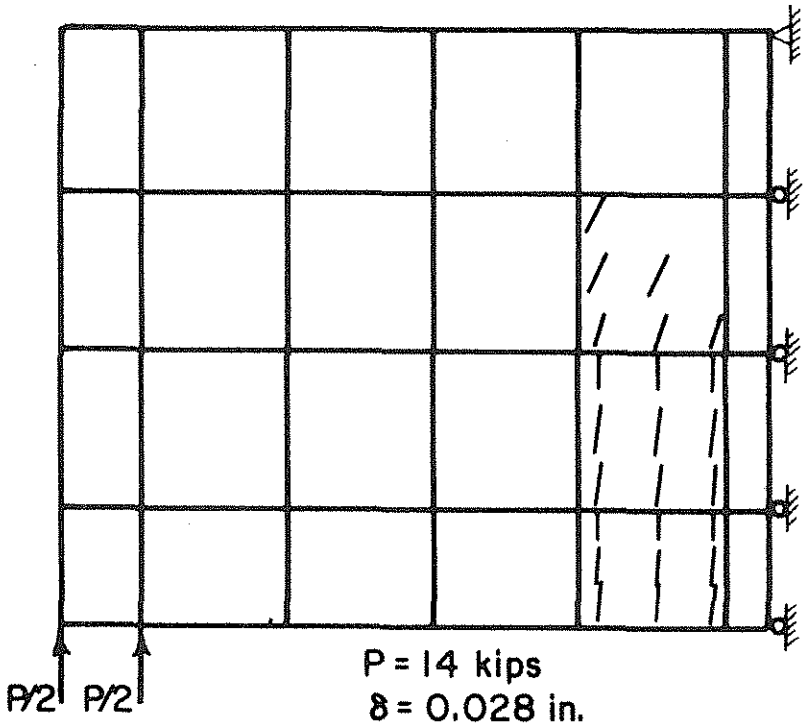

Analytical - "Center" Load On Rib

Figure 4.11 Comparison of Analytical and Experimental Crack Patterns for Shear Panel W-2

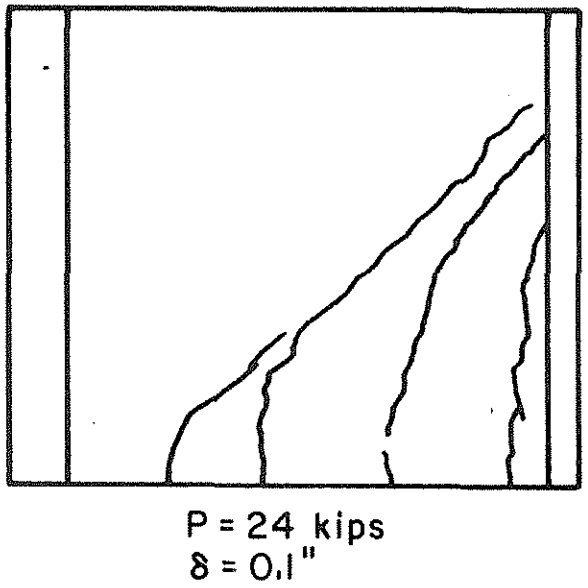

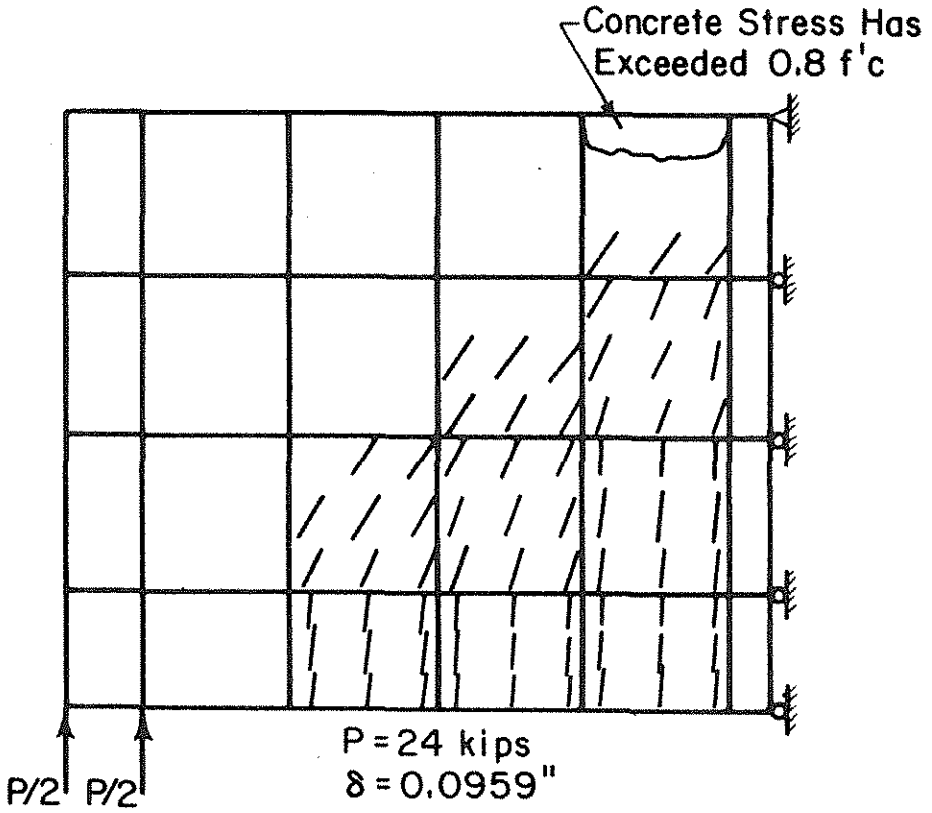

Figure 4.11 (Continued)

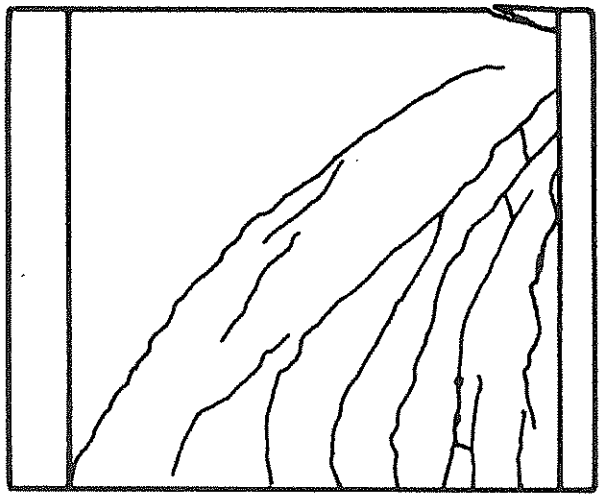

P = 25.5 kips
δ = 0.350"

Experimental (Cervenka, Gerstle)

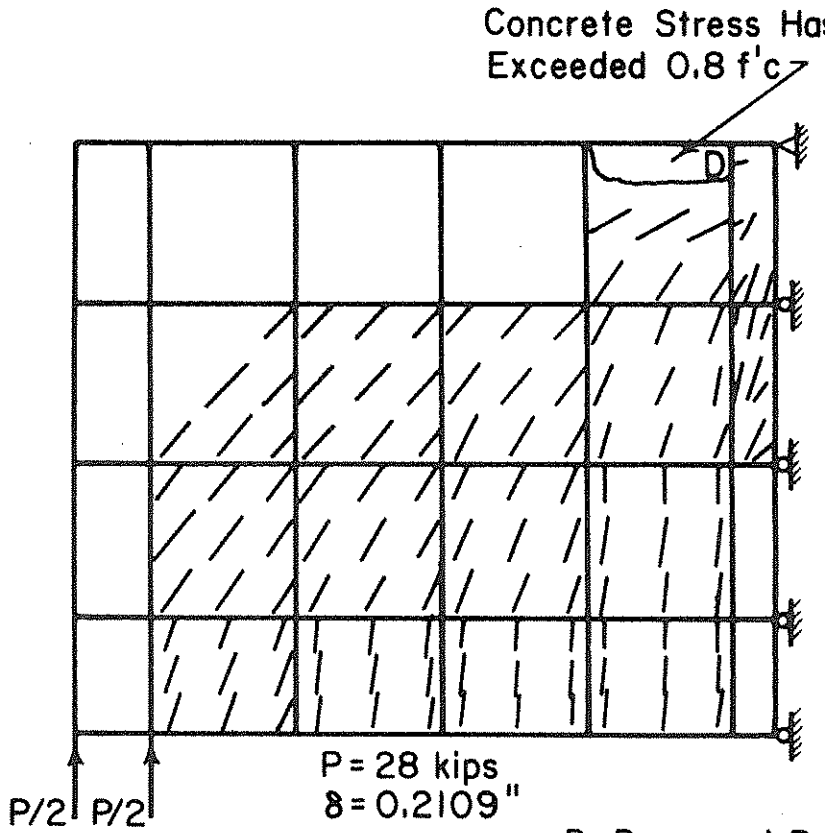

Analytical-"Center" Load On Rib

Figure 4.12 Comparison of Analytical and Experimental Crack Patterns for Shear Panel W-2 on "Yield" Plateau

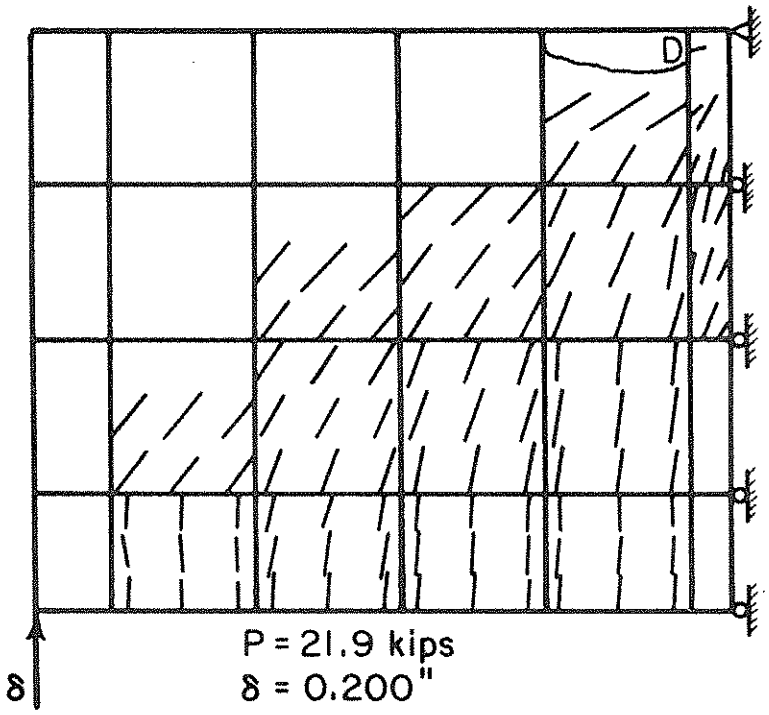

Analytical - Imposed Edge Displacement

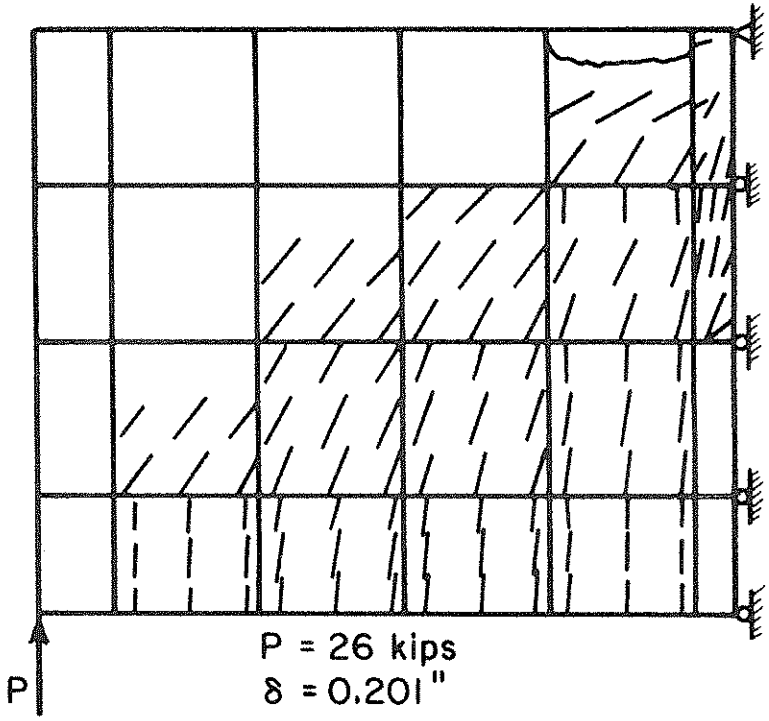

Analytical - Concentrated Edge Load

Figure 4.12 (Continued)

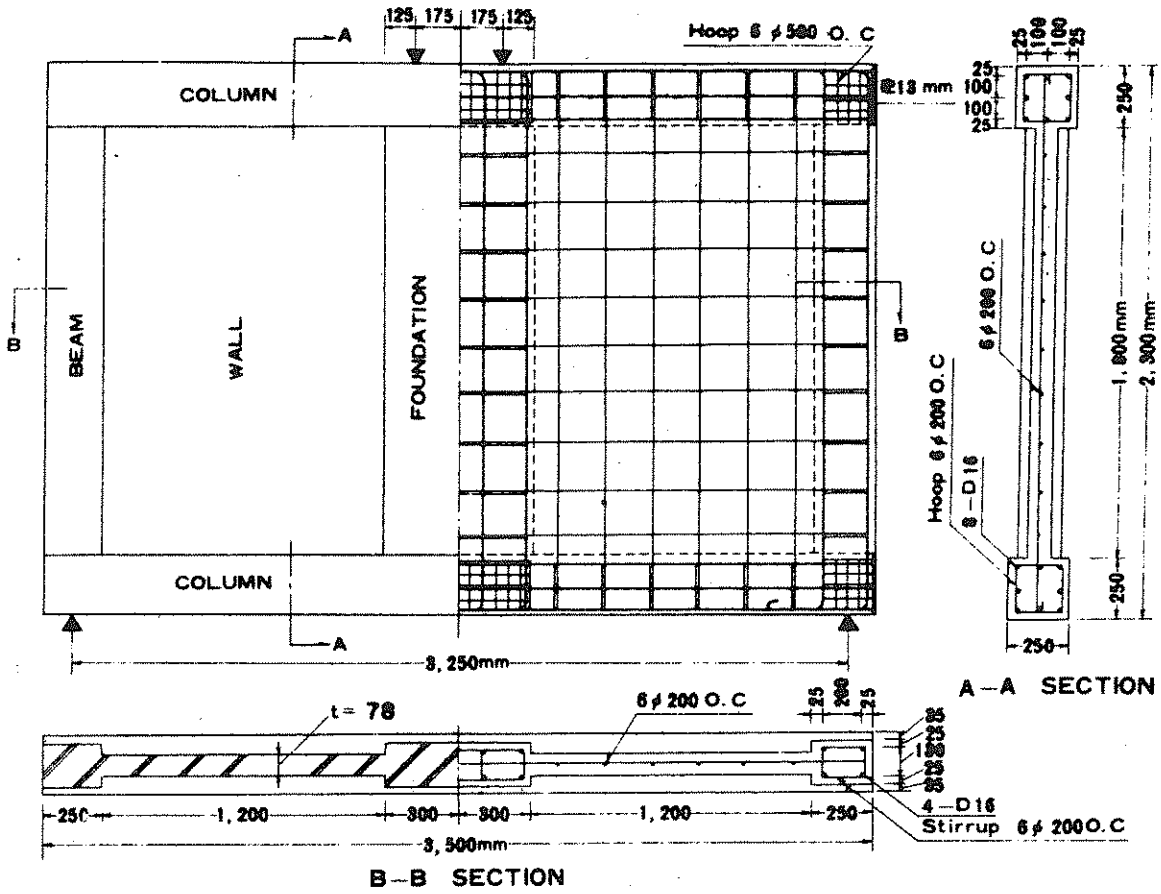

Figure 4.13 Shear Wall-Frame System A-1 (38)

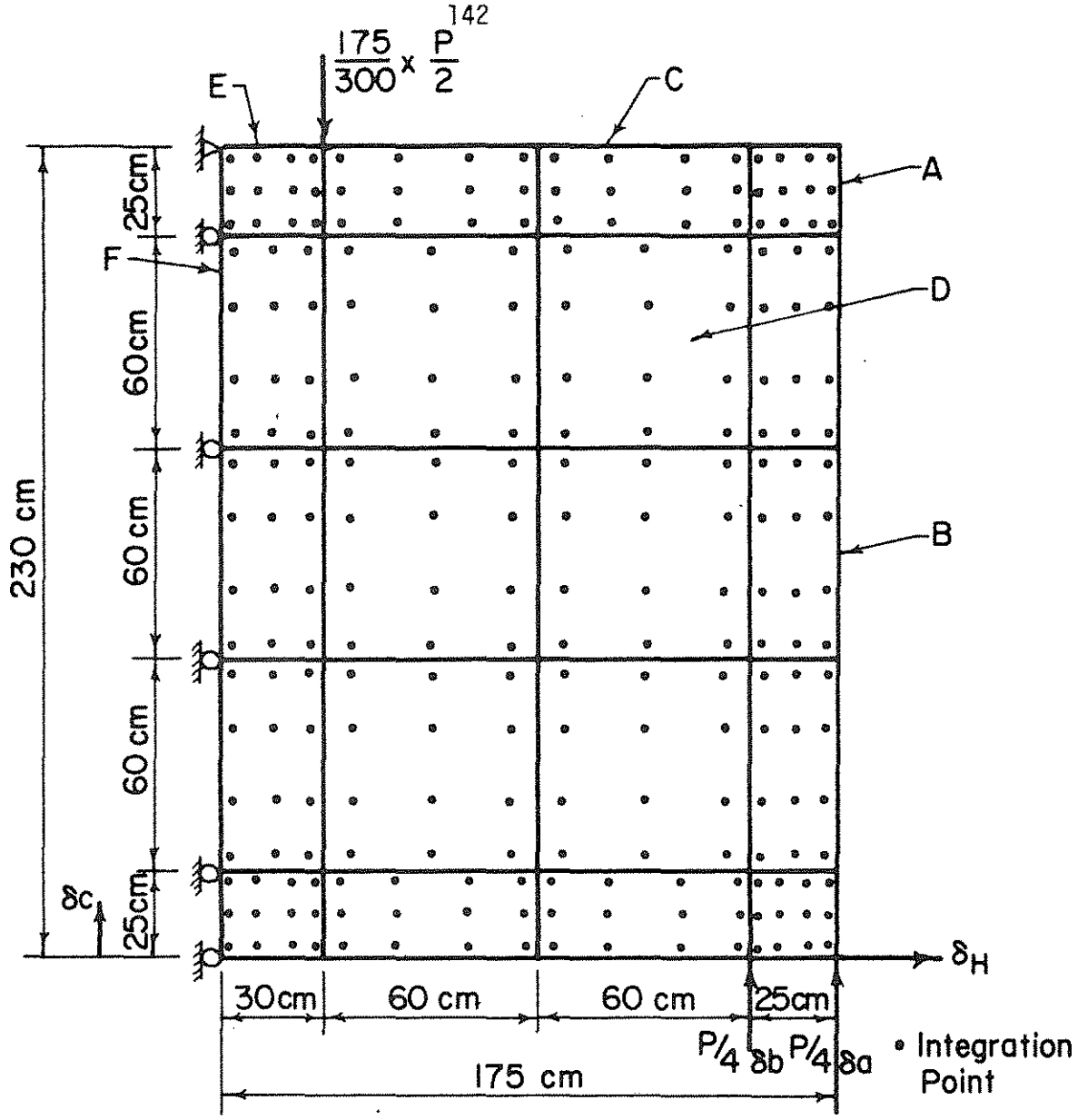

A. Beam - Column Connection
$p_x = 0.03024$
$p_y = 0.01787$
t = 25 cm

B. Beam
$p_x = 0.002355$
$p_y = 0.01787$
t = 18 cm

C. Column
$p_x = 0.02573$
$p_y = 0.001696$
t = 25 cm

D. Wall
$p_x = p_y = 0.001812$ t = 7.8 cm

$$\delta = \frac{\delta a + \delta b}{2} - \delta c$$

$$\delta_{L,R} = \delta a - \delta c$$

E. Column-Foundation Connection
$p_x = 0.03024$
$p_y = 0.01169$
t = 25 cm

F. Foundation
$p_x = 0.002355$
$p_y = 0.01489$
t = 18 cm

Figure 4.14 Finite Element Model of Shear Wall-Frame System A-1

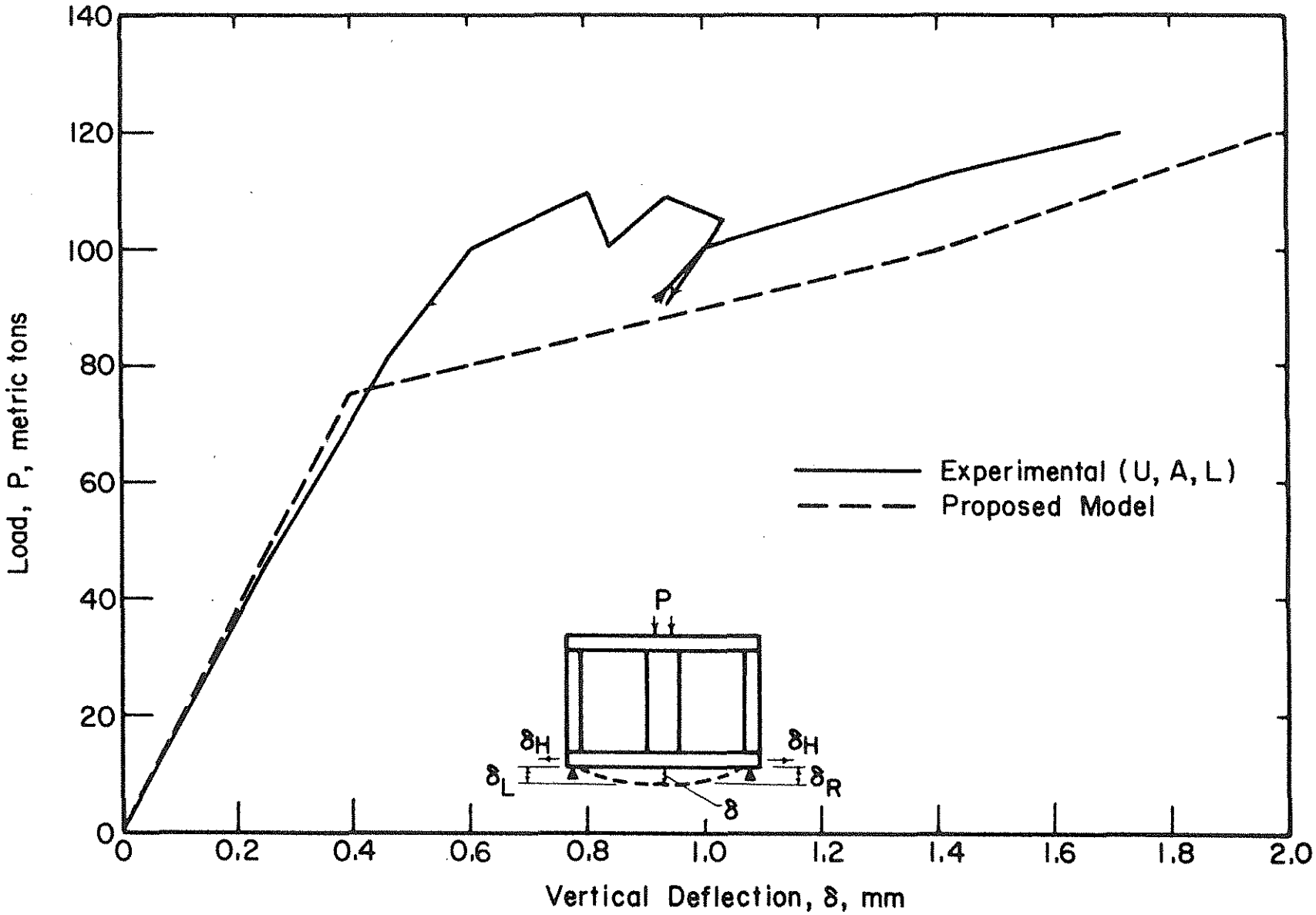

Figure 4.15 Initial Portion of Load-Deflection Curves for Shear Wall-Frame System A-1 (42)

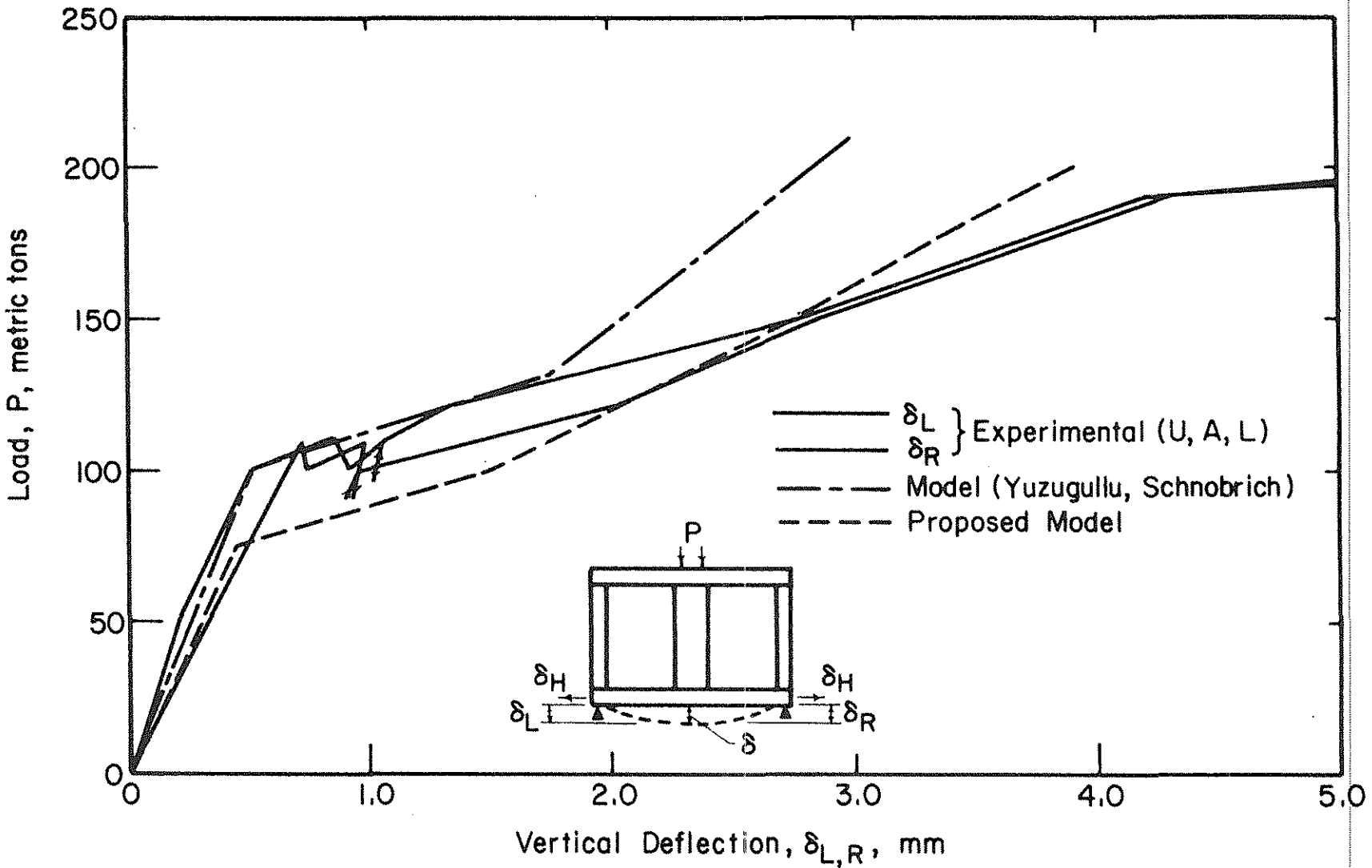

Figure 4.16 Load-Deflection Curves for Shear Wall-Frame System A-1 (42)

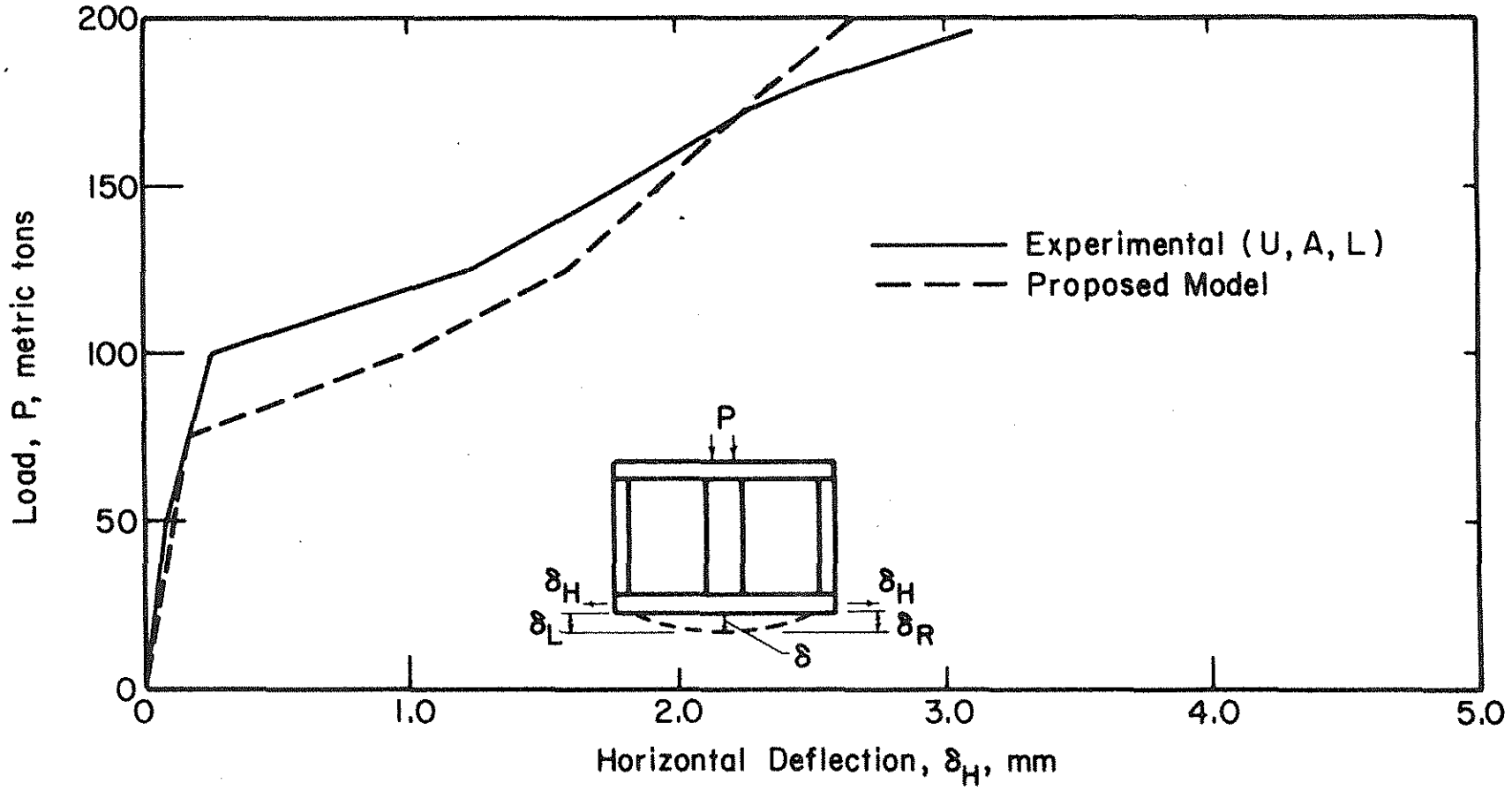

Figure 4.17 Load-Horizontal Deflection Curves for Shear Wall-Frame System A-1 (42)

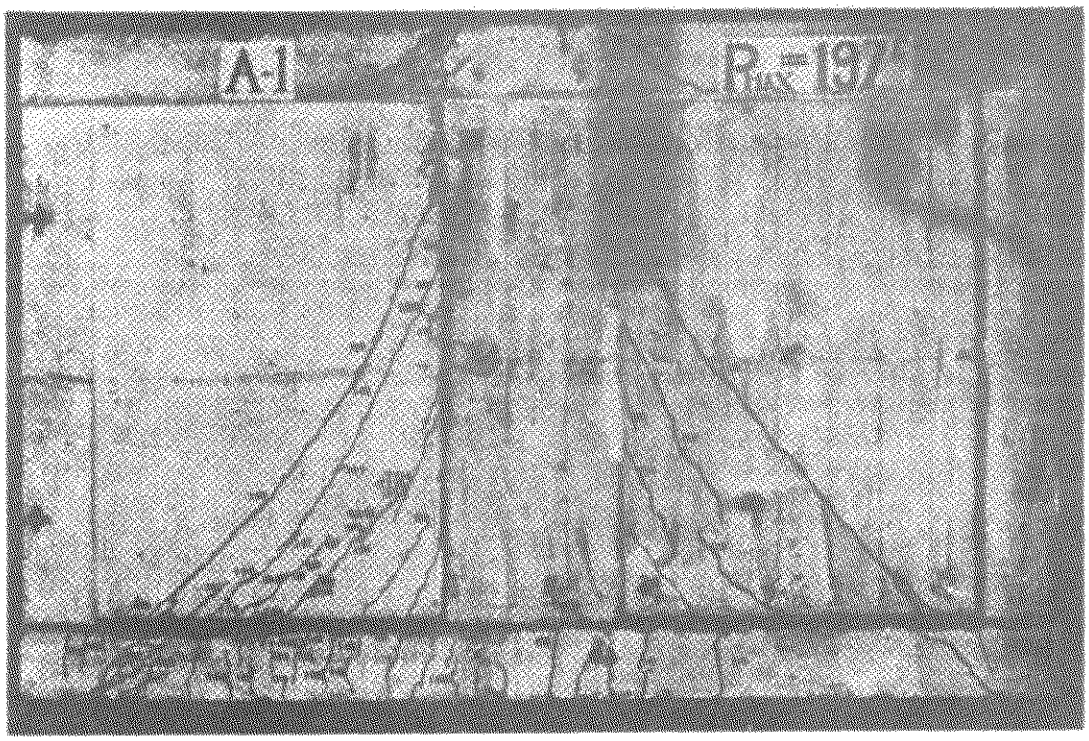

Figure 4.18 Experimental Crack Pattern for Shear Wall-Frame System A-1

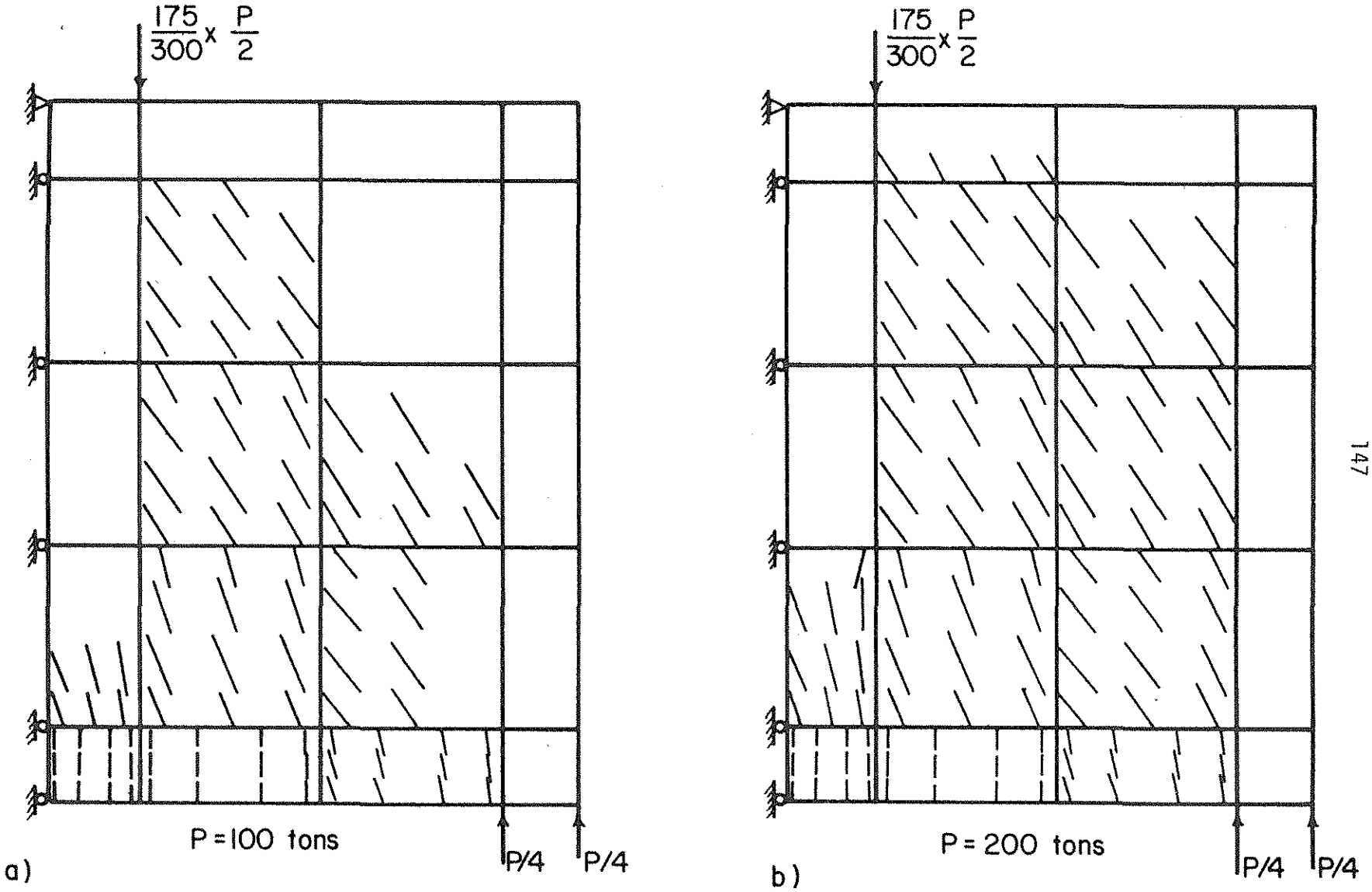

Figure 4.19 Analytical Crack Patterns for Shear Wall-Frame System A-1

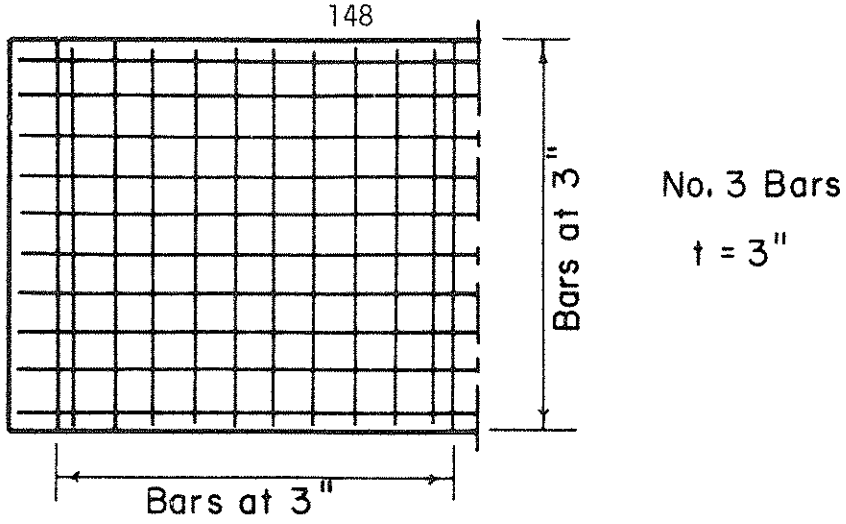

Figure 4.20a Reinforcing for Shear Panel W-4

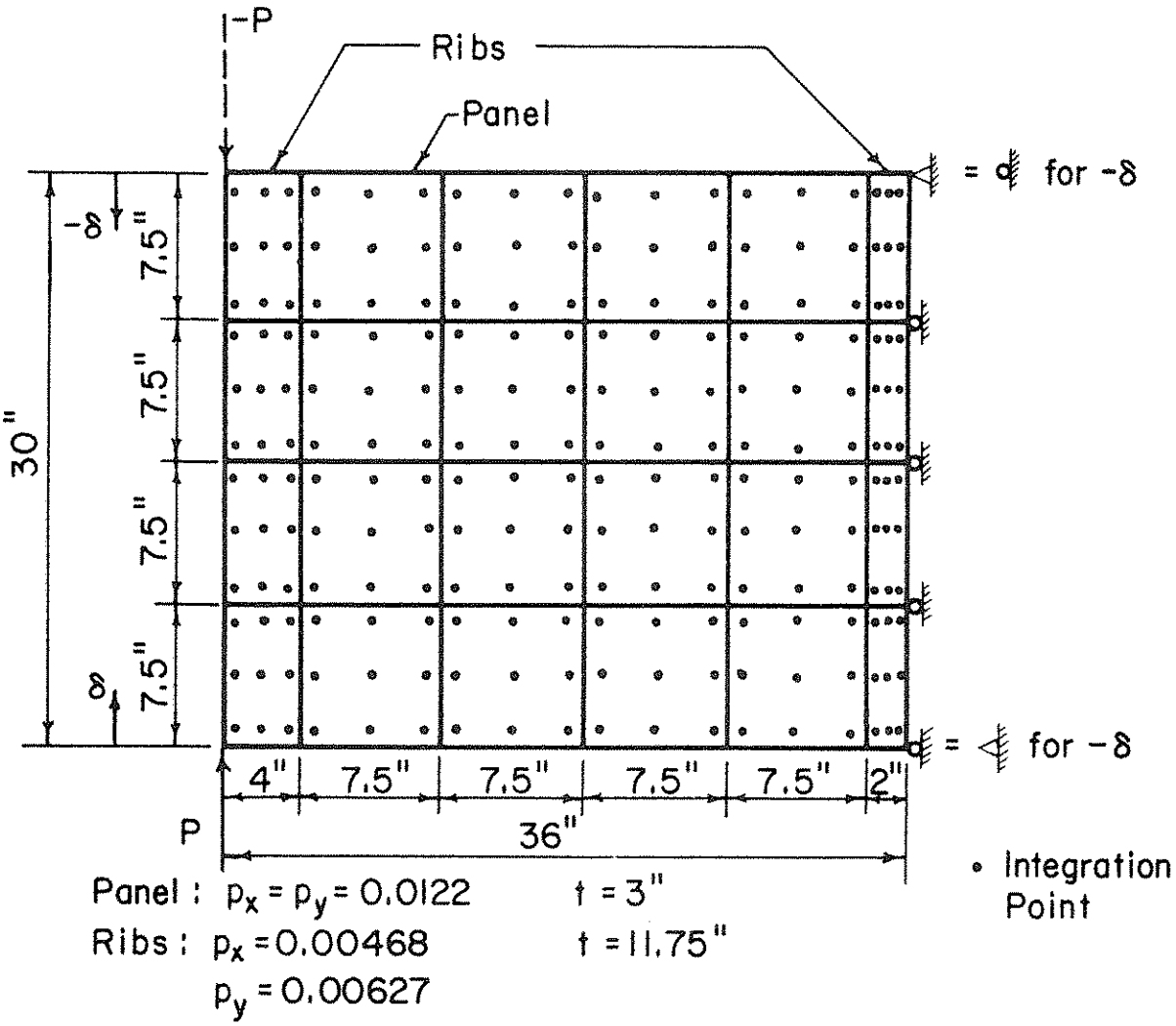

Figure 4.20b Finite Element Model of Shear Panel W-4

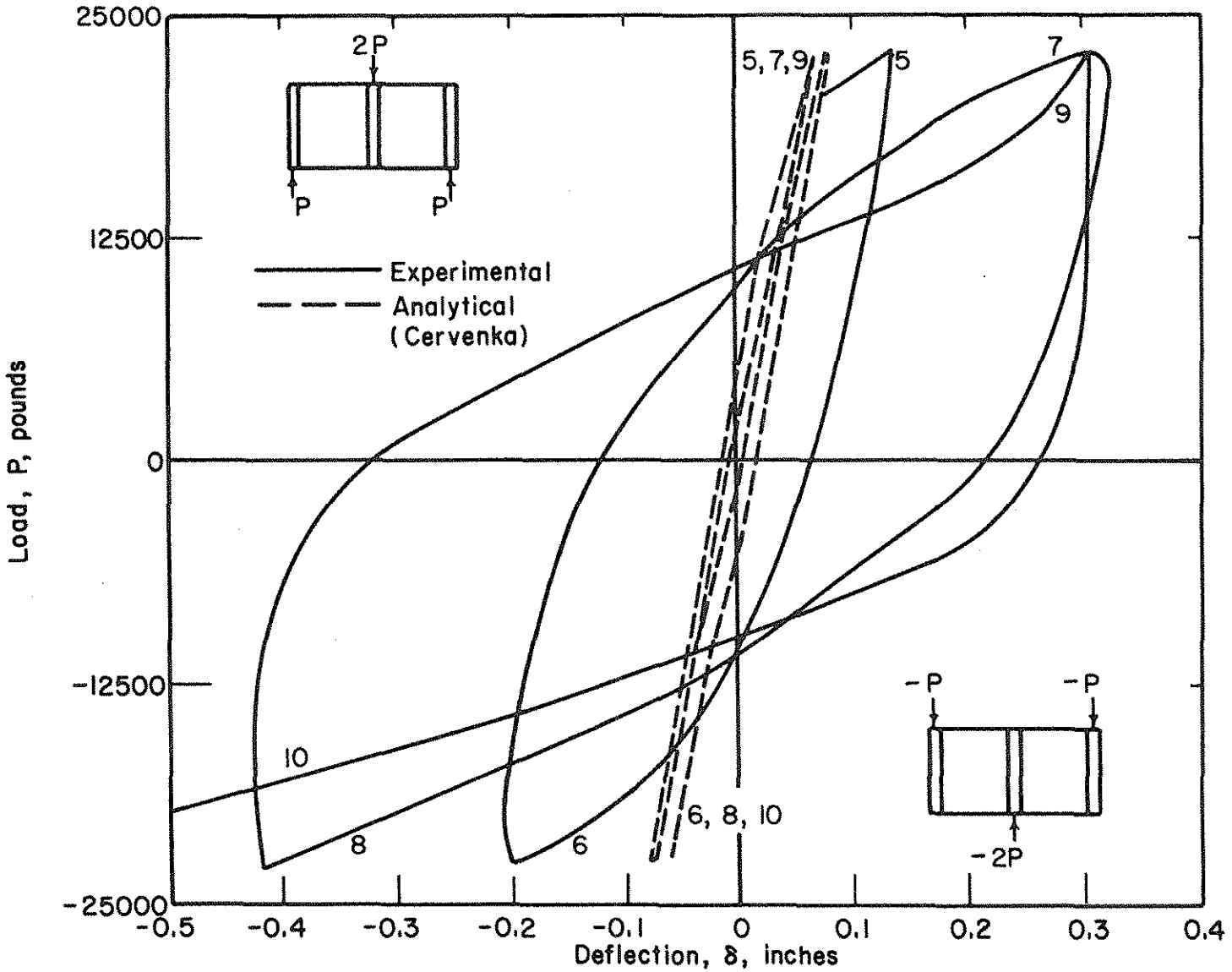

Figure 4.21 Comparison of Cervenka and Gerstle's Model to Experimental Load-Deflection Curve for Cyclic Loading of Shear Panel W-4 (8)

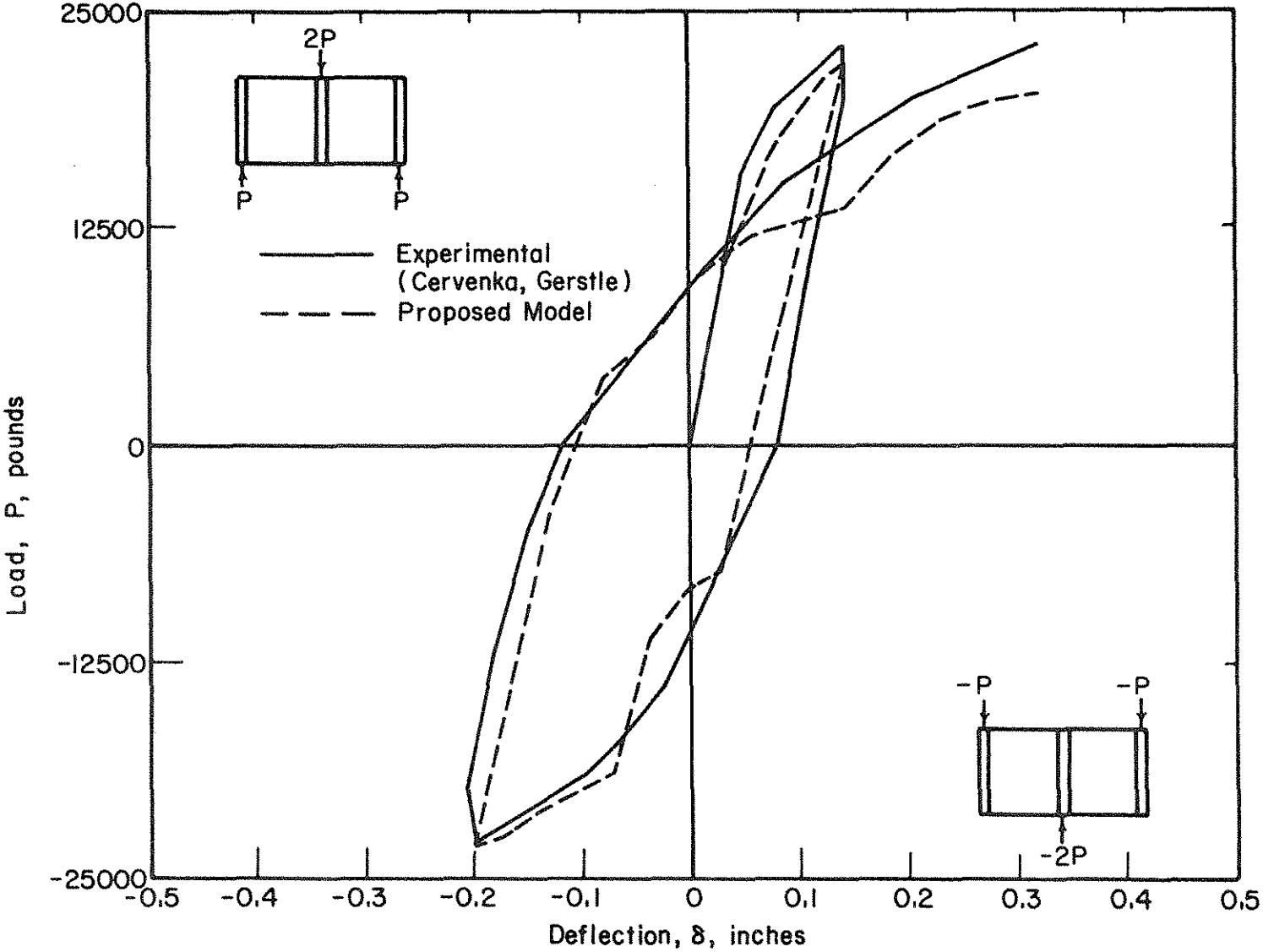

Figure 4.22 Comparison of Proposed Model to Experimental Load-Deflection Curve for Cyclic Loading of Shear Panel W-4

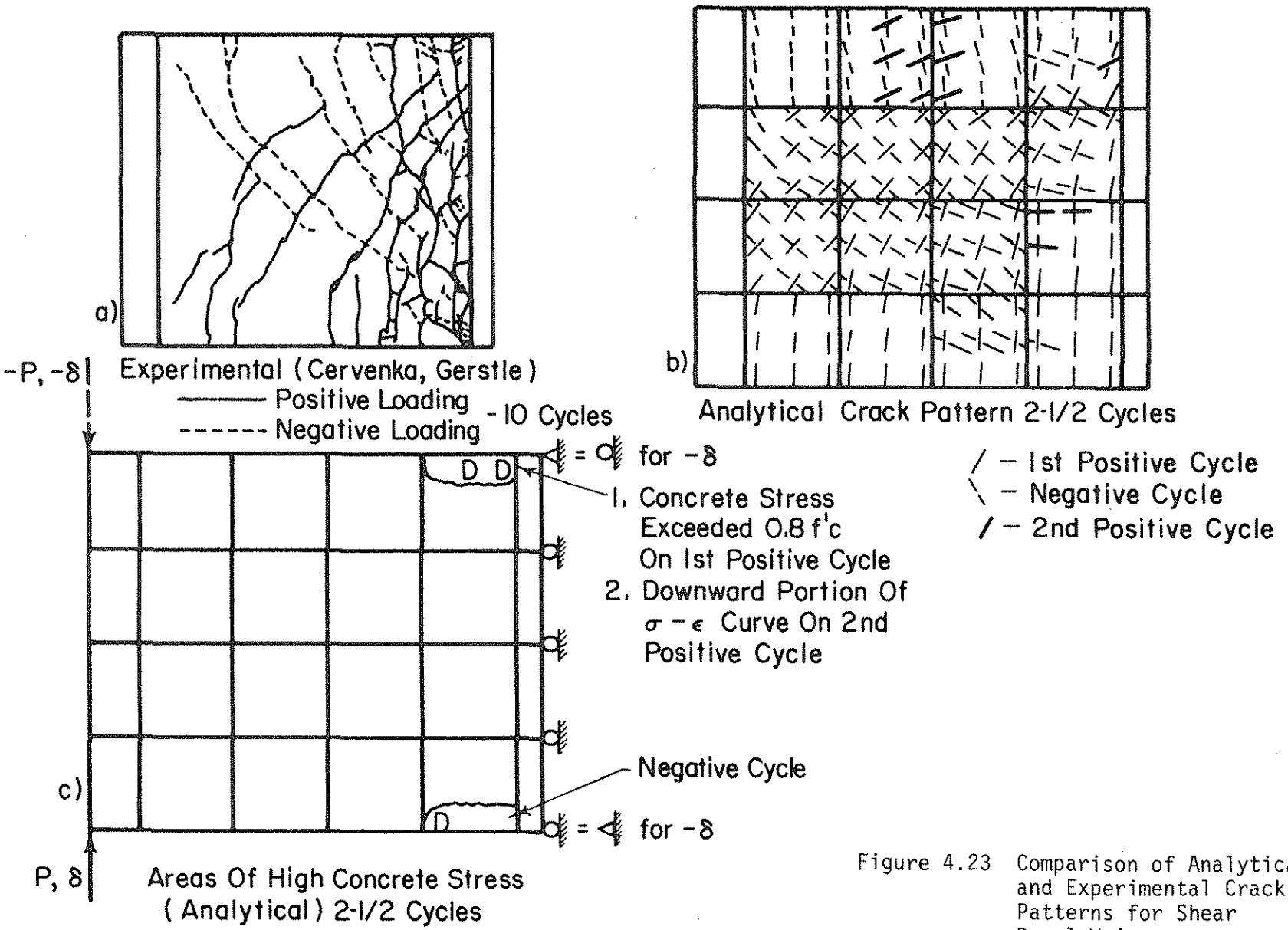

Figure 4.23 Comparison of Analytical and Experimental Crack Patterns for Shear Panel W-4

APPENDIX A

SUMMARY OF MATERIAL MODEL

A.1 Concrete

A.1.1 Orthotropic Constitutive Equations in Material Coordinates (Section 2.2.1)

$$\begin{bmatrix} d\sigma_1 \\ d\sigma_2 \\ d\tau_{12} \end{bmatrix} = \frac{1}{1-\nu^2} \begin{bmatrix} E_1 & \nu\sqrt{E_1E_2} & 0 \\ & E_2 & 0 \\ \text{Sym} & & \frac{1}{4}(E_1+E_2-2\nu\sqrt{E_1E_2}) \end{bmatrix} \begin{bmatrix} d\varepsilon_1 \\ d\varepsilon_2 \\ d\gamma_{12} \end{bmatrix} \quad (A.1)$$

A.1.2 Equivalent Uniaxial Strain (Section 2.2.2)

$$\varepsilon_{iu} = \sum_{\substack{\text{All} \\ \text{load} \\ \text{increments}}} \frac{\Delta\sigma_i}{E_i} \quad (A.2)$$

(except for open crack)

A.1.3 Monotonic Loading Curves (Section 2.2.3)

Compression:

$$\sigma_i = \frac{\varepsilon_{iu} E_o}{1 + [\frac{E_o}{E_s} - 2] \frac{\varepsilon_{iu}}{\varepsilon_{ic}} - (\frac{\varepsilon_{iu}}{\varepsilon_{ic}})^2} \quad (A.3a)$$

where $E_s = \frac{\sigma_{ic}}{\varepsilon_{ic}}$

Tension:

$$\sigma_i = \varepsilon_{iu} E_o \tag{A.3b}$$

Maximum Strength, σ_{ic}:

Compression-Compression:

$$\sigma_{2c} = \frac{1 + 3.65\alpha}{(1 + \alpha)^2} f_c' \tag{A.4a}$$

$$\sigma_{1c} = \alpha \sigma_{2c} \tag{A.4b}$$

where $\alpha = \frac{\sigma_1}{\sigma_2}$

Tension-Compression:

$$\sigma_{1t} = \text{modulus of rupture for structural modeling}$$

$$= (1 - 0.8 \frac{\sigma_2}{f_c'}) f_t' \quad \text{for material simulation} \tag{A.5a}$$

$$\sigma_{2c} = \frac{1 + 3.28\alpha}{(1 + \alpha)^2} f_c' \tag{A.5b}$$

Tension-Tension:

$$\sigma_{1t} = \sigma_{2t} = \text{modulus of rupture for structural modeling}$$

$$= f_t' \quad \text{for material simulation} \tag{A.6}$$

Equivalent Uniaxial Strain at Maximum Stress, ε_{ic}:

$|\sigma_{ic}| \geq |f_c'|$:

$$\varepsilon_{ic} = \varepsilon_{cu} \left[\frac{\sigma_{ic}}{f_c'} R - (R - 1)\right] \tag{A.7}$$

where

$$R = \frac{\frac{\varepsilon_{ic}\ (\alpha = 1)}{\varepsilon_{cu}} - 1}{\frac{\sigma_{ic}\ (\alpha = 1)}{f_c'} - 1} \tag{A.8}$$

$R \simeq 3$ (3.15 used in analysis)

$|\sigma_{ic}| < |f_c'|$:

$$\varepsilon_{ic} = \varepsilon_{cu} \left[-1.6 \left(\frac{\sigma_{ic}}{f_c'}\right)^3 + 2.25 \left(\frac{\sigma_{ic}}{f_c'}\right)^2 + 0.35 \frac{\sigma_{ic}}{f_c'}\right] \tag{A.9}$$

Poisson's Ratio:

$\nu = 0.2$ for tension-tension and compression-compression (A.10a)

$$\nu = 0.2 + 0.6\left(\frac{\sigma_2}{f_c'}\right)^4 + 0.4\left(\frac{\sigma_1}{\sigma_{1t}}\right)^4 \tag{A.10b}$$

≤ 0.99 for uniaxial compression and tension-compression

A.1.4 Cyclic Loading Curves (Section 2.2.5)

Plastic Strain, ε_p:

$$\frac{\varepsilon_p}{\varepsilon_{cu}} = 0.145 \left(\frac{\varepsilon_{en}}{\varepsilon_{cu}}\right)^2 + 0.13 \left(\frac{\varepsilon_{en}}{\varepsilon_{cu}}\right) \tag{A.11}$$

Common Points and Turning Points:

See Fig. 2.33.

Poisson's Ratio:

$$\nu = 0.2 \quad \text{for} \quad |\varepsilon_{en}| \leq |\varepsilon_{cu}| \tag{A.12a}$$

$$\nu = 0 \quad \text{for} \quad |\varepsilon_{en}| > |\varepsilon_{cu}| \tag{A.12b}$$

A.1.5 Cracking (Section 2.2.6)

Constitutive Equations in Material Coordinates:

One Crack Open:

$$\begin{bmatrix} d\sigma_1 \\ d\sigma_2 \\ d\tau_{12} \end{bmatrix} = \begin{bmatrix} 0 & 0 & 0 \\ 0 & E_2 & 0 \\ 0 & 0 & E_2/4 \end{bmatrix} \begin{bmatrix} d\varepsilon_1 \\ d\varepsilon_2 \\ d\gamma_{12} \end{bmatrix} \tag{A.13}$$

Two Cracks Open:

$$d\sigma = \begin{bmatrix} 0 \\ 0 \\ 0 \end{bmatrix} \tag{A.14}$$

Crack Width, C_{wi}:

$$C_{wi} = \frac{\sigma_{cri}}{E_i} + \sum_{\substack{\text{load increments} \\ \text{following crack} \\ \text{formation}}} (\Delta\varepsilon_i + \nu\Delta\varepsilon_j) \tag{A.15}$$

where $\Delta\varepsilon_i$ and $\Delta\varepsilon_j$ are the true strain increments perpendicular and parallel to the crack, respectively, and $\nu = 0.2$, unless set to zero by Eq. A.12b. $\nu = 0$ if two cracks are open.

A.2 Steel (Section 2.3)

Bilinear, strain hardening material.

$$E_{sh} \simeq 0.05\, E_{\substack{\text{steel} \\ \text{(elastic)}}} \tag{A.16}$$

(see Figs. 2.44 and 2.45)

A.3 Material Data Required for Computer Analysis

A.3.1 The Following Information Must Be Input for the Elements (may Vary from Element to Element)

E_o = initial stiffness of the concrete

f'_c = compressive strength of the concrete under uniaxial load

ε_{cu} = strain at f_c'

f_t' = tensile strength of the concrete

t = thickness of the concrete

A.3.2 The Following Information Must Be Input for the Material Points (May Vary from Point to Point)

$E_{steel\ i}$ = elastic stiffness of the reinforcing steel

f_{yi} = yield strength of the reinforcing steel

$p_{steel\ i}$ = steel ratio
(= area of steel/area of concrete)

$\delta_{steel\ i}$ = ratio of the strain hardening stiffness, E_{sh} to E_{steel}

ϕ_i = orientation of steel

i = 1, 2

APPENDIX B

PROPERTIES OF THE FINITE ELEMENT

B.1 Introductory Comments

The finite element used in this study is a four noded, quadrilateral, isoparametric element with two translational degrees of freedom at each node, plus four non-conforming degrees of freedom. The element and the degrees of freedom are shown in Fig. 3.1. The purpose of adding the extra four incompatible modes is to "soften" the element to give a better match with the elastic solution for pure flexure. Nonconforming or incompatible modes allow separation or overlapping of elements during deformation.

The coordinates (X,Y) of any point in the element may be expressed as follows (Fig. B.1):

$$X = \sum_{i=1}^{4} h_i X_i \qquad \text{(B.1a)}$$

$$Y = \sum_{i=1}^{4} h_i Y_i \qquad \text{(B.1b)}$$

where X_i and Y_i are the X and Y coordinates of the corner nodes, respectively, and h_i are the following shape functions:

$$h_1 = \frac{1}{4}(1 - \xi)(1 + \eta)$$

$$h_2 = \frac{1}{4}(1 - \xi)(1 - \eta)$$

$$h_3 = \frac{1}{4}(1 + \xi)(1 - \eta)$$

$$h_4 = \frac{1}{4}(1 + \xi)(1 + \eta)$$

where ξ and η are the nondimensional coordinates of point (X,Y) within the element, and have the range $-1 \leq \xi,\eta \leq 1$. The displacements (u_x,u_y) of point (X,Y) is given as follows:

$$u_x = \sum_{i=1}^{4} h_i u_{xi} + h_5\gamma_1 + h_6\gamma_3 \qquad \text{(B.3a)}$$

$$u_y = \sum_{i=1}^{4} h_i u_{yi} + h_5\gamma_2 + h_6\gamma_4 \qquad \text{(B.3b)}$$

where u_{xi} and u_{yi} are the displacements of the corner nodes, γ_1, γ_2, γ_3 and γ_4 are the displacements of the incompatible modes, and h_5 and h_6 are the shape functions that describe the incompatible modes.

$$h_5 = (1 - \xi^2)$$

$$h_6 = (1 - \eta^2) \qquad \text{(B.4)}$$

It is interesting to note that the shapes of the incompatible modes (Fig. 3.1) vary quadratically from zero at the element extremes to a maximum at the center lines of the element. The values of γ_i in Eqs. B.3 represent departures from linear displacements. Therefore, the nonconforming modes can be conveniently suppressed by setting $\gamma_i = 0$, as a geometric boundary condition. When this is done the element becomes an eight degree of freedom, conforming isoparametric element.

It should be mentioned that this element was originally tested as a rectangular quadrilateral (25) and that there is no assurance that the incompatible modes will lead to reasonable solutions if the quadrilateral is distorted. Iron's Patch Test (27) is a useful tool for assessing behavior characteristics of nonconforming elements.

B.2 Strain at a Point

The strains at a point may be obtained by taking appropriate derivatives of displacements. Strains are obtained from Eqs. B.3 as follows:

$$\varepsilon_x = \frac{\partial u_x}{\partial x} = \sum h_{i,x} u_{xi} + h_{5,x}\gamma_1 + h_{6,x}\gamma_3$$

$$\varepsilon_y = \frac{\partial u_y}{\partial y} = \sum h_{i,y} u_{yi} + h_{5,y}\gamma_2 + h_{6,y}\gamma_4 \qquad \text{(B.5)}$$

$$\gamma_{xy} = \frac{\partial u_x}{\partial y} + \frac{\partial u_y}{\partial x} = \sum h_{i,y} u_{xi} + \sum h_{i,x} u_{yi}$$

$$+ h_{5,y}\gamma_1 + h_{6,y}\gamma_3 + h_{5,x}\gamma_2 + h_{6,x}\gamma_4$$

where $\_,x$ represents the partial derivative with respect to X.

Since the shape functions, $h_i (i = 1,6)$, are expressed as functions of ξ and η the derivatives with respect to X and Y must be calculated using the chain rule.

$$h_{i,x} = h_{i,\xi}\,\xi_{,x} + h_{i,\eta}\,\eta_{,x}$$

$$(i = 1,4) \qquad \text{(B.6)}$$

$$h_{i,y} = h_{i,\xi}\,\xi_{,y} + h_{i,\eta}\,\eta_{,y}$$

It can be shown (25) that:

$$\begin{bmatrix} \xi_{,x} & \eta_{,x} \\ \xi_{,y} & \eta_{,y} \end{bmatrix} = \frac{1}{|J|} \begin{bmatrix} Y_{,\eta} & -Y_{,\xi} \\ -X_{,\eta} & X_{,\xi} \end{bmatrix} \qquad \text{(B.7)}$$

where $$|J| = X_{,\xi}\, Y_{,\eta} - X_{,\eta}\, Y_{,\xi} \tag{B.8}$$

and
$$X_{,\xi} = \sum h_{i,\xi} X_i$$
$$X_{,\eta} = \sum h_{i,\eta} X_i \qquad (i = 1, 4) \tag{B.9}$$
$$Y_{,\xi} = \sum h_{i,\xi} Y_i$$
$$Y_{,\eta} = \sum h_{i,\eta} Y_i$$

Equation B.5 may now be expressed in the following matrix form:

$$\begin{bmatrix} \varepsilon_x \\ \varepsilon_y \\ \gamma_{xy} \end{bmatrix} = \frac{1}{|J|} \left[\begin{array}{cc|cc|c|cc} \alpha_1 & 0 & \alpha_2 & 0 & & \alpha_6 & 0 \\ 0 & \beta_1 & 0 & \beta_2 & \cdots & 0 & \beta_6 \\ \beta_1 & \alpha_1 & \beta_2 & \alpha_2 & & \beta_6 & \alpha_6 \end{array}\right] \begin{bmatrix} u_{x1} \\ u_{y1} \\ \cdot \\ \cdot \\ \cdot \\ u_{x4} \\ u_{y4} \\ \gamma_1 \\ \gamma_2 \\ \gamma_3 \\ \gamma_4 \end{bmatrix} \tag{B.10}$$

where: $$\alpha_i = h_{i,x}\, |J| \qquad (i = 1,6)$$
$$\beta_i = h_{i,y}\, |J|$$

In symbolic terms, Eq. B.10 may be written as:

$$\varepsilon = Bu = \frac{\overline{B}}{|J|}\, u \tag{B.11}$$

B.3 Element Stiffness Matrix

The element stiffness matrix is given by

$$K = \int_{area} t\, B^T\, DB\, dA \tag{B.12}$$

where t is the element thickness and D is the constitutive matrix. Integration is done over the area of the element.

Equation B.12 may be rewritten for the purpose of numerical integration.

$$K = \int_{-1}^{1} \int_{-1}^{1} t\, B^T\, DB\, |J|\, d\xi\, d\eta \tag{B.13a}$$

or

$$K = \int_{-1}^{1} \int_{-1}^{1} t\, \overline{B}^T\, D\overline{B}\, \frac{d\xi\, d\eta}{|J|} \tag{B.13b}$$

The numerical integration (20) is done with the following summation:

$$K = \sum_j \sum_k H_j\, H_k\, t_{jk}\, \overline{B}_{jk}^T\, D_{jk}\, \overline{B}_{jk}\, \frac{1}{|J|_{jk}} \tag{B.14}$$

where t_{jk}, $\overline{B}_{jk}$, D_{jk} and $|J|_{jk}$ take on the appropriate values at each integration point (ξ_j, η_k). H_j and H_k are the appropriate weighting factors.

B.4 Element Residual Loads

The residual loads due to inelastic behavior for the element are given by:

$$R = \int_{area} t\, B^T \sigma_r \, dA \tag{B.15}$$

where the residual stresses, σ_r, are given by:

$$\sigma_r = \begin{bmatrix} \sigma_{xr} \\ \sigma_{yr} \\ \sigma_{xyr} \end{bmatrix}$$

In terms of the nondimensional coordinates, Eq. B.15 may be rewritten.

$$R = \int_{-1}^{1} \int_{-1}^{1} t\, \bar{B}^T \sigma_r \, d\xi \, d\eta \tag{B.16}$$

Numerical integration to obtain the residual loads takes the following form:

$$R = \sum_i \sum_k H_j H_k t_{jk} \bar{B}_{jk}^T \sigma_{rjk} \tag{B.17}$$

where H_j, H_k, t_{jk} and $\bar{B}_{jk}$ are defined in Eq. B.14.

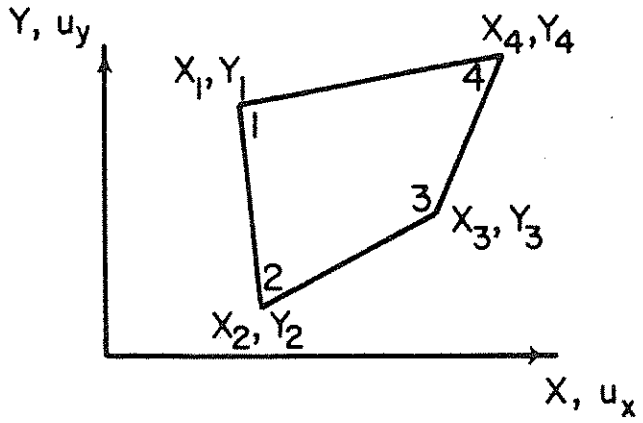

a) Global Coordinates

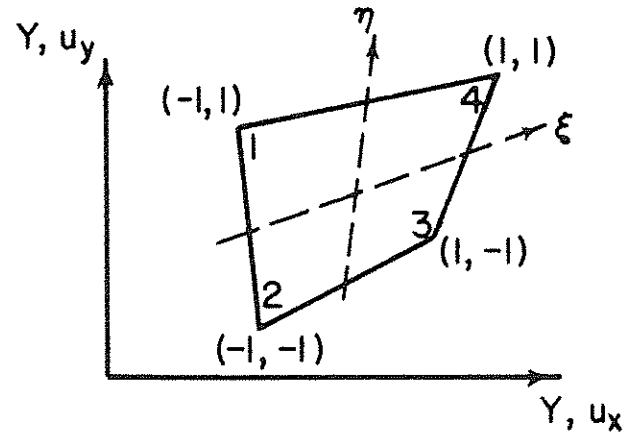

b) Non-Dimensional Coordinates

Figure B.1 Global and Non-Dimensional Coordinates

APPENDIX C

NOMENCLATURE

Symbols used in the text are defined where they first appear. A summary of frequently used symbols is presented below for convenience. Symbols with dual meanings are listed twice.

B, B_{jk}	matrix (3 x 12) relates strains at a point (j,k) to finite element nodal displacements
$\overline{B}$, $\overline{B}_{jk}$	B divided by Jacobian, $\|J\|$
C_w, C_{wi}	crack width, defined in terms of strain
$d\epsilon$	differential strain vector in material coordinates: $d\epsilon_1$, $d\epsilon_2$, $d\gamma_{12}$
$d\sigma$	differential stress vector in material coordinates: $d\sigma_1$, $d\sigma_2$, $d\tau_{12}$
D, D_{ij}	constitutive matrix (3 x 3)
$D^{(i)}$	tangent D for ith iteration
D_{steel}	contribution of steel to total D
E_i, E_1, E_2	tangent stiffness in direction of material axes
E_o	initial stiffness of concrete
E_s	$\sigma_{ic}/\epsilon_{ic}$, secant stiffness to point of maximum strength for concrete

E_{sh}	strain hardening stiffness of reinforcing steel
E_{steel}, $E_{steel\ i}$	elastic stiffness of reinforcing steel
f_c', f_t'	uniaxial compressive and tensile strength of concrete, respectively
f_y, f_{yi}	yield strength of steel
G, G'	shear stiffness and transformed shear stiffness, respectively
h_i, i = 1,6	shape functions
H_i, H_k	weighting factors for Gaussian integration
$\|J\|$, $\|J\|_{jk}$	Jacobian
K	structure stiffness matrix: K_{II}, K_{IB}, K_{BI}, K_{BB}
L_K	localizing matrix, relates nodal displacements of element K to structure displacement vector, U
p_{steel}, $p_{steel\ i}$	steel ratio
P	nodal load vector
R	factor relating ε_{ic} to ε_{cu} for values of $\|\sigma_{ic}\| < \|f_c'\|$, and
R	residual load vector
t, t_{jk}	element thickness

T	transformation matrix
u_x, u_y, u_{xi}, u_{yi}	element displacements
U	structure displacement vector
X, Y	global coordinates
α	σ_1/σ_2 ratio of principal stresses, $\sigma_1 \geq \sigma_2$
α_i, β_i	first partial derivatives of h_i with respect to X and Y; found in B matrix
γ_{xy}, γ_{12}	shear strain in x, y or 1, 2 coordinates
γ_i, $i = 1,4$	nonconforming degrees of freedom
$\delta( )$	change in a quantity during iteration
δP, δP_B, δP_I	nodal loads
δR_B, δR_I	residual nodal loads
$\delta\sigma$, $\delta\sigma_K$	apparent change in stresses at a point
δ_u	change in element nodal displacements
δU, δU_B, δU_I	change in structure nodal displacements
$\Delta( )$	total change in a quantity during load increment
$\Delta\varepsilon_i$	change in strain parallel to i axis
ΔP, ΔP_I, ΔP_B	increments of nodal loads applied to structure

$\Delta\sigma_i$	$\sigma_{i\ new} - \Delta\sigma_{i\ old}$, change in stress at a point
$\Delta\sigma_K$	true change in stress at a point
ΔU_B	imposed boundary displacements
ε	strain at a point; ε_x, ε_y, γ_{xy}
ε_{cp}	common point strain
ε_{cu}	strain corresponding to f_c'
ε_{en}	envelope strain
ε_i	strain in ith direction
ε_{ic}	equivalent uniaxial strain corresponding to, σ_{ic}
ε_{iu}	equivalent uniaxial strain in ith direction
ε_p	plastic strain
ε_{tp}	turning point strain
η, η_k	nondimensional coordinate
ν	"equivalent" Poisson's ratio, = $\nu_1\nu_2$
ν_1, ν_2	Poisson's ratio in 1 and 2 directions, respectively
ξ, ξ_j	nondimensional coordinate
σ	stress at a point: σ_x, σ_y, τ_{xy}

σ_{cp}	common point stress
σ_{cri}	"stress" in concrete just prior to cracking
σ_{en}	envelope stress
σ_{ic}, $i = 1,2$	compressive strength of concrete in ith direction
σ_{it}, σ_{1t}, σ_{2t}	tensile strength of concrete
$\sigma_{i\,new}$, $\sigma_{i\,old}$	stresses in ith material coordinate at end and beginning of load increment, respectively
σ_r, σ_{rk}	residual stress at a point: σ_{xr}, σ_{yr}, τ_{xyr}
σ_{tp}	turning point stress
σ_i, σ_1, σ_2	stress in material axes, $\sigma_1 > \sigma_2$